Adventitious Hydrocarbon Adsorption and Its Effect on the Solid-Liquid Interface

by

Justin Mitchell Hurst

Bachelor of Science, Millersville University, 2012

Submitted to the Graduate Faculty of the

Dietrich School of Arts and Sciences in partial fulfillment

of the requirements for the degree of

Doctor of Philosophy

University of Pittsburgh

2020

UNIVERSITY OF PITTSBURGH

DIETRICH SCHOOL OF ARTS AND SCIENCES

This dissertation was presented

by

Justin Mitchell Hurst

It was defended on

June 12, 2020

and approved by

Dr. Alexander Star, Professor, Department of Chemistry

Dr. Shigeru Amemiya, Professor, Department of Chemistry

Dr. Lei Li, Associate Professor, Department of Chemical and Petroleum Engineering

Dissertation Advisor: Dr. Haitao Liu, Associate Professor, Department of Chemistry

Adventitious Hydrocarbon Adsorption and Its Effect on the Solid-Liquid Interface

Justin Mitchell Hurst, Ph.D.

University of Pittsburgh, 2020

Atmospheric hydrocarbon adsorption has recently been revealed to mask the intrinsic properties of some surfaces. The prevalence of hydrocarbon adsorption was previously only understood in vacuum science, but as new sensitive techniques developed it became possible to study the adsorption behavior in ambient air. In this work, we have studied the effect of atmospheric adsorption on graphite and soil minerals.

We studied the change in capacitance on aqueous graphite electrodes when exposed to air and while in solution. We found that exposing a freshly exfoliated highly oriented pyrolytic graphite (HOPG) surface to ambient air and 1-octadecene vapor (*ca.* 1 ppm) caused a *ca.* 30% and 70% decrease in its double layer capacitance, respectively. Similarly, a 38% decrease of capacitance was observed within 1500 min after a freshly cleaved HOPG was immersed in 1 M NaCl solution; liquid phase ellipsometry data showed that a contamination layer of *ca.* 0.6 - 2 nm was formed on the HOPG surface within the same time frame. The capacitance of a contaminated sample can be partially and temporarily restored by applying a high or low potential (-1.222 V or 0.778 V *vs.* Ag/AgCl). For graphite in 1-butyl-3-methylimidazolium hexafluorophosphate, we found a slight difference between the capacitance in a clean hood and in a glove box. Solution phase capacitance reduction is between 25-30% in both pure solution and with added contaminant. This work also emphasized the U-shaped capacitance *vs.* potential curve of the graphite-ionic liquid system, contrary to recent literature.

The second system of study is the soil-water interface. In this work we showed how airborne adventitious hydrocarbons can adsorb to mineral surfaces to contribute to soil-water repellency. The water contact angle (WCA) was shown to increase from 0° to 25° for silica, and to 65° for alumina after 4 days of exposure in ambient air. The change in the amount of hydrocarbons was monitored by spectroscopic ellipsometry (SE) and X-ray photoelectron spectroscopy (XPS). Water drop penetration time (WDPT) was measured on kaolinite after treatments with either heat or ozone to show that adsorption of airborne hydrocarbons can increase the WDPT of mineral powders.

Table of Contents

List of Tables

List of Figures

1.0 Introduction

1.1 Introduction to Surfaces and Interfaces

Chemistry has been dominated by the study of the bulk for the majority of its existence as a natural science. The technology to study surfaces and interfaces did not exist until the 1960's and 1970's. Perhaps the best example of the emergence of the study of surfaces is the development of low energy electron diffraction.[1] It was originally difficult to resolve the occurrences on the surface due to interference of gas molecules in air. Advances in vacuum technology allowed for air pressures near 10^{-9} torr, and subsequent studies utilized this to study reactions at surfaces.[2] A new field of vacuum science was born, including many types of electron spectroscopies that would not be possible without high vacuum. Discoveries about the interactions of photoelectrons with solid surfaces allowed for detailed analysis like never before.

Another type of vacuum measurement, scanning tunneling microscopy (STM), also benefited from the advent of vacuum science. The precursor to this technique was first presented in 1971.[3] Developments in this field also led to atomic force microscopy (AFM). These techniques existed due to the rapid increase in computational power, and the precision that such devices allowed.

As a greater understanding of surfaces and interfaces was built, more spectroscopic technologies were also developed; such as those we will discuss below. Without the foundation provided by vacuum science, we would be decades behind where we are today. Some of the lessons learned from the early days of vacuum science were forgotten and had to be recalled in order to describe some unexpected phenomena.

1.1.1 Masking of Surface Properties

Surface adsorbed carbon has been well known in vacuum science since the early days of surface measurements. It is so prolific that it is even used as a binding energy standard for instrument calibration.[4] This surface layer is fairly strongly bound, as it remains on the surface even in ultra-high vacuum (UHV) and requires specialized techniques to remove it.[5-6] Usually, it is more convenient to ignore the surface adsorbed carbon, as these cleaning techniques inevitably affect the surface in some way. Some processes that involve chemical reactions (*i.e.* atomic layer deposition) or are not sensitive to carbon are unaffected by the contamination layer. The assumption that surface adsorbed carbon has a negligible effect on the system can be valid but is not true for all surface properties or modifications.

Some material properties are particularly sensitive to changes on the surface. One of these properties is wettability. The interaction between water and a surface is determined by the surface energy, or by the amount of energy it takes to increase the surface area of a liquid or solid. The stronger the interaction between the liquid and the surface, the lower the contact angle. Since the bulk underneath the surface has little to no impact on the contact angle, surface coatings are quite impactful. This has been shown for many systems, including silica, titania, and boron nitride nanotubes.[7-9] Another substrate of interest is graphite. It is difficult to differentiate surface carbon from the graphitic carbon with electron spectroscopy. Also, graphite is reactive to some of the strongly oxidizing techniques that are used to clean the surface carbon from materials like silica and titania. The wetting of graphite was reevaluated with several modern techniques and shown to be more hydrophilic than previously believed.[10] With this context in mind, we must ask ourselves what other surface properties have been overlooked since the advent of more sensitive surface analysis techniques.

1.1.2 Double Layer Capacitance

The current state of affairs in the world economy calls for more effective energy storage devices.[11] As we collectively work to limit the usage of fossil fuels, electrical energy storage is the best solution for the time being. Electrical energy is provided to nearly every home in the developed world, so it follows that it is this energy form we should use. Storage of electrical energy is an important factor in transportation.[12] Lithium ion batteries currently are the most prolific energy storage device, but certain inefficiencies in battery performance require for other technologies to fill the gap.[13] Figure 1 illustrates how capacitors can complement batteries in electrical energy storage.

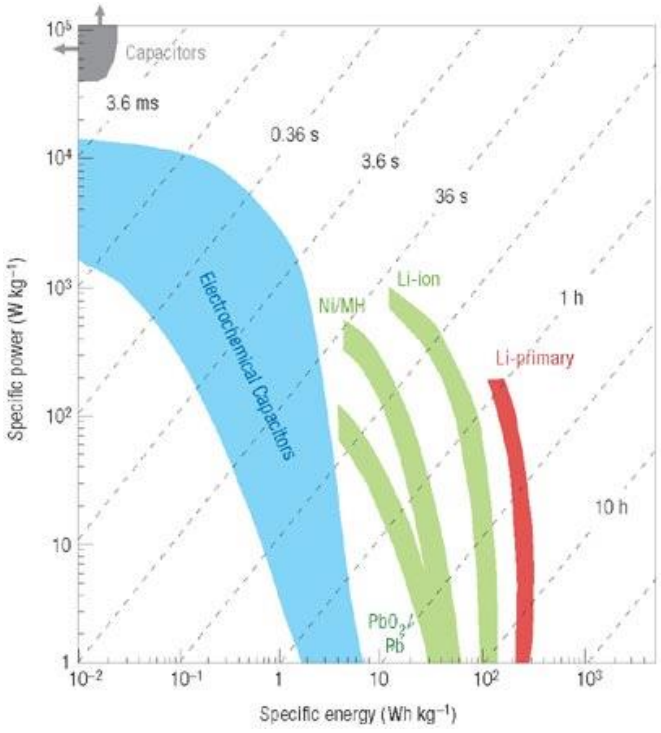

Figure 1. Ragone plot comparing the power density and energy density of capacitors and batteries. Reprinted by permission from Nature Materials **2008**, 7, 845–854. Copyright 2008 Springer Nature.[14]

New research is needed into such devices to optimize their energy density. The theoretical limit of certain capacitors even approaches that of a lead acid battery.[15] Though impressive energy density is possible, capacitors excel where high power and quick charge/discharge cycles are needed.[16] The capacitance of two parallel plates is given by:

$$C = \frac{\varepsilon \varepsilon_0 A}{d} \quad [1]$$

where C is the capacitance in farads, ε_0 is the permittivity of free space, ε is the dielectric constant of the medium between the two plates, and A is the area of the plates. This idealized equation helps us to understand the general properties of capacitors, but the true capacitance also changes with voltage, temperature, and many other factors. Another type of capacitor, an electrochemical capacitor, uses a phenomenon known as the electrical double layer to store larger amounts of energy.[17]

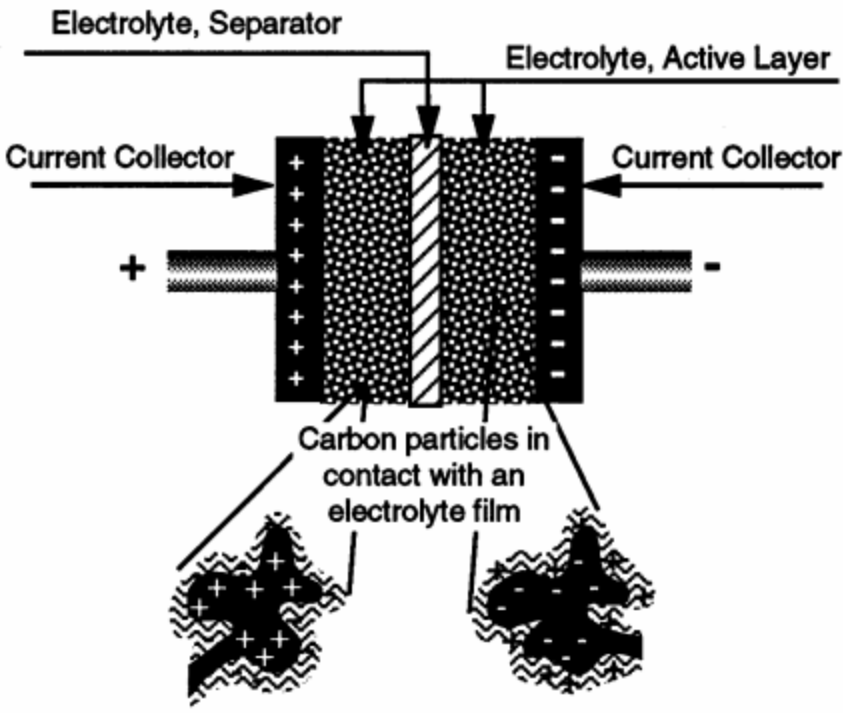

Figure 2. A diagram of the components of an electrochemical capacitor. Insert shows a high surface area electrode material. Adapted from reference 8.[18]

Electrochemical capacitors are often constructed of an electrode material, a porous non-conducting separator, an electrolyte solution, and a current collector. The non-conducting separator functions to inhibit a short circuit, which would remove the capacitive behavior. The electrodes are most often either carbon based, a transition metal oxide, or a conductive polymer. The electrolyte solution is either an aqueous electrolyte solution, or an ionic liquid. The current collector is any conductive material that can serve as a structure to the apparatus.[18]

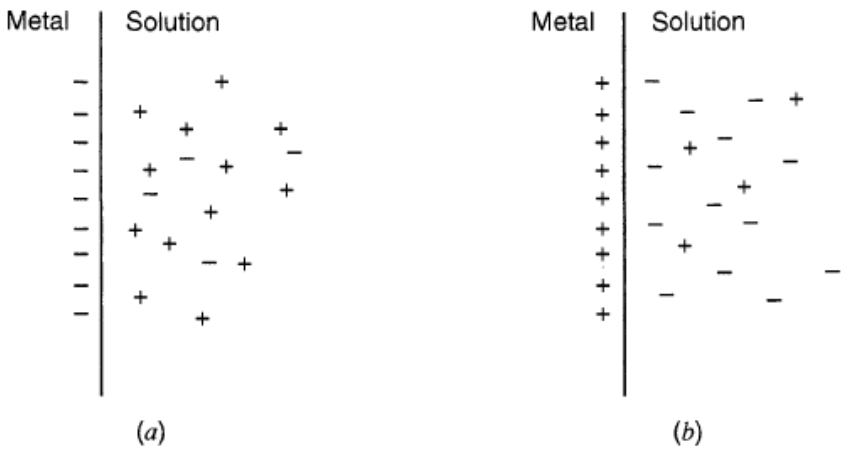

Figure 3. Visualization of an electrode building up (a) negative charge and (b) positive charge at the metal/solution interface. [19]

The electrical double layer forms in any electrochemical cell when a potential is applied. As charge builds up on the electrode surface, ions of the opposite charge are attracted to the electrode and ions of same charge are repelled. The excess charge that is near the electrode can be seen as the other "plate" of a parallel plate capacitor. The electrical double layer can be described by the Gouy-Chapman-Stern model.[19] This model constructs the double layer as two components: the capacitance of the compact layer, and the capacitance of the diffuse layer. The model is described by equation 2.

$$\frac{1}{C_d} = \frac{x_2}{\varepsilon\varepsilon_0} + \frac{1}{(2\varepsilon\varepsilon_0 z^2 e^2 n^0/kT)^{1/2}\cosh(ze\phi_2/2kT)} \quad [2]$$

The measured (experimental) double layer capacitance is C_d, x_2 is the distance between the plane of closest approach and the electrode, ε is the dielectric constant of the interface, ε_0 is the vacuum permittivity, e is the charge on the electron, n^0 is the number ions in the bulk, k is Boltzmann's constant, T is the absolute temperature, z is the charge of the electrolyte ion, and ϕ_2

is the potential at distance x_2. The first term is the capacitance generated by the plane of closest approach for a charge carrier. It is generally accepted that the plane of closest approach is determined by the solvated radius of the charge carrier.[20] The second term describes the capacitance of the diffuse layer. The diffuse layer capacitance arises from the charge gradient that is induced on the solution as described above.

Various carbon materials offer promising electrical properties for uses in the supercapacitor industry. Activated carbon supercapacitors have been quoted to power densities of 5 kW/kg and graphene to as much as 85 kW/kg, whereas a typical battery is often less than 1 kW/kg.[21-23] Graphene's superior electrical capabilities can be attributed to: a) its electron mobility of 2.5×10^5 $cm^2\ V^{-1}\ s^{-1}$ and b) its 2D structure, which allows for an atomically thin electrode that maximizes surface area.[24] These properties, along with carbon's ability to form other useful nanostructures, make carbon a popular subject of investigation. One particular carbon material, highly ordered pyrolytic graphite (HOPG), is useful for studying the surface interactions of sp^2 hybridized carbon networks.[25] HOPG is, in fact, the very material from which graphene was first isolated.[26] It is also easy to prepare, as a fresh surface can be exposed by scotch tape exfoliation. A study of the surface properties of HOPG is then merited for its own sake and also for comparison with the properties of other carbon materials.

A previous study on the wettability of HOPG has suggested that surface contamination from airborne hydrocarbons can affect its water contact angle. Kozbial et al. showed that a significant layer of hydrocarbons can adsorb to the HOPG surface within 15 minutes of air exposure.[27] This data implies that for other surface properties of HOPG, such as double layer capacitance, there will also be a change with air exposure. Other studies have also shown airborne contaminants to affect surface properties of electrodes and other materials.[10, 28-31] Hydrocarbon

contamination could play a key role in carbon capacitor performance. With this precedent, we shall use HOPG as a model system to determine the effect of atmospheric contaminants on carbon surfaces.

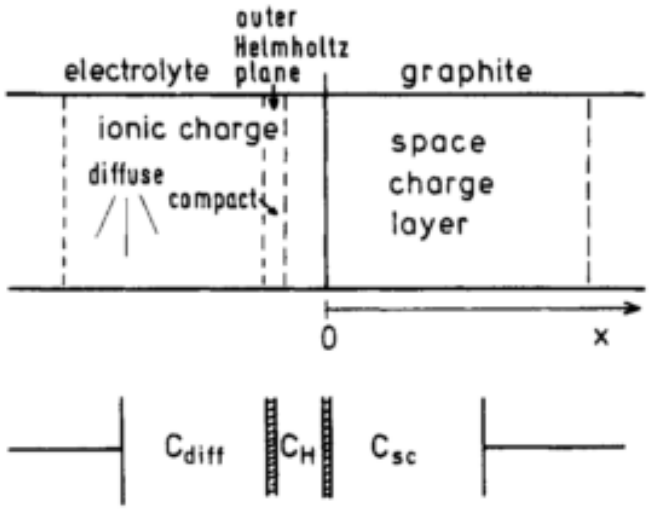

Figure 4. Illustration of the solution/HOPG interface and each type of capacitance, with a diagram of 3 series capacitors below.[32]

The model of the double layer structure described above is appropriate for most electrodes but does not accurately describe the observed minimum capacitance for HOPG. Now that HOPG has been established as the system to be studied, it is appropriate to describe its properties as an electrode in specifics. The most significant contribution to the minimum capacitance of HOPG is due to a space charge layer that exists in the HOPG.[32] Graphite is a semimetal, which means the density of states for HOPG is lower than the type of metal electrode for which the Guy-Chapman-Stern model was constructed. The charge in the HOPG electrode builds up across a space charge layer, much in the same way that the diffuse layer does. The dominant capacitance (smallest in

value) arises from this space charge layer. Therefore, our experimental capacitance must be modeled by equation 3, which shares the same subscripts as figure 4.

$$\frac{1}{C_{exp}} = \frac{1}{C_{diff}} + \frac{1}{C_H} + \frac{1}{C_{sc}} \quad [3]$$

1.1.3 Soil Water Repellency

Another system in which the properties of the solid - liquid interface are of importance is the soil - water interface. A better understanding of this topic will inform erosion control efforts, increase water uptake in agricultural applications, and help in understanding the natural phenomenon of soil water repellency.[33] The topic of water repellency of soil has a broad impact, especially for environmental concerns like pollution and climate change.[34-35] Many studies have tried to determine contributing factors to soil water repellency, and the phenomenon has proven to be multifaceted and difficult to describe.

Part of the difficulty with studying soil is the number components. Soil contains both mineral content and organic content. The mineral content can be classified by particle sizes with powder-like, sand-like, and gravel-like all being included (more technical definitions exist but are outside the scope of this document). The same is true of the organic component; molecules with wide a range in molecular weight, bacteria, plant matter and animals all fit this definition and must be considered. Soil also has internal structures. Aggregates can form that may have different internal properties than the surface.[36] Regions of preferential flow can form where large amounts of soil (*i. e.* kilograms) are isolated from the water flow.[37] It is also known that the amount of rain an area experiences can affect repellency. Soils can remain wettable until a certain threshold is reached, where a lack of rain favors the formation of repellent aggregates.[38] All of these

phenomena are well described and are often included in discussions of soil water repellency.[33] For the purposes of this work, we will exclude further discussion that involves aggregate effects, and focus on the chemical nature of the majority components of soils.

1.2 Characterization of Surfaces and Interfaces

1.2.1 Electrochemical Impedance Spectroscopy

One method for probing this contamination is to test the electrical response of the system. Electrochemical impedance spectroscopy (EIS) is a useful tool for understanding the electronic properties of a system.[19, 39] A typical 3 electrode system is used, where the counter electrode's surface area is large compared to the working electrode, and a reference electrode (*i.e.* Ag/AgCl) is used as a standard for cell potential. EIS measures both the resistive and capacitive impedance response of a system when an AC current is applied. The voltage of the AC signal is typically constant for a single EIS experiment. The response of the system is then measured over a range of frequencies, typically between 1 Hz and 100 kHz. Higher frequencies risk much more error in the measurement.[40-41] AC bridge circuits are used to determine resistive and capacitive impedances separately. The resulting data is plotted by one of two methods: a Bode plot or a Nyquist plot. A Nyquist plot's two axes are the real and imaginary impedances; which correspond to resistive and capacitive impedances, respectively. A bode plot superimposes two variables on a single graph. They are the total impedance, and the phase angle. The x-axis is shared, and is the frequency. An example of such data can be seen in figure 5.

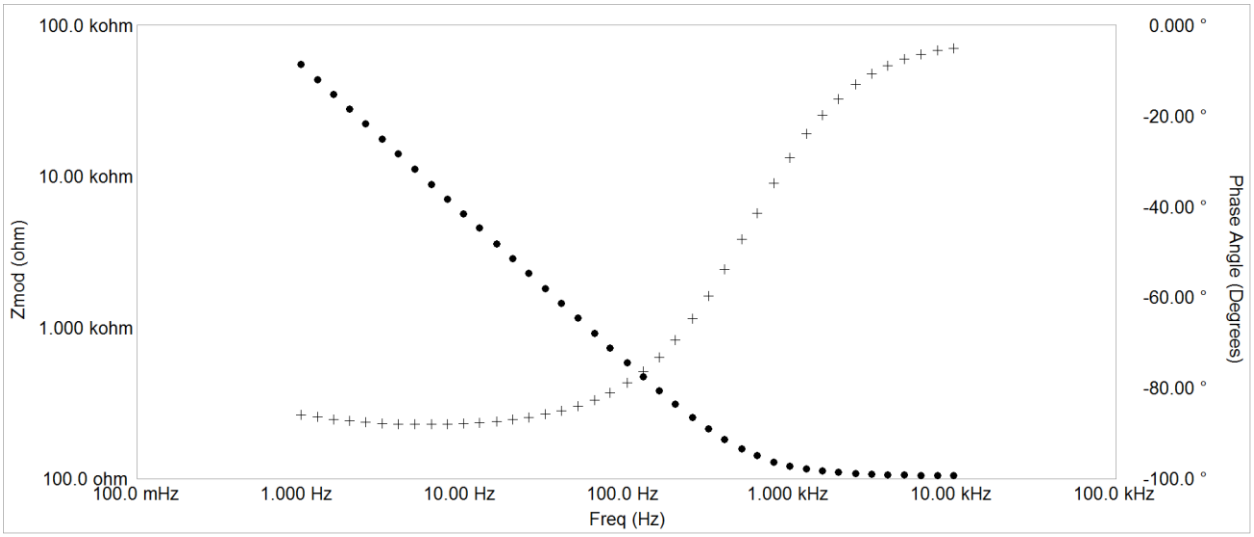

Figure 5. Sample bode plot. Dots are impedance data, and pluses are phase angle. There are two separate y-axis scales compared with the same x-axis. Both the impedance, and frequency axes are on a logarithmic scale.

A model is then developed to imitate the response of the system. The model's parameters are then optimized to mirror the experimental data as closely as possible. These parameters can then be used to compare with the physical phenomena of interest. The equivalent circuit model is not meant to describe the interface phenomenologically, but simply replicate the measured properties and approximate the surface behavior.[42] While the equivalent circuit is empirical in nature, care must be taken to limit the number of circuit elements to the smallest amount needed to appropriately describe the surface. A commonly used standard is that if the χ^2 value (a measure of the goodness of fit) is reduced by a factor of 10 by the addition of a new circuit element, then the new addition is warranted.[43] Although it is common to rely on literature precedent when studying a system, it is apparent that applying this standard is best done when building a new model. Therefore it is preferable to use a building up method when determining the most appropriate equivalent circuit for the impedance spectrum.

There are two models that can appropriately describe the system in question with minimal complexity. A simplified version of the Randle's cell fits well to most electrodes.[44] In some cases, a constant phase element (CPE) can be used to establish a better fit to the data.[45] The constant phase element replaces the capacitor in Randle's cell. An electrochemical cell that is low enough in voltage that no chemical reaction occurs can be modelled by the circuit in figure 6.

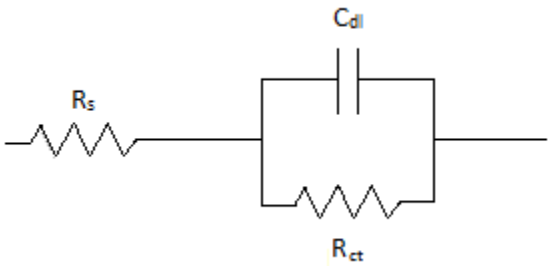

Figure 6. Simplified Randles cell equivalent circuit. R signifies a resistor and C a capacitor.

R_s is the resistance of the solution and all wiring and connections, R_{ct} is the charge transfer resistance, and C_{dl} is the capacitance of the electrical double layer. Often, a Warburg element will be included in the equivalent circuit model. A Warburg element is usually associated with linear diffusion, which has its largest impedance at high concentrations and very low frequency.[19] Thus, we can remove it from our model while maintaining a good fit with the proper experimental conditions. While the capacitor in our equivalent circuit will give us an appropriate fit, we can obtain a much better fit with a constant phase element (CPE). The definition for the impedance of a constant phase element has been proposed in several different forms; equation four is our chosen definition.[46]

$$Z_{CPE} = \frac{1}{Q(j\omega)^{\alpha}} \quad [4]$$

Here, j is the complex number $\sqrt{-1}$, ω is the angular frequency ($2\pi f$) and Q and α are the fit parameters. The units of Q are $\Omega \times s^{-\alpha}$, and α is unitless with acceptable values of $-1 \leq 0 \leq 1$.[47] Although the CPE will fit the data well, its physical meaning is lacking and the capacitance should be extracted from the fit parameters. The capacitance can be extracted using equation 5.

$$C = Q(\omega''_{max})^{\alpha-1} \quad [5]$$

C is the capacitance of the circuit element in farads, ω''_{max} is the frequency at which the capacitive (imaginary) impedance is at a maximum, and Q and α are as previously described.[48] Though other values generated by the model are also useful, the focus is on the capacitance for the current study. As seen in equation 1, the capacitance is not solely dependent on the intrinsic properties of the material, but also the surface area. For this reason, capacitance values must be quoted as C/A. The unit that translate closest to laboratory scale is $\mu F \cdot cm^{-2}$.

1.2.2 Spectroscopic Ellipsometry

A technique that is useful to measure the thickness of thin layers is spectroscopic ellipsometry (SE).[49] SE directs polarized light to a sample, and measures the reflected light. The change in polarization that occurs in the light after reflection can be used to gather data about the surface of the material. The two properties of reflected light that are measured are the phase difference (Δ), and the amplitude ratio (Ψ).[50] The phase difference is the change in the angle of polarization between the source and the measured light, and the amplitude ratio is the ratio of the respective amplitudes. The phase difference of the light is illustrated in figure 7.

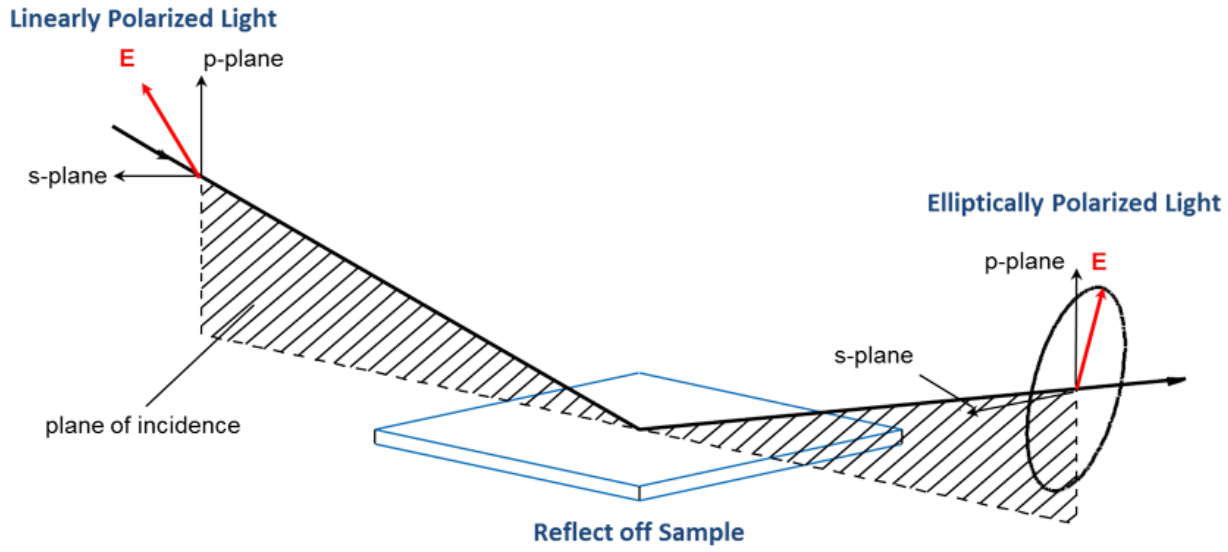

Figure 7. Example of an ellipsometry measurement. Source light is on the left, measured light is on the right. (From https://www.jawoollam.com/wp-content/uploads/ellipsometry-definition.png)

Elliptically polarized light is the most common form and is the namesake of the technique of ellipsometry. The polarized light source is projected onto the surface at a known angle relative to the plane of incidence. The measured light is typically elliptical, and its polarization state is determined by a rotating polarizer. It is customary to refer to light along each axis as either s-polarized or p-polarized. The letters are carried over as a convention from the original publication in German; s signifies perpendicular and p parallel to the material studied. [51]

Though Δ and Ψ are the measured quantities, they are somewhat removed from any the theoretical models that describe light.[52] To interpret the physical meaning of these parameters, we must start with a discussion of Snell's law. When there is an interface between two materials

$$n_i \sin(\theta_i) = n_t \sin(\theta_t) \quad [6]$$

and light impinges upon the interface, the refraction and reflection of light is governed by Snell's law. Here, n_i and n_t are the refractive indices of the two media, θ_i is the incident angle of the light and θ_t is the angle at which light enters the second material. An example can be seen in figure 8.

$$r_p \equiv \frac{E_{rp}}{E_{ip}} = \frac{n_t \cos\theta_i - n_i \cos\theta_t}{n_t \cos\theta_i + n_i \cos\theta_t}$$

$$r_s \equiv \frac{E_{rs}}{E_{is}} = \frac{n_i \cos\theta_i - n_t \cos\theta_t}{n_i \cos\theta_i + n_t \cos\theta_t}$$

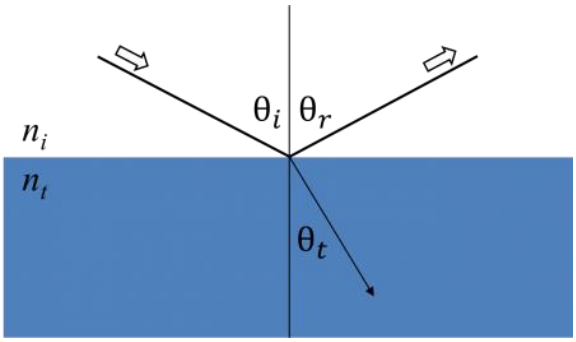

Figure 8. On right, illustration of Snell's law of refraction. On left, Fresnel's equations describing the behavior of reflected light. (from: https://www.jawoollam.com/resources/ellipsometry-tutorial/interaction-of-light-and-materials)

Related to Snell's law is a set of equations describing the effect of reflection and refraction on the polarization state of light. These equations are known as Fresnel's equations.[53] The two parameters from Fresnel's equations that are of interest for ellipsometry, r_s and r_p, can be seen in figure 8. These values are the ratio of incident light to reflected light at either polarization state. There are other similar equations for the refracted light, but since ellipsometry only deals with reflected light, only r_s and r_p are of interest. These values are connected to the measured values by the relation in equation 7. The values r_p, r_s, Δ, and Ψ are as previously

$$\rho = \frac{r_p}{r_s} = \tan(\Psi)\, e^{i\Delta} \qquad [7]$$

defined, and i is the imaginary number. The value ρ is typically how ellipsometric raw data is quoted, as it is influenced by all the changes to the light by interacting with the system. Here is where the properties the reflected light are connected to the properties of the material.[54] Yet, though we have made this connection, only information on pure materials can be extracted from this relation. As we have before with EIS, we must again construct a model with which to compare our experimental data.

Unlike equivalent circuit modelling, in ellipsometry the model must have true physical meaning. For EIS, the properties of some bulk virtual material can be useful, but for ellipsometry the strength of the investigative technique lies in its ability to determine the depth of a thin layer. This can only be determined through the application of a model like that of figure 9.

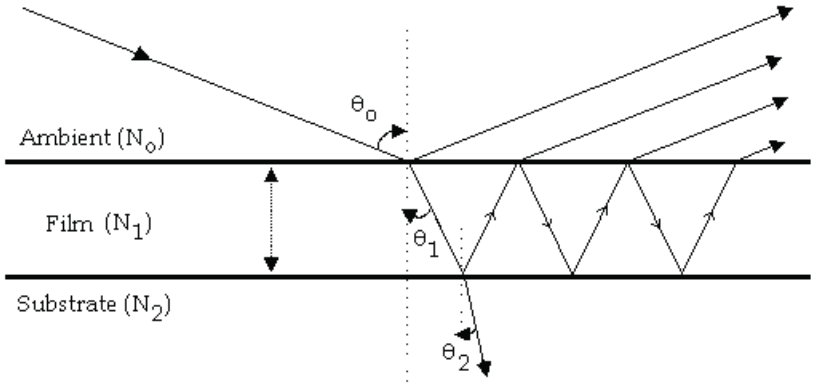

Figure 9. A model of a thin film on a substrate. The thin lines represent the direction of travel of light beams, and the thick lines an interface of two substances. The angle of reflection or refraction is represented by θ.[55]

For this example, four reflected beams can be seen. To the detector, they will be read as a single beam of light. The resultant beam is a combination of many. The light will have a different intensity and a different value of ρ depending on the properties of the film. A computer algorithm is used to calculate the resultant light beam once all are combined. The thickness and optical constants of the film can be determined in this step.[55] Some substrates are uniform enough in their optical constants that they can be referenced for the calculations, but HOPG will have a wider range in optical properties with each exfoliation. Therefore, its optical constants must be determined before the growth of the film.

The model used for this study consists of a Cauchy layer, and a B-spline layer. The Cauchy model is most useful for samples that are highly transparent for the wavelengths chosen.[56] Hydrocarbon contamination is fitted to this model. As seen in equation 8,

$$n(\lambda) = A + \frac{B}{\lambda^2} + \frac{C}{\lambda^4} \quad [8]$$

the Cauchy relationship correlates the wavelength of light to the refractive index of the material. The extinction coefficient is assumed to be 0 for the Cauchy model. The parameters A, B and C are fit via least squares to the data.

As previously stated, HOPG must have its optical constants determined before measuring the thin film. This is accomplished by taking a measurement and modelling the optical constants to the data via the B-spline function. A B-spline function is appropriate for materials whose properties are not of immediate importance to the experiment, and can be modelled as a virtual material.[57] B-spline, short for basis spline, is a stepwise function. The function is broken to enough pieces that the data can be modeled by several functions stitched together.

The nature of an electrochemical capacitor requires an interface with a liquid, and this fact complicates ellipsometry measurements. A special piece of equipment designed by the manufacturer of the instrument must be employed to study this interface in the same aqueous environment in which all of our EIS testing is conducted. Seen in figure 10, the liquid cell allows us to take these measurements while compensating for the effects of an aqueous ambient.

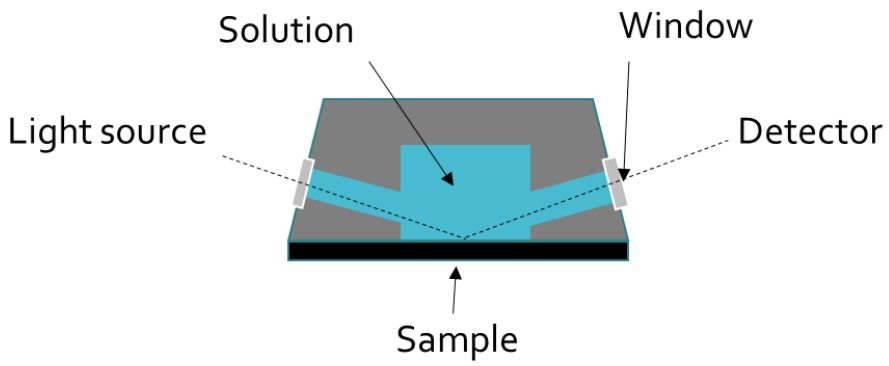

Figure 10. Cutaway illustration of the liquid cell used for ellipsometric measurements. The blue region is the liquid ambient, the gray region is the device in question, and the black area is the sample.

1.2.3 Fourier Transform Infrared Spectroscopy

An FTIR spectrophotometer measures the absorbance or percent transmittance of a material over a specified range of frequencies. Typically, the range is between 400-4000 cm^{-1}. This range is used because it is the region in which most bond vibrations of interest absorb. FTIR was developed as an alternative to frequency dispersion techniques. In most other methods of analysis, each individual frequency must be recorded separately, but an FTIR gathers information about all frequencies at once. This is accomplished by the use of an interferometer. Originally developed to measure a supposed "Luminiferous aether", the Michelson interferometer is still used in modern science.[58] The interferometer is illustrated in figure 11.

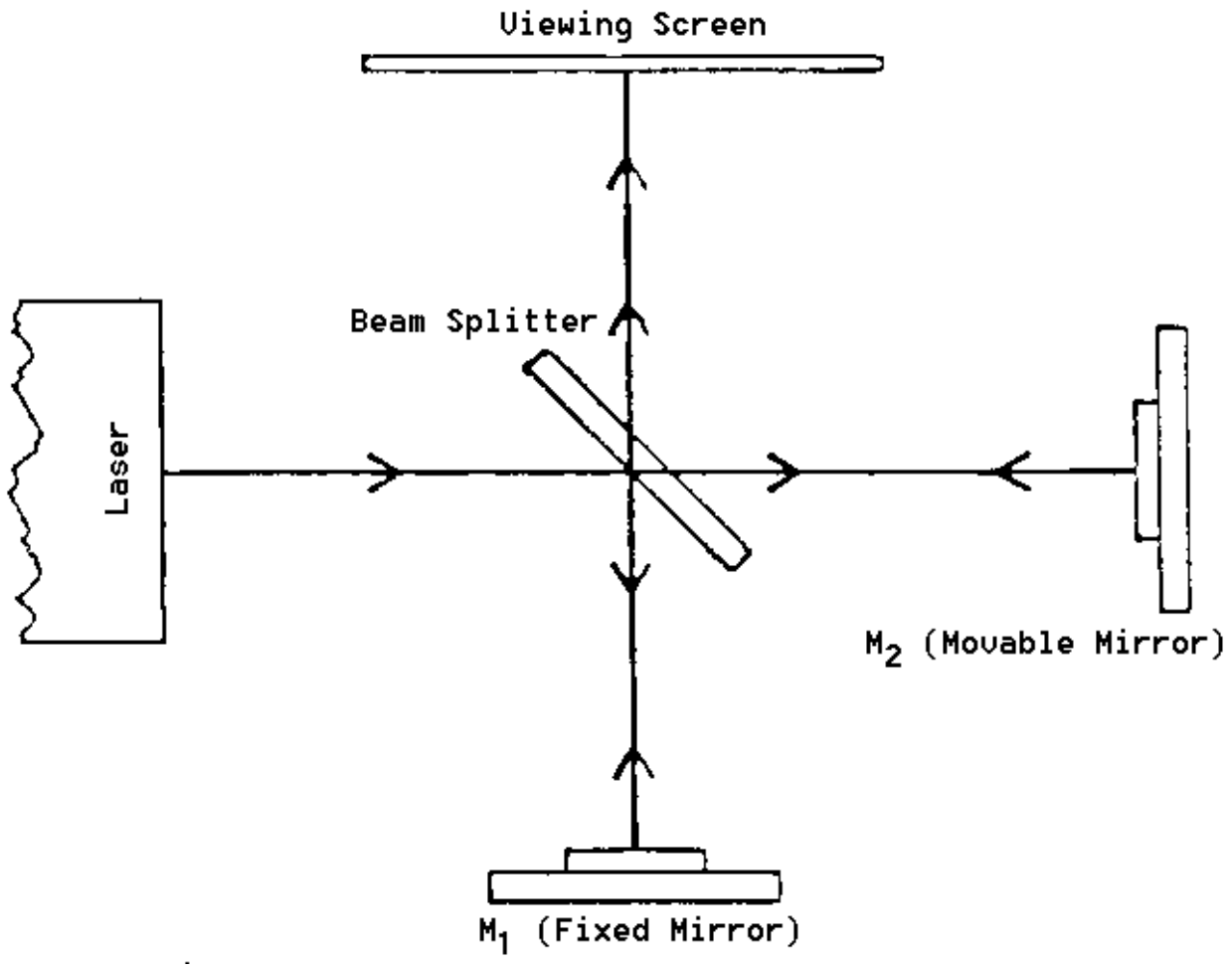

Figure 11. A diagram of a Michelson interferometer. Arrows denote the direction of a light beam. (from http://felix.physics.sunysb.edu/~allen/252/PHY251_Michelson.html)

An interferometer creates a pattern of constructive and destructive interference. A cohesive beam of light is sent through partially reflective beam splitter. The light is split in half and sent to two different mirrors. One mirror is moved, and one is kept stationary. The two beams of light then recombine at the beam splitter after having travelled different path lengths. Light of the same wavelength then either constructively or destructively interferes depending whether they are in or out of phase. The interference pattern created carries information on all of the wavelengths of light being studied. The generated data is called an interferogram. An interferogram is a time domain

measurement (intensity vs. mirror position). The raw data generated must be mathematically transformed into frequency domain (intensity vs. wavenumber). The method used is called a Fourier transform.[59] The resultant spectrum can then be analyzed to determine chemical information.

Molecular motions, such as bond vibrations and molecular rotations, are associated with the infrared region of the electromagnetic spectrum. The change in energy of these molecular motions are specific to a particular functional group, and chemical environment.[60] For example: the region in which an O-H stretch occurs is different depending on whether or not there are hydrogen bonds present. Other functional groups have absorption regions that are well resolved from others, which makes them very easily identifiable (*i.e.* nitriles). Though FTIR is useful for functional group identification, it is much more cumbersome for identification of a whole molecule. The existence of overtones of bond vibrations makes positive identification much less straightforward.

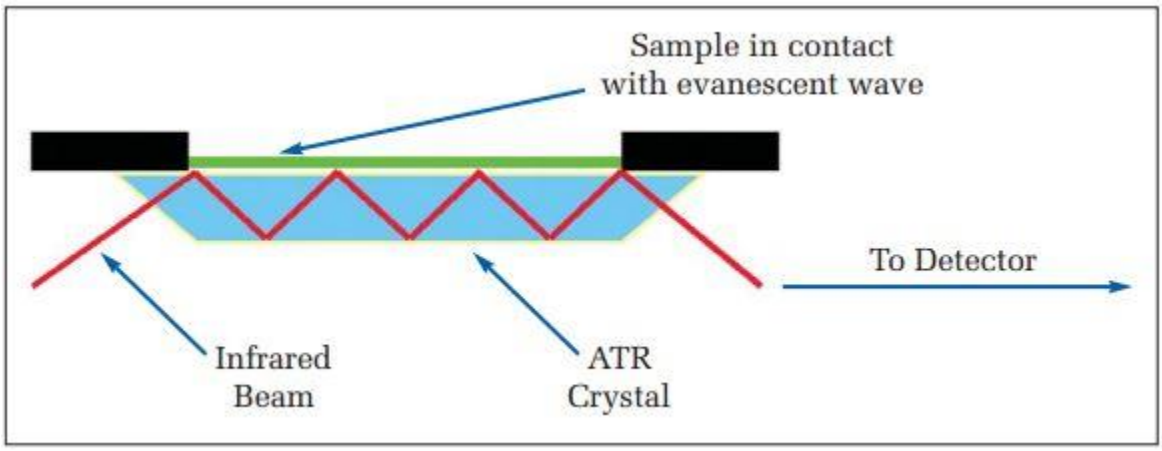

Figure 12. A visualization of attenuated total reflectance when a light beam strikes the interface of a sample and an ATR tip.[60]

In order to sample the surface of an opaque substance, traditional transmission spectroscopy is not appropriate. A special type of reflectance spectroscopy, attenuated total reflectance (ATR), is used. The technique works by bringing an optical crystal into contact with the surface to be measured. When light impinges upon the interface at an appropriate angle it can be totally internally reflected, and an evanescent wave can form. This affect can only occur if the crystal has a larger refractive index than the material being studied. The path length through the interface increases with more reflections and leads to more absorption from the analyte. The infrared beam will eventually reflect back into the crystal and will be directed to the detector. An illustration of the effect can be seen in figure 12.

1.2.4 X-Ray Photoelectron Spectroscopy

XPS is a technique that allows the measurement of elemental composition on a surface. Typically, the x-rays penetrate the first 10 nanometers of the surface. The preferential systems to be studied are surface coatings, thin layers of adsorbed materials, or systems where the electronic structure is of interest.

When X-rays impinge on a surface, they can interact with interior electrons and liberate them from the atom as a photoelectron. The kinetic energy of the photoelectron depends on the energy of the x-ray and of the electron's orbital. Therefore, it is possible to correlate the energy of the photoelectron to the identity of its source. A schematic can be seen in figure 13. Kinetic energy of photoelectrons varies enough between elements for XPS to be used as a characterization technique.

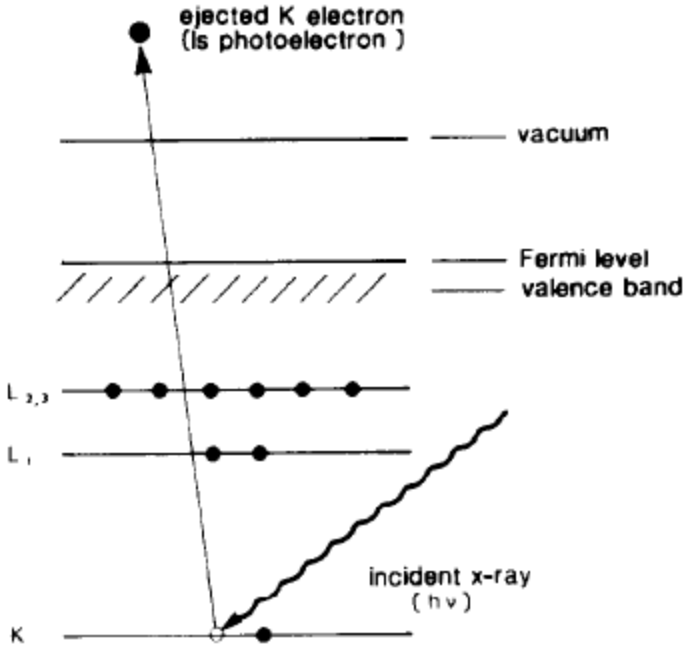

Figure 13. Visualization of the energy change of a photoelectron ejected from an atom. K and L are the x-ray notation for energy levels of n = 1,2 respectively.[60]

The relationship between the energy of the photoelectron (E_k), the energy of the x-ray ($h\nu$) and the work function of the detector (ϕ) is defined below as the binding energy (E_B).

$$E_B = h\nu - E_K - \phi. \quad [9]$$

E_B is the amount of energy it takes to remove an electron from the core shell of the atom. Since this value is material specific, it is where we obtain the identity of the element in question.

In order to gather information about the photoelectrons, they must be focused to an electron detector and be separated by energy. The energy analyzer separates the electrons by kinetic energy, and the detector generates a current from the electrons impacting it.

1.2.5 Water Contact Angle and Water Drop Penetration Time

Water contact angle (WCA) is an effective and convenient way of determining the free energy of a surface. Surface energy governs the interactions of one material with another. When a surface is studied in an environment of known surface energies (water and air) we can calculate the surface energy with the Young equation.

$$\gamma_{SG} - \gamma_{SL} - \gamma_{LG} \cos\theta = 0 \qquad [10]$$

In equation 10, γ represents the interfacial energy, and θ the angle between the surface and the water drop. The subscripts *S*, *L* and *G* signify solid liquid and gas, respectively. In this way γ_{SG} signifies the surface energy of the solid/gas interface. A diagram is provided below in figure 14 for clarity.

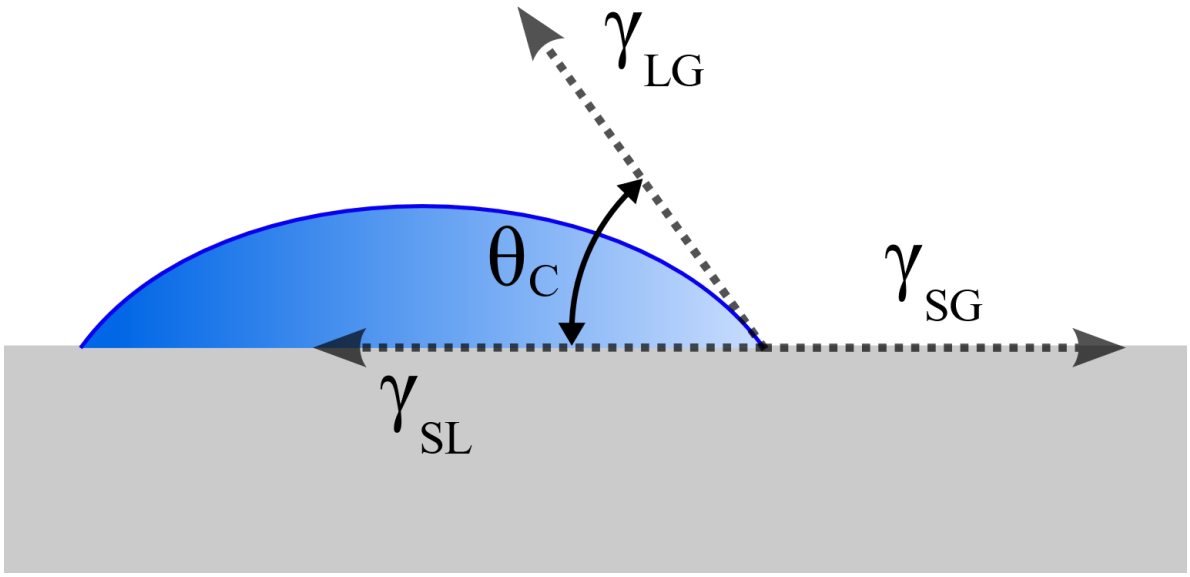

Figure 14. A diagram of a WCA measurement. The meaning of the variables is supplied in the text above.

We can use the WCA as a measure of how the surface energy has been changed by adsorptive processes. The calculation of the surface energy is not as important as the change in the WCA over time. Since hydrocarbon adsorption on typically hydrophilic surfaces tracks neatly with WCA, the angle itself is the measure we use.

The equipment used includes an optical camera, a syringe for dropping consistently sized droplets of water, and a level surface. A computer program is used to aid in the calculation of the angle of the water droplet.

Videos can also be used to determine water infiltration rates for powder or granular samples. These measurements are particularly useful for soil samples and other solid mixtures. The contact angle of these surfaces is difficult to define, as the water drop is in continuous motion. Using the water drop penetration time (WDPT) allows for a measurement of the water-substrate interaction when contact angle measurements are not feasible. Sometimes a sieve is required to increase homogeneity and it is suggested that the sample be air dried instead of oven dried to reduce error. For particularly hydrophobic soils, a varying ethanol concentrations in the water drops can increase the precision.[61]

1.3 Adventitious Hydrocarbons and Their Effect on Graphite and Soil

Adventitious hydrocarbon adsorption is an often overlooked contributor to surface properties. Understandably so, as many surface modifications are unaffected by this effect. However, when minor contributors are not considered, errors in understanding can compound and eventually lead to incorrect conclusions about the properties of any given surface. Herein lies the

purpose of this research, to establish hydrocarbon adsorption as one of these contributing effects so that communities outside of surface science can gain insight into their fields.

Graphite is used as both a supercapacitor electrode and a battery electrode. Even marginal increases in performance of these materials could translate to huge commercial profits. As the world strives to reduce its dependence on fossil fuels, these improvements are in high demand. The consequences of this shifting climate also influence other environmental concerns, such as soil water repellency. Contributing to a deeper understanding of water repellent soils will allow for more informed remediation techniques. Both of these topics are multifaceted, and in need of careful study. Herein it will be shown that adventitious hydrocarbon contamination is a contributing factor to water repellency in soils and the decreased efficiency of graphite as an electrode material.

2.0 Adventitious Hydrocarbons and the Graphite-Water Interface

2.1 Chapter Preface

The content of this section has been published in the journal *Carbon*.

List of authors: Justin M. Hurst, Lei Li, Haitao Liu

This paper reports the adsorption of airborne and waterborne hydrocarbon contaminants on graphite and their impact on the graphite-water interfacial properties. Exposing a freshly exfoliated highly oriented pyrolytic graphite (HOPG) surface to ambient air and 1-octadecene vapor (*ca.* 1 ppm) caused a *ca.* 30% and 70% decrease in its double layer capacitance, respectively. Similarly, a 38% decrease of capacitance was observed within 1500 min after a freshly cleaved HOPG was immersed in 1 M NaCl solution; liquid phase ellipsometry data showed that a contamination layer of *ca.* 0.6 - 2 nm was formed on the HOPG surface within the same time frame. The capacitance of a contaminated sample can be partially and temporarily restored by applying a high or low potential (-1.222 V or 0.778 V *vs*. Ag/AgCl). Herein we report that hydrocarbon contamination on graphite is significant in both water and air.

2.2 Introduction

Graphite has been a well-studied material going back to the early 1900's. Being a naturally formed allotrope of carbon, its intrinsic properties are of fundamental interest. Properties such as band structure, dielectric constant, double layer capacitance, and Raman spectrum are extensively

studied.[62-66] Graphite's inherent flatness has also made it useful for surface measurements.[67-69] Therefore, the intrinsic properties of graphite surface have been of great importance to the academic community and beyond.

Our group has shown that atmospheric hydrocarbons can adsorb onto graphite and mask its intrinsic wetting properties.[10] The water wettability of graphite was revealed to be intrinsically more hydrophilic than had been reported in the literature in the past 75 years. It was shown that when graphite was aged in laboratory air, the water contact angle increased within several minutes due to the airborne hydrocarbon contamination. Other work confirmed this effect for carbon and other materials.[27-29, 31, 70] Given the rapid kinetics of the airborne contamination, it should then be expected that a wide range of surface properties would also be unknowingly affected by this phenomenon. Any interfacial properties that are dependent upon the surface energy, dielectric properties, or chemical reactivity have the possibility of being influenced by the airborne adsorbates. In a recent study, Zou *et al.* showed that freshly exfoliated HOPG has a higher double layer capacitance (6.0 μF cm^{-2}) than that of HOPG aged in air for 24 hours (4.7 μF cm^{-2}).[71] They also observed that when a HOPG sample was immersed in 6 M LiCl solution, its double layer capacitance also decreased over time. These results are consistent with the idea that hydrocarbon contamination affects surface properties of HOPG other than wettability.

In the present study, we aim to expand on the results of previous works that show the adsorption of airborne organics and the effects on the graphite-water interface. Given the complex nature of the research topic, the goal of this study will be limited to (1) identify if airborne hydrocarbons remain on the graphite surface when in an aqueous environment; (2) determine if waterborne hydrocarbon contamination will occur at graphite-water interface; and (3) determine the kinetics of these processes and their impact on the double layer capacitance of graphite-water

interface. To accomplish these goals, we will use electrochemical impedance spectroscopy (EIS) and spectroscopic ellipsometry (SE) to characterize the HOPG-water/electrolyte interface. EIS will allow us to determine the double layer capacitance, which is a property that is heavily influenced by surface changes. SE will quantify the adsorbed contamination layer on the surface. We will also use Fourier transform infrared spectroscopy (FTIR) to characterize the organics adsorbed on the surface from air.

Our study highlights the effect of the contamination layer on the graphite-water interface. We characterize the growth of waterborne contaminants through both EIS and SE. The time resolution of our EIS and SE measurements permits a better understanding of when the contamination will begin changing electrochemical behavior. This data adds to the understanding of the dynamical behavior of both airborne and waterborne contaminants at the graphite-water interface.

2.3 Experimental Methods

2.3.1 Methods and Materials

A piece of 2 × 2 cm HOPG (SPI Supplies, SPI-2 grade) was prepared for experimentation by scotch tape exfoliation. Scotch brand tape was affixed to the basal plane of the graphite crystal, and was peeled off such that a fresh layer of graphite was exposed. High purity water (Thermo Scientific Barnstead "MicroPure" ultrapure water system, 18 MΩ×cm, < 10 ppb total organic carbon) was used for rinsing and making solutions. 1-octadecene (>90%, Sigma-Aldrich) was used for intentional contamination of the HOPG surface.

Electrochemical impedance measurements were recorded on a Gamry Reference 600 in potentiostatic EIS mode. Unless stated otherwise, the measurements were recorded at -0.222V vs. Ag/AgCl reference electrode with an AC perturbation between 10 - 20 mV in NaCl electrolyte solution (0.171 M or 0.984 M). Electrolyte solutions were prepared with NaCl from Sigma-Aldrich (>99.0%). Glassware was rinsed with piranha solution (3:1, H_2SO_4:H_2O_2), and 18 MΩ×cm DI water prior to use for electrolyte solution (*Warning: piranha solution presents an explosion danger and should be handled with extreme care; it is a strong oxidant and reacts violently with organic materials. All work should be performed in a fume hood. Wear proper protective equipmen*t). The electrochemical cell was constructed of a glass cylinder, and had a ~5 cm opening at the top where the counter and reference electrodes were inserted through a glass lid or rubber stopper. The cell was ~8 cm tall and had a small opening at the bottom where the HOPG was clamped (Appendix A, Figure 30). The area of the working electrode was determined by a Viton o-ring which was 0.988 cm^2. A platinum wire was used as the counter electrode and the reference electrode was Ag/AgCl (Accumet 13-620-53). The capacitance of the HOPG electrode was determined by fitting the EIS data to a Randle's cell model with a constant phase element (CPE) in place of a capacitor. The capacitance was extracted from the CPE through the method detailed by Hsu and Mansfield.[72] Detailed information about the modeling of EIS data can be found in the supporting information.

Thin film thickness was determined by spectroscopic ellipsometry (SE). A J. A. Woollam Alpha-SE spectroscopic ellipsometer recorded data between the wavelengths 381 and 893 nm, at an incident angle of 70˚. A 500 μL liquid cell was used for liquid phase measurements. The cell is constructed of stainless steel and has quartz windows. A seal was created between the cell and the HOPG by a Viton gasket. The liquid was delivered by a glass syringe through a metal fitting. The

liquid cell, syringe, and fittings were treated with UV/Ozone prior to measurements. The window effects were calibrated using a silicon wafer with 25 nm thermal oxide (J. A. Woollam).

Fourier transform infrared (FTIR) spectroscopic measurements were taken using a germanium tip for attenuated total reflectance (ATR) on a Bruker VERTEX-70LS FTIR and a Bruker Hyperion 2000 FTIR microscope. Measurements were taken from 600 to 4000 cm^{-1} with a resolution of 4 cm^{-1}. The ATR tip was swabbed with isopropyl alcohol prior to measurements. At least 5 minutes was allowed for the isopropyl alcohol to evaporate before measurements were taken.

2.3.2 Air Aging

A petri dish was cleaned with DI water, then acetone and dried with air. The HOPG was exfoliated, then set in the petri dish and covered. It was then stored in air in a wet chemistry laboratory at various intervals prior to analysis by EIS.

In a separate experiment, the HOPG was aged in an open container. The HOPG was exfoliated then suspended in a beaker such that only the outer edges of the HOPG came in contact with the glass. The freshly exfoliated side of the HOPG was faced down in order to avoid particulate material from falling on the surface. In all air aging experiments, each individual EIS measurement corresponds to a separate exfoliation of the same HOPG sample.

2.3.3 1-Octadecene Aging

The HOPG was either measured within 1 minute of exfoliation, or aged through the following process: a vial cap (ca. 2 cm in diameter) was filled with 1-octadecene and placed in a

covered petri dish at room temperature to establish an atmosphere with high partial pressure of 1-octadecene (ca. 1 ppm). The HOPG was then placed in the petri dish and allowed to age at various intervals. For the EIS measurement, a rubber stopper was used to hold the counter and reference electrode, and 0.171 M NaCl was used as the electrolyte. Each EIS measurement corresponds to a separate exfoliation.

2.3.4 SE Liquid Phase Aging

HOPG was exfoliated, set up in the liquid cell and measured *in situ*. Either deionized water (18 MΩ) or 0.984 M NaCl was used as the liquid ambient. In both cases J. A. Woollam software CompleteEASE was used to analyze the data. The optical constants of the HOPG were determined by a b-spline model at the first measurement after the cell was assembled. The Cauchy model was used to model the properties of the contamination layer, and the thickness of the layer was extracted from the fitting.

2.3.5 EIS Liquid Phase Aging

The HOPG was exfoliated and assembled in the electrochemical cell with a glass lid. NaCl (0.984 M) was used as the electrolyte. The sample was then monitored in solution by EIS for several hours, with a frequency range of 1 - 10k Hz, cell potential of -0.222 V vs. Ag/AgCl, and a 10 mV root mean square AC perturbation. The capacitance of the HOPG surface was determined by fitting data to a CPE model (Appendix A, Figure 31); the details of the data fitting can be found in the supporting information. To verify the effect of contamination, the experiment was also

repeated while adding 3 drops 1.5% benzyl alcohol in 85 mL of electrolyte (concentration: 4.19 ppm).

To study the effect of electrode potential on the stability of the contaminant layer, the HOPG electrode was aged in electrolyte solution until the HOPG was in equilibrium with respect to contamination. The HOPG electrode was then conditioned for 300 seconds at either -1.222 V or 0.778 V (vs. Ag/AgCl). Following the conditioning, the double layer capacitance was monitored at -0.222 V vs. Ag/AgCl.

2.3.6 ATR-FTIR

HOPG was characterized by ATR-FTIR after being exposed to either air, or 1-octadecene vapor. For both experiments the sample was exfoliated, and the first measurement was conducted within 30 seconds. For air aging, the sample was then transferred to a covered petri dish and then FTIR measurements were repeated as a function of air aging time. Two spectra, 3 hours and 3 days aged, were from a separate exfoliation. They were included to give better time resolution. For the measurement involving exposure to 1-octadecene vapor, the same method as described in section 2.3 was used except the sample was exfoliated only once and repeatedly measured as a function of exposure time to 1-octadecene.

2.4 Results

2.4.1 Effect of Airborne Contamination on the Double Layer Capacitance of HOPG

Our first goal is to test if airborne hydrocarbons, after their adsorption onto graphite surface, would remain in an aqueous environment and if so, what is their impact on the properties of graphite-water interface. For this purpose, we have conducted gas phase aging of HOPG in laboratory air. A piece of HOPG was exfoliated using the scotch tape method, allowed to age in air, and then characterized by EIS. As seen in Figure 15A, the capacitance of the HOPG surface is dependent on the amount of time spent in air after exfoliation. One set of data shows an HOPG sample aged in a covered petri dish and for the other data set a sample was suspended with the exfoliated side down to ensure no particulates fell on the surface. In both samples, a decrease in the double layer capacitance was observed with longer air exposure; no significant difference in the kinetics was found. Note that each data point involves a separate exfoliation of the HOPG surface. The scattering seen in the data can be attributed to the difference in true surface area of the HOPG with each exfoliation, due to the microscopic flakes that remain on the surface.

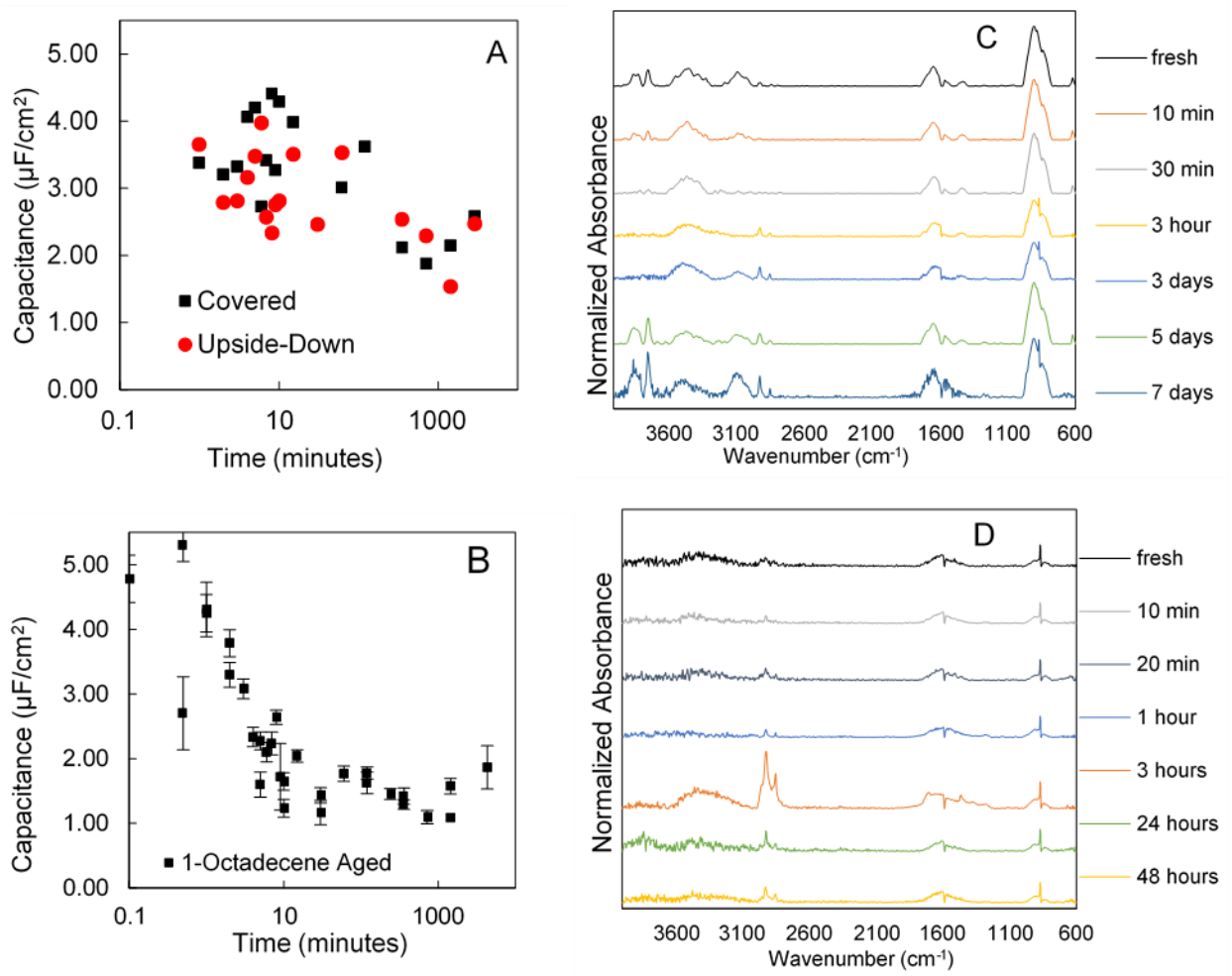

Figure 15. Effect of gas phase aging on the HOPG. (A) Air aging experiment in petri dish; (B) Air aging experiment with added 1-octadecene contaminant; ATR-FTIR spectra with (C) air aging and (D) aging in 1-octadecene. The error for individual data points in (A) is on the order of 0.001 μF/cm^2, too small to be seen in the figure. The scattering of the data in (A) and (B) may be attributed to variation in the true surface area, as each data point is a separate exfoliation.

Figure 15B shows the intentional contamination of HOPG with 1-octadecene vapor. These experiments serve as a positive control, to establish that hydrocarbon contamination can result in a decrease of double layer capacitance. A reduction of capacitance greater than *ca.* 70% occurred

within the first 10 minutes of aging in 1-octadecene vapor. After 10 minutes, the capacitance stabilized at *ca*. 1 - 2 μF/cm^2.

Verification of the identity of the airborne contaminants can be seen in the ATR-FTIR measurements in Figure 15 C and D. The peaks of interest are located at 2840 and 2930 cm^{-1}, corresponding to aliphatic C-H stretches.[73] It can be seen that for the air aging sample, there is a significant increase in the C-H stretching peaks after 3 days. For 1-octadecene aging, these peaks are noticeable after 3 hours. As in the case of air-aging samples, the C-H stretching peak intensity generally increases with longer exposure in 1-octadecene vapor. However, the spectrum acquired at 3-hr showed unexpectedly strong intensity; the exact reason is not known but we suspect that the inhomogeneity of the HOPG surface is the cause. This abnormally large intensity change was not reproduced in later experiments. The interpretation of this data is limited by the fact that the sample was not measured in the exact same location on the surface. Other notable features in the FTIR data include the peaks at 3100 and 880 cm^{-1}. Absorptions near 3100 cm^{-1} are associated with aromatic C-H stretches. Peaks at 880 cm^{-1} are likely out-of-plane bending modes for vinyl or aromatic hydrogens. It is worth noting that there is considerable dynamics in the FTIR data. For example, for the air aged sample, the 3100 cm^{-1} peak appeared at the very beginning of the measurement, its intensity decreased initially but eventually increased at longer exposure times.

2.4.2 Effect of Water-Borne Contamination

HOPG was characterized by SE to probe the surface contamination from water-borne contaminants. For liquid ambient SE measurements, a flow cell was used to contain the liquid. The HOPG surface was freshly prepared and immediately (< 30 s) assembled onto the liquid cell. The flow cell has quartz windows and an inlet for introducing the liquid. Figure 16A shows that a

significant layer of contamination builds up on HOPG even when in contact with ultrapure water produced by a Nanopure^{TM} water purification system. The thickness of the adsorbed layer increased quickly within the first 200 minutes, and then plateaued between 0.5 - 0.7 nm. It is likely that a monolayer amount of material was adsorbed during this process.

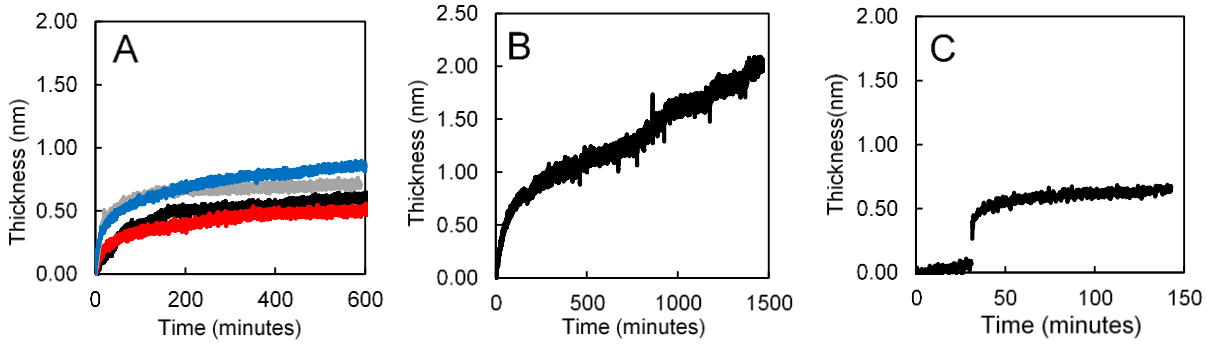

Figure 16. Liquid phase SE aging data. (A) several replicate measurements of aging of HOPG in pure water; (B) aging in electrolyte solution (0.984 M NaCl); (C) Aging of HOPG in pure water, with intentional contamination of stearic acid introduced at 30 minutes.

For a better comparison to the EIS data, HOPG was also characterized by SE in the presence of 0.984 M of NaCl solution. All parameters are the same as the pure water experiment with the only difference being the ambient solution. Shown in Figure 16B, the adsorption kinetics is similar to Figure 16A at early times. There is a change from fast to slow kinetics at *ca.* 200 minutes and at a similar thickness. However, the measured thickness kept increasing to *ca.* 2 nm, during which time the error of the measurement also continuously increased (Appendix A.5 Figure 32). It is likely that a secondary mechanism begins to influence the measurement; this is discussed in further detail in the supporting information.

In Figure 16C the HOPG surface was initially aged in pure water; saturated stearic acid solution (~1×10^{-5} M; ~3 ppm) was added to the flow cell at about 30 minutes. This experiment

serves as a positive control to show that hydrocarbons do adsorb onto water-graphite interface and such a process can be detected by SE. As expected, the thickness of the contamination layer rapidly increased after introducing stearic acid and plateaued at *ca.* 0.6 nm, similar to the ultrapure water experiment.

The effect of water-borne contamination on the double layer capacitance of HOPG can be seen in Figure 17. In this experiment, The HOPG was set up in the electrochemical cell and continuously measured by EIS in contact with 0.984 M of NaCl solution. A 38% decrease in capacitance occurred over 1500 min, with most of the decrease observed in the first 200 minutes. A similar test was performed with benzyl alcohol solution added to the electrolyte after a preliminary measurement of the uncontaminated surface. A capacitance decrease of 26% occurs when 3 drops of 1.5% v/v benzyl alcohol solution is added (final concentration: ~10^{-4} M). Curiously, the addition of benzyl alcohol solution does not depress the capacitance as significantly as the electrolyte solution alone. It could be that benzyl alcohol competitively inhibits adventitious organics from adsorbing to the surface. Since benzyl alcohol has a higher dielectric constant than most organics, it is possible that it increases the capacitance value when it adsorbs (see discussion below).

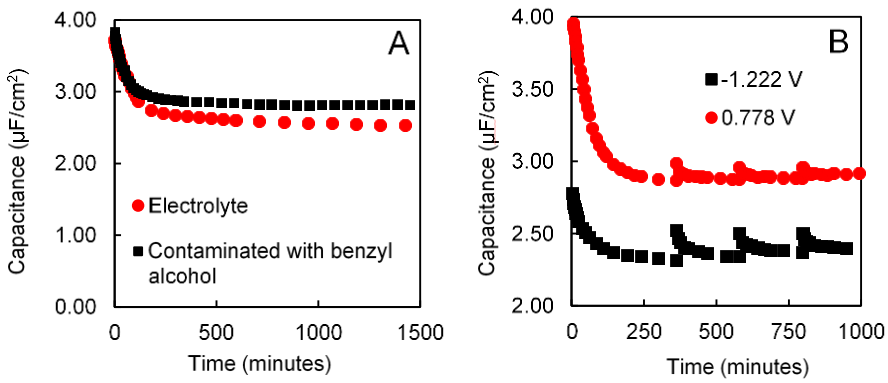

Figure 17. Liquid phase aging data measured by EIS. (A) Electrolyte solution and benzyl alcohol as an added contaminant. (B) Electrolyte aging, with potential "jumps". The potential jumps are either -1.222 V or 0.788 V for 300 seconds. Note, the vertical axis of (B) is on a truncated scale for visual purposes.

We also studied how the electrode potential impacts the adsorbed contaminant on HOPG. In this experiment, HOPG was cleaved and assembled in the liquid cell, then monitored by EIS at -0.222 V for about 375 minutes. The cell was then held at either -1.222 V or 0.778 V *vs*. Ag/AgCl for 5 minutes. The conditioning voltages were selected to avoid possible electrolysis of electrolyte solution while probing the effect of extreme electrochemical potential on the adsorbed contaminant. After 5 minutes of holding at -1.222 V or 0.778 V, EIS data acquisition then continued at -0.222 V *vs*. Ag/AgCl to monitor the capacitance. Capacitance "jumps" can be seen in the data presented in Figure 17B. The jump in capacitance is small, between 1% and 8%, with the negative holding potential yielding higher recovery.

2.5 Discussion

Previous studies found that airborne hydrocarbon contamination affects the surface of graphite and the impact of this contamination is significant within minutes after exfoliation. The data presented here agrees with these previous studies, and presents new evidence that adventitious hydrocarbons can also be introduced through the aqueous phase.

2.5.1 Gas Phase Aging

We observed a significant decrease of double layer capacitance after the HOPG was exposed to ambient air. The exfoliation of HOPG introduced some variability in the true surface area of the sample that we believe contributed to the large noise in the capacitance data shown in Figure 15A. However, despite the large variability, the overall trend is clear: increasing air exposure leads to a decrease of double layer capacitance of HOPG (Appendix A.2 Table 1). ATR-FTIR measurements showed that the graphite surface was contaminated by hydrocarbons, consistent with our previous observation of surface contamination of graphitic carbon in air.[9-14] The data shows that airborne hydrocarbon contamination is the likely cause for the decrease in the double layer capacitance.

As a positive control, we also found that exposing graphite to 1-octadecene vapor resulted in a larger decrease in the capacitance compared to the air-aged sample. For the HOPG sample aged in 1-octadecene vapor, the EIS data compares well with the kinetics established by Kozbial *et al.* through both SE and water contact angle measurements.[13] It can be inferred from the difference between air and 1-octadecene aging that environment will change the aging effect. Note

that the vapor pressure of 1-octadence is estimated to be 0.009 Pa (*ca.* 0.9 ppm) at room temperature.[74] If handled in an environment with volatile solvents present, HOPG could experience an even more pronounced decrease of double layer capacitance than noted in the present study.

It is difficult to use ATR-FTIR for analysis of the kinetics of adsorption. The composition and orientation of the adsorbed hydrocarbons may change over time. For example, small molecular weight aromatic hydrocarbons may adsorb rapidly at early times, then replaced by higher molecular eight aliphatic and aromatic hydrocarbons. Due to the conductive nature of HOPG, the surface selection rule will also affect the IR absorption of the molecules if their orientation changes: the vibration modes with an oscillating dipole moment parallel (perpendicular) to a conductive surface should be suppressed (enhanced), due to the presence of an image charge in the conductive substrate.[75-76] It is expected that both processes will strongly dependent on the aging time and local airborne hydrocarbon composition. Such a mechanism could explain the temporal variation of the 3100 cm^{-1} peak for the air-aged sample shown in Figure 15C; note that such behavior is not always observed, likely due to day-to-day variation in the airborne contaminants (Appendix A, Figure 33). In the same way, different types of contamination may impact the double layer capacitance to a different degree even if they show similar FTIR signatures. Thus, the kinetics measured by FTIR and EIS may not quantitatively reproduce each other. Nevertheless, the samples at long exposure times always show a much stronger -CH_2- stretching peak compared to the fresh sample, confirming the presence of hydrocarbon adsorption did occur on HOPG (Appendix A, Figure 34). Therefore, we limit our interpretation of the FTIR data only to the positive identification of hydrocarbons on the surface of graphite.

2.5.2 Solution Aging

Similar decrease of capacitance was also observed when HOPG is exposed to NaCl solution. These data showed much less variation, because the sample was exfoliated once and then continuously monitored, thus eliminating the variations of true surface area. Electrolyte solution with salt of >99.0% purity causes a large (33% of the initial value) drop in capacitance over the course of 24 hours (Figure 17A). Curiously, the addition of an intentional contaminant (benzyl alcohol) resulted in a slightly higher ending capacitance value than the electrolyte alone. It is most likely that this phenomenon can be explained by the difference in dielectric constant of benzyl alcohol and other hydrocarbons. The adsorption of benzyl alcohol increases the dielectric constant of the contamination layer and alleviates some of the capacitance losses (see *Qualitative analysis* section below). Also shown is the effect of voltage conditioning on the cell, which resulted in a small increase of the double layer capacitance (Figure 17B). Among other possibilities, the data is consistent with the idea that the contamination layer is partially driven off of the surface, recovering a small percentage of the original capacitance. We speculate that the contaminant may change its charge state or solubility due to redox reactions and/or local pH changes induced by the potential. However, the capacitance of the surface then is quickly driven down again by re-adsorption for little to no permanent improvement.

SE data collected in the electrolyte solution shows an increase in the thickness of the adsorbed layer that matches the kinetics of capacitance reduction well. SE data collected in pure water shows a similar effect, but with a thinner contamination layer. Although SE does not confirm the identity of the layer, it does provide information on the existence, and the thickness of the contamination layer. Similar liquid-aging experiments were also carried out using air-aged HOPG (Appendix A, Figure 35). We found that in pure water, the air-aged sample showed a slower

growth of contaminant layer; however, in NaCl solution and with intentionally added stearic acid, the air-aged sample showed similar behavior as the fresh-exfoliated sample. Additional studies are needed to fully understand this complex behavior.

2.5.3 Qualitative Analysis

The observed decrease of double layer capacitance is significant in magnitude and highly sensitive to the environment. As an example, exposing graphite to *ca.* 1 ppm of 1-octadecene vapor resulted in 70% decrease in the double layer capacitance. The change in the capacitance can be attributed to two factors, as discussed below.

First, the hydrocarbon contamination would increase the charge separation in the double layer and hence decrease the double layer capacitance. The hydrated ions in the double layer is in intimate contact with the electrode surface, therefore, the distance between the ions and graphite electrode would then be significantly increased if a monolayer of hydrocarbon was inserted in between. Capacitance has an inverse relationship with distance between charges. The ion-electrode separation can be estimated to be about 0.8 nm.[77-78] Using the plate capacitor model, one expects that increasing ion-electrode separation value by 0.7 nm (Figure 16) would decrease the double layer capacitance by about 50%. The second item of concern is the dielectric constant. The room temperature dielectric constant of water is about 78, and 1 M NaCl solution is about 70.[68-69] Most organic materials have a much lower dielectric constant (*e.g.,* 1-octadecene has a dielectric constant of approximately 2, which is typical for hydrocarbons[79]), which would also reduce the double layer capacitance proportionally.

The above analysis would predict a *ca.* 70-fold reduction of double layer capacitance, much larger than what we observed. A key factor that we did not consider in the analysis is the low

carrier density of graphite. Graphite is a semi-metal with low density of states near its Fermi level. In a double layer structure, the counter charges in graphite are not localized at the graphite-water interface; instead, these counter charges are distributed several to several tens of nanometers within the surface. Therefore, the effective charge separation distance is longer than the ion-graphite separation; in the same vein, the effective dielectric constant will have a contribution from graphite. Both factors make the impact of surface contamination much less than predicted by the simple model we described. Work is under way to quantitatively model the double layer structure in the presence of contamination.

2.6 Conclusion

The data presented here increases the community's understanding of the dynamical behavior of the contamination layer at the graphite water interface. This study shows that trace amounts of hydrocarbons from the atmosphere, water, and electrolyte can significantly contaminate the surface of HOPG within as little as 10 minutes of exposure. Contamination from the electrolyte reduced the differential capacitance by as much as 30%, and in the case of airborne contamination by more than 70%. ATR-FTIR confirmed the presence of hydrocarbons on the HOPG surface upon air exposure. Liquid phase SE experiment showed that a contamination layer of 0.6 nm – 2 nm formed on HOPG upon contact with water and electrolyte solution. We hope that a better understanding and controlling of the surface cleanness of graphite may lead to a reassessment of some of the well-known properties of graphite and discovery of new applications. For more discussion on the cleanliness of carbon electrodes, refer to Appendix C: "Assessing and Mitigating Surface Contamination of Carbon Electrode Materials".

2.7 Acknowledgements

This work is supported in part by ONR (N00014-15-1-2520).

3.0 The Ionic Liquid-Graphite Interface

3.1 Introduction

A recent advance in electrochemistry is the utilization of room temperature ionic liquids (RTIL) for electrochemical energy storage devices. RTILs are good for energy storage because of their chemical stability, large potential window, and thermal stability. Ionic liquids exist as two charged organic species. This allows the anion/cation pair to be a solvent free electrolyte. These advantages are balanced by low ion mobility and high resistance between electrodes.

An attractive combination with RTILs is a carbon electrode. Carbon is lightweight and conductive and is a suitable battery electrode for batteries and capacitors that need a large specific energy. Carbon electrodes have a rich history in electrochemistry and are well studied for aqueous solutions. With the introduction of RTILs new theories were developed to explain the RTIL/electrode interface. The Kornyshev theory of the RTIL/electrode interface matched well for metallic electrodes, and is still quite successful.[80] Experimental capacitance vs. potential curves showed the same shape predicted by Kornyshev theory.[81]

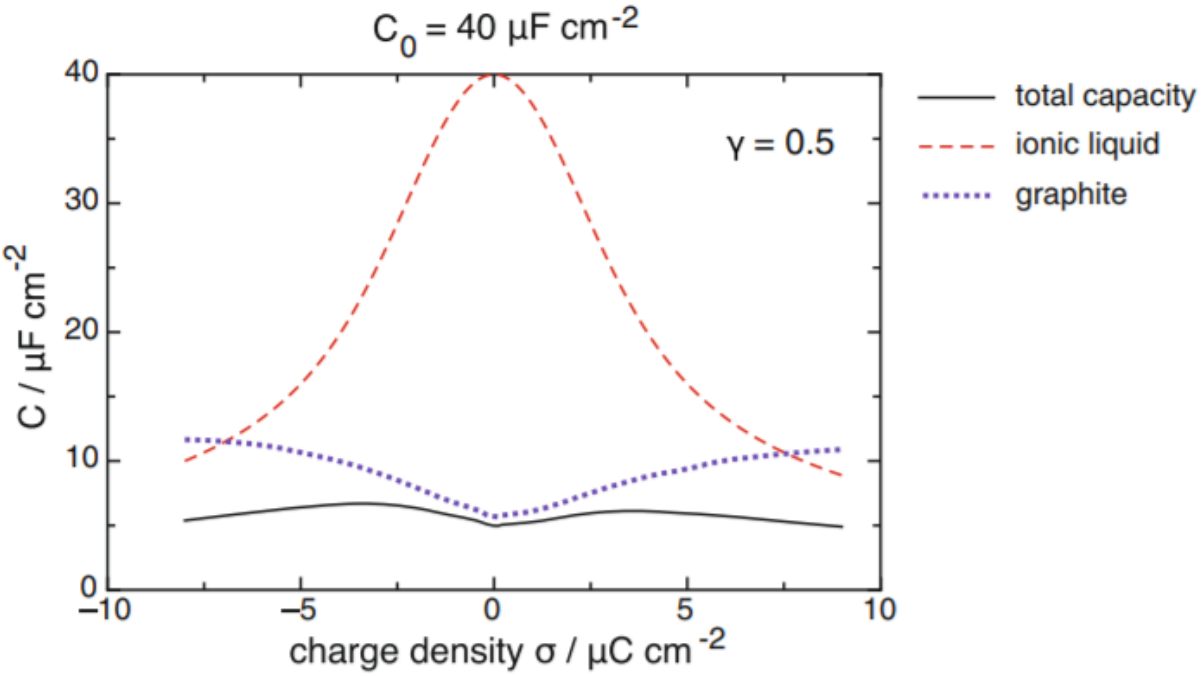

Figure 18. The charge density dependence of the capacitance of the RTIL-graphite interface as calculated by Kornyshev theory. Reprinted by permission from *Journal of Solid State Electrochemistry*, **2014**, *18 (5)*, 1345-1349. Copyright Springer Nature (2014).

There is a further complication with carbon electrodes. The minimum capacitance for graphitic carbon is known to be limited by a space charge layer within the graphite itself.[32] So graphitic carbons electrodes cannot be sufficiently described by Kornyshev theory, but must make considerations of semiconductor theory as well.[82] This work was completed by Kornyshev *et.al.* in 2014.[83] Their calculations are reprinted in figure 18. The capacitance of the RTIL/metal interface is limited by the RTIL, where overcrowding lowers the capacitance at high potentials. For graphite, the space charge layer becomes more compact at higher potentials, and therefore raises the capacitance. This behavior is seen in aqueous systems and was predicted for an RTIL solvent as well.

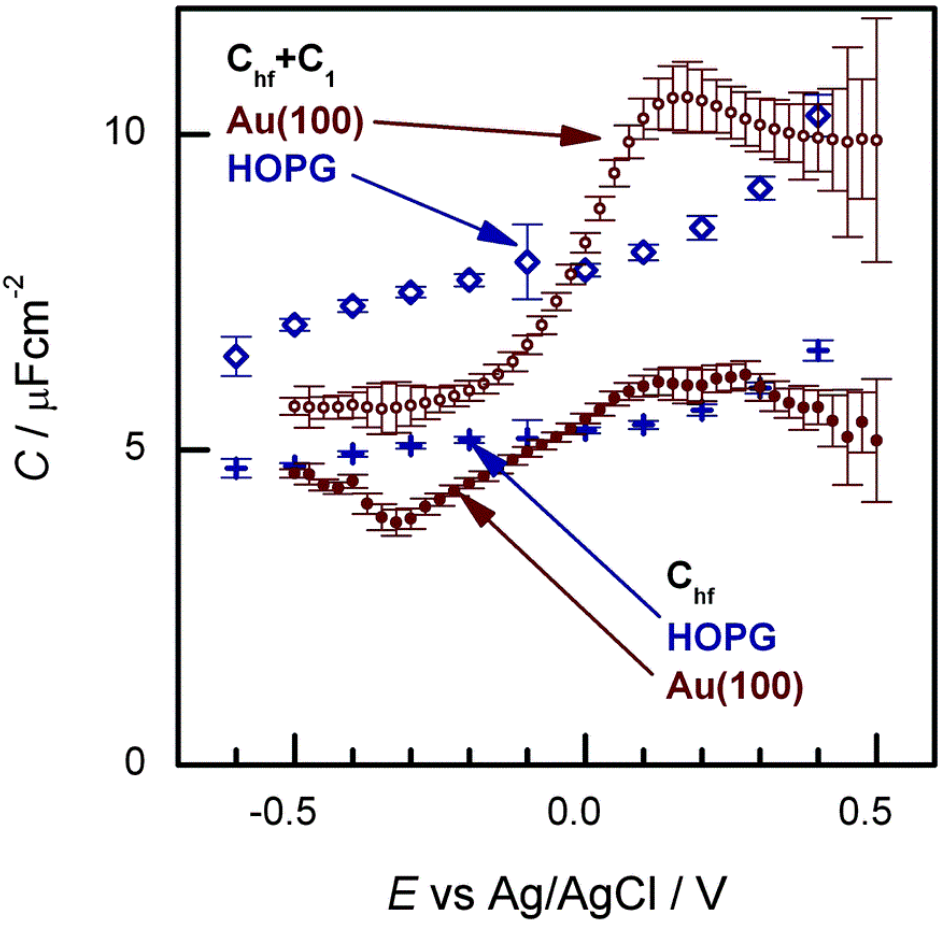

Figure 19. The capacitance curve of graphite and BMIM PF_6. Reprinted by permission from Physical Chemistry Chemical Physics. **2016**, *18*, 920. Copyright 2016 Royal Society of Chemistry.

Surprisingly, Muller *et al*. found that carbon electrodes did not follow the predicted pattern.[84] In this work, they found that the capacitance curve followed a sigmoid shape. This data is reprinted in figure 19. If semiconductor theory is best used to explain the surface capacitance of graphite, then it would follow that both aqueous and RTIL electrolytes would show a similar capacitance vs. potential curve. Especially at the minimum capacitance near the potential of zero charge (PZC), where RTIL overcrowding cannot explain a capacitance reduction. There remains

a discrepancy between theory and experiment that must be explained to fully understand the RTIL/nonmetallic electrode interface.

It has also been shown that adventitious hydrocarbons can adsorb to the surface of graphite and mask its intrinsic surface properties.[27, 85] Previous works start with the assumption that this behavior is not significant, and do not mention it as a consideration. This gap in understanding must be addressed.

We will investigate by comparing capacitance vs. potential curves for 1-butyl-3-methylimidazolium hexafluorophosphate (BMIM PF_6) in various experimental conditions. Comparing ambient atmospheric measurements at various levels of cleanliness will allow a baseline of comparison to measurements in a glovebox, and in a clean hood. We will also study the effects of these environments on the interface at the potential of zero charge (PZC).

3.2 Methods

The first step in this process is to make an appropriate reference electrode (RE). In most aqueous solutions, commercially available REs function well enough. Since the electrolyte is the solvent for RTILs, one universal RE system will not do, as using different RTILs for the electrochemical cell and the RE is certain to introduce error. This means that a new RE must be made for each individual RTIL. Another consideration is the redox couple. Ag/AgCl REs are commonly used for aqueous systems, but is has been shown that the Ag/Ag^+ standard is more appropriate for RTILs.[86]

An appropriate model must also be made, such that the impedance spectra can be accurately fit, but that the elements can be traced to a physical phenomenon. The most basic model, a Randel's

cell, fits fairly well for some aqueous systems but not for ILs. A second capacitor is usually needed to explain the high frequency behavior of the graphite IL system. The model used for this work is seen in figure 20 below.

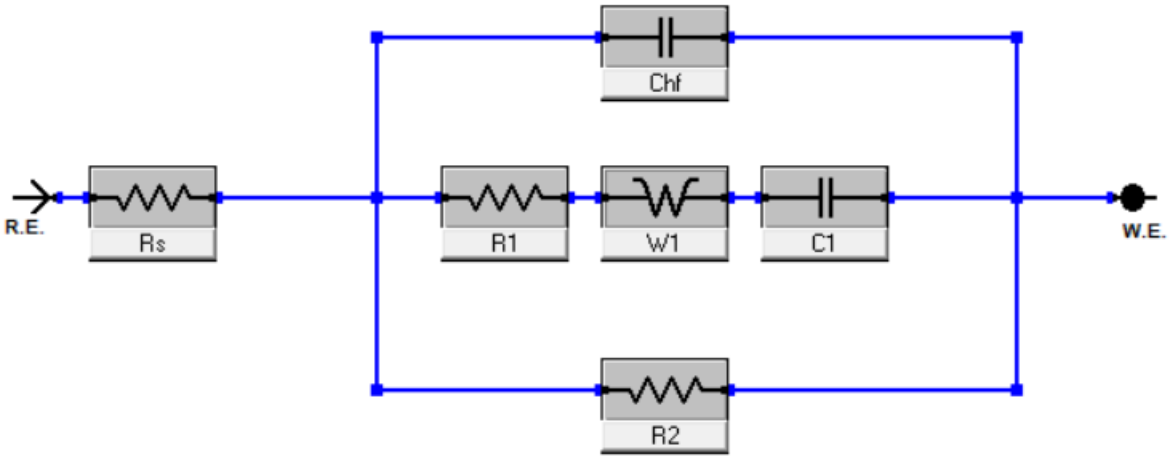

Figure 20. The model used as an equivalent circuit for the extraction of capacitance from an impedance spectrum.

The resistances are described as the resistance of the solution, Rs, the charge transfer resistance (or also can be thought of as the resistance associated to the leakage current), R2, and the resistance associated with the formation of the double layer, R1. Chf describes the high frequency behavior of the system, and C1 is the double layer capacitance. A Warburg element is also included, and could be attributed to the ordered structure that occurs at the interface.[87]

3.2.1 EIS Measurements

Impedance spectra were measured by a Gamry Reference 600. A glass cell was used to contain the solution and electrode. The electrochemical cell was constructed of a glass cylinder,

and had a ~5 cm opening at the top where the counter and reference electrodes were inserted through a glass lid or rubber stopper. The cell was ~8 cm tall and had a small opening at the bottom where the HOPG was clamped as seen in Appendix A Figure 30. The area of the working electrode was determined by a Viton o-ring which was 0.988 cm^2. The reference electrode was constructed of a glass cylinder and a frit attached by a shrink-wrapped plastic. For our system $AgPF_6$ is added to $BMIMPF_6$ such that a saturated solution is made. This solution and a silver wire are then placed in a glass tube with a vycor frit at the base.

3.2.2 Capacitance Versus Potential Curves

Capacitance was determined by EIS and equivalent circuit modelling. Each spectrum had an AC amplitude of 10 mV (except for glove box measurements), and the cell potential was iteratively changed from -1.8 V to 0.2 V versus Ag/Ag^+ over 21 measurements.

3.2.3 Glove Box Measurements

The reference electrode was assembled after being placed in the glove box and the graphite electrode was exfoliated in the glove box as well. Water and oxygen concentrations were < 0.1 ppm. The AC amplitude was increased to 100 mV for this measurement as it was found to return the widest frequency window without errors. This is especially important for the lower frequencies, where the most information is gained about the C1 capacitance.

3.2.4 Clean Hood Measurements

An AirClean 600 Workstation clean hood was utilized to reduce the amount of adventitious hydrocarbons available to adsorb on the surface. This apparatus belongs to the lab of professor Shigeru Amemiya, where these experiments were performed. Air was filtered through a medical grade filter and a charcoal filter, and a positive pressure was established to create a clean atmosphere. No organic reagents were kept in the clean hood. The graphite was exfoliated in the hood, and the reference electrode solution was made in the hood as well.

3.2.5 In Situ EIS

Graphite was exfoliated and the cell was assembled. The reference electrode was purged with N_2 to prevent the voltage from drifting over time. The EIS tests were started and the adulterant was added (except for the untreated).

3.3 Results

3.3.1 The Effect of Environment on the PZC Capacitance

The first test is to determine if there is a significant difference between the capacitances at the potential of zero charge (PZC) in different experimental conditions. Below in figure 21 we see a comparison of 3 different conditions.

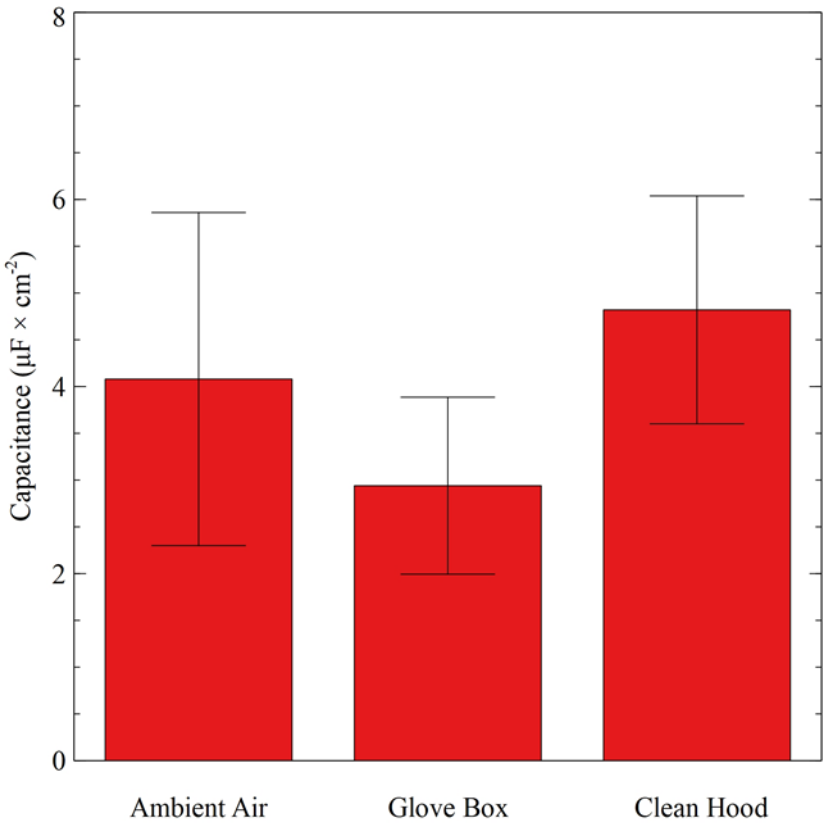

Figure 21. Capacitance measurements in ambient air, a glove box, and a clean hood. The number of replicates are 10, 7 and 7 respectively.

The variance in capacitance between separate exfoliations makes interpretation difficult, but it can be seen that there is not a significant difference between ambient air and other atmospheric conditions. The glove box and clean hood tests do have some overlap at one standard deviation, so we cannot consider their difference to be statistically significant.

Observations of intentional contamination were also made. It is known that hydrocarbon adsorption affects the capacitance on the surface of graphite in aqueous systems, so it would follow that the same could be true for ionic liquids.[85] Below in figure 22, we see the effect of additional contaminants to a BMIM PF_6/graphite system.

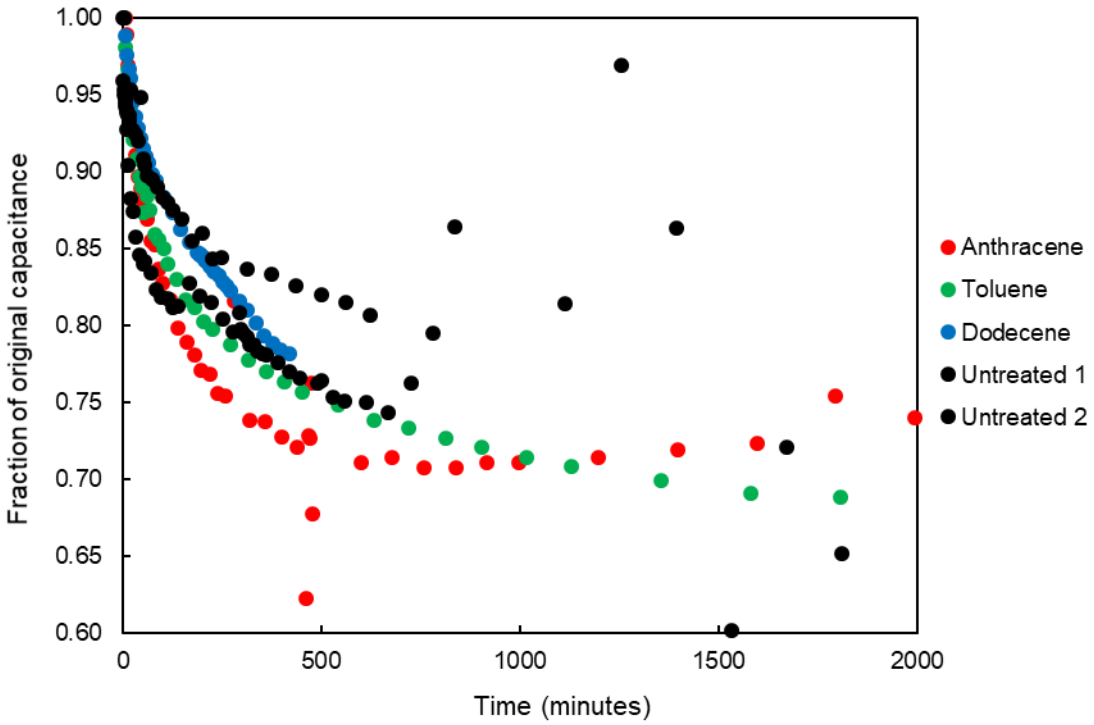

Figure 22. Solution phase aging of graphite in BMIM PF_6.

For many of the tests the capacitance measurements become unreliable after about 8 hours. An EIS measurement was considered unreliable when either impedance or the phase shift of the spectrum did not follow the behavior of known systems. Also these errors were often accompanied by other instrument error messages (*i.e.* current overload). The difference between the untreated systems and those with added organics is not substantial.

The voltage dependent behavior of the graphite/IL system was studied as well. Here we answer the question of whether or not we should expect graphite to behave as explained in Kornyshev theory or deviate as has been found in some experiments.

3.3.2 Capacitance Versus Potential Curves

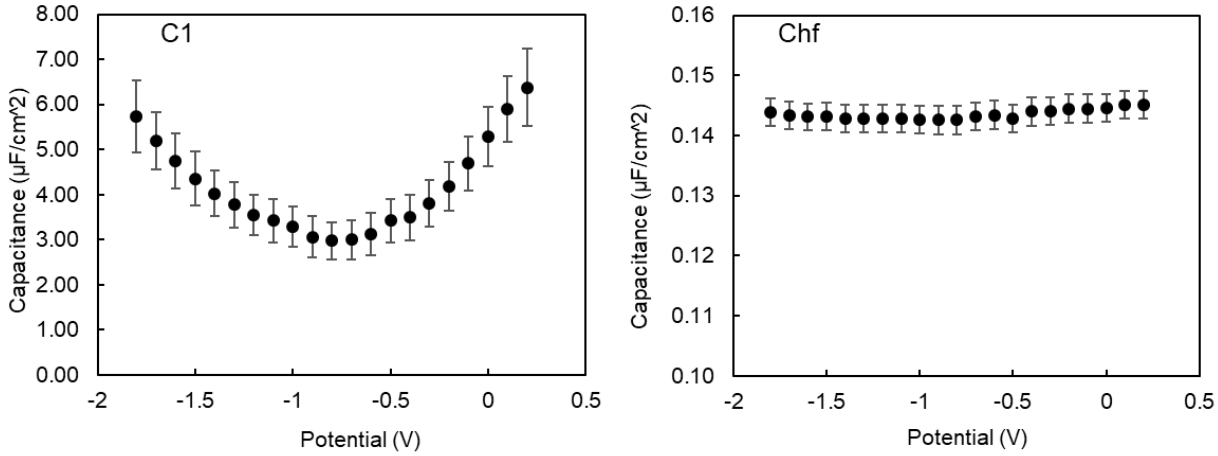

Figure 23. Capacitance vs potential measurement of the graphite BMIM PF_6 interface in a glove box. C1 and Chf are the two relevant circuit elements being discussed.

Above in figure 23, we see the capacitance vs potential curve for our system. The data is best fit by an equivalent circuit with two capacitors. Chf fits the high frequency phase shifts, and C1 the lower frequencies. The test was first done in a glove box as the hypothesis was that contaminants changed the behavior of the surface. We see here that the "u-shaped" curve predicted by theory is observed here. There is no potential dependence for the Chf circuit element. the interpretations of this data will be in the discussion.

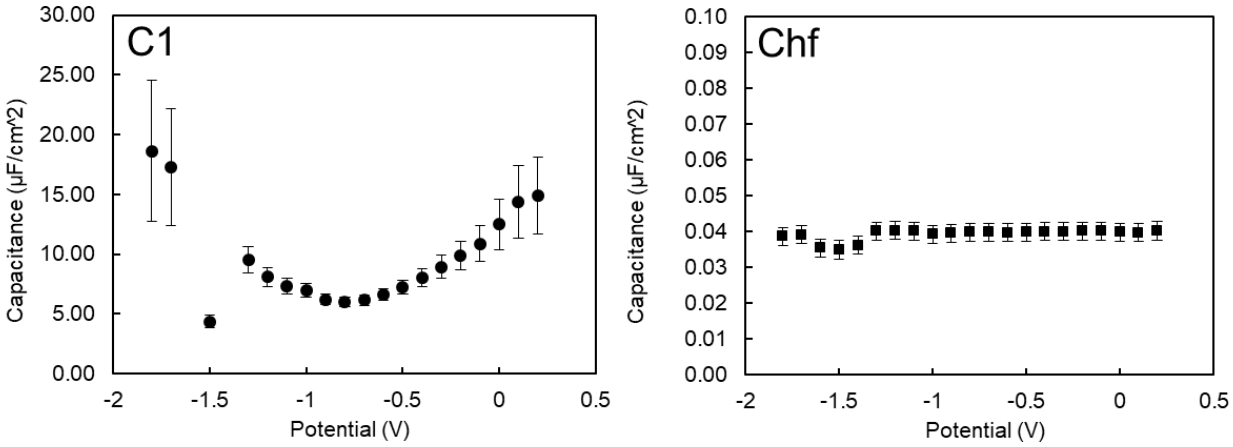

Figure 24. Capacitance versus potential measurement of the graphite BMIM PF_6 interface in a clean hood.

Figure 24 shows the same experiment in a clean hood. This hood uses a positive pressure airflow with a charcoal and medical grade filter. This is likely as close as can be attained for cleanliness from hydrocarbons in a realistic environment. Some of the data is not plotted, as the fit became suggested a physical impossibility. It is difficult to determine the cause of the unexpected behavior in the data. The EIS spectra of each point are continuous, and consistent with capacitive behavior. The data points from -1.6 V to -1.4 V are likely influenced by something not related to the interface but part of the measuring process. The shape of the curve is reminiscent of the previous data, and also follows the shape predicted by theory.

Finally, we will compare the previous data to the same experiment in an unaltered ambient atmosphere. The only difference here is that the reference electrode was purged with nitrogen to remove the potential shifts introduced by oxygen in the cell.

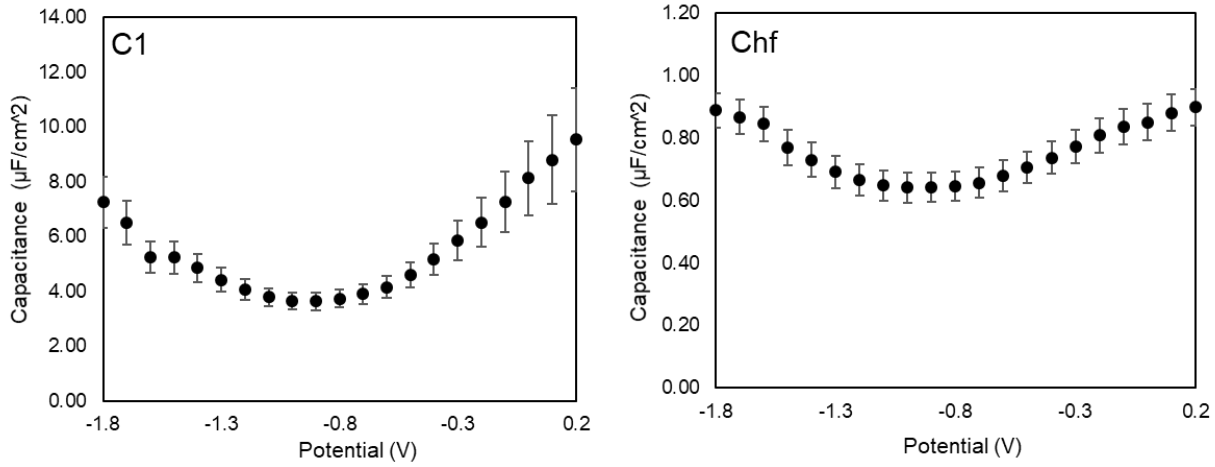

Figure 25. Ambient air capacitance versus potential curve.

Curiously, Chf for this test does seem to have potential dependence. Both C1 and Chf have the minimum shifted below -0.8V, which is likely due to a shift in the potential of the reference electrode. Also, the capacitance is asymmetric in magnitude on either side of the curve.

3.4 Discussion

The original hypothesis – that hydrocarbons affect the behavior of the graphite/IL interface – is not necessarily proven by this data. The primary reason for the lack of clarity comes from the inconsistency in the true surface area of the surface of graphite. For the ambient air measurements at the PZC, the standard deviation is so large that it is difficult to make meaningful conclusions. Another factor that contributes to this is the possibility of reference electrode drift. In order to allow for a measurement that is influenced by the environment, the reference electrode was not purged with nitrogen. The reference electrode shifts would cause the potentiostat to hold the working electrode at the incorrect potential and shift the measurement. These two elements would

need to be accounted for to reduce the error in the experiments. On the other hand, any sort of measurement of the true surface area would unavoidably influence the surface and cause doubt of the validity of the measurement. The same is true for a nitrogen purge of the system. For these reasons and that the measurements were intended to be complimentary, they are presented as is.

3.4.1 Capacitance at the PZC

The clean hood and glovebox measurements of figure 21 seem to imply that with more precise measurements, there may be a difference in their capacitance values. These two tests were designed to parse between water and hydrocarbons as possible contaminants. It has been postulated that water could influence the surface properties of graphite by forming an ice-like layer that remains even in solution.[88] Since the glovebox is an environment with trace water, it should be the minimal contributor. It may be more optimistic to think the same is true about the clean hood and hydrocarbons. A charcoal filter and a medical grade filter are used to reduce as much contamination as possible. We expect this to be a slightly lower hydrocarbon environment, and therefore have a larger capacitance. The data implies that this is possible, but difficult to defend with the large error involved.

The *in situ* capacitance measurements of the graphite - IL interface in figure 22 contains some unexpected results. The addition of organics intended as contaminants did not seem to appreciably effect the ending capacitance. The capacitance is presented as a fraction of the original capacitance for the purposes of comparison. Behavior very similar to this has been recorded for aqueous systems.[85] The possibility remains that this initial capacitance loss is intrinsic to graphite itself after exfoliation and measurement by EIS. A possible mechanism could be solvent intercalation in the outermost layer of the exposed step edges. Another idea is step edge healing,

where flakes of graphite assimilate to the surface and reduce the available surface area. It is also possible that this initial capacitance loss is adsorption related, but the contaminants chosen were not able to compound the effect. The sets of experiments performed here were not sufficient to determine the mechanism behind this behavior. Further investigation is required for more understanding on this subject.

3.4.2 Capacitance versus Potential Curves

Finally, we will discuss the potential dependence of the capacitance as seen in figures 23-25. The most striking observation is that the u-shaped behavior is seen in each of the experiments. The part of the hypothesis that adventitious adsorbates influenced the behavior of the measurement of Muller *et al.* seems to be disproven.[82] The discrepancy between theory and their data seems to be from an unknown source. In this work we verify the theoretical model proposed by Kornyshev, and the commonly held view that nonmetallic electrodes in ionic liquids exhibit u-shaped capacitance versus potential curve.[81-82]

3.5 Conclusion

The behavior of the interface between BMIM PF_6 and graphite is shown to follow with theory as established by Kornyshev.[83] A U-shaped capacitance-potential curve is observed in various environments, and there is no clear effect of environment on the shape of the curve. Several replicates were measured at the PZC and no statistical significance was seen between different environments. This data suggests that on short timescales (< 5 minutes) in air, surface adsorption

of adventitious species is not a significant factor for reduction of capacitance. There is, however, evidence that a change occurs at the surface when in solution. A capacitance drop of ~25% over 8 hours was observed. The behavior of the system was not significantly changed with the addition of anthracene, toluene, or dodecene. Several possibilities were discussed about the nature of this capacitance drop at the PZC, but further study is needed to clarify its source and effect on the system. For more discussion on the cleanliness of carbon electrodes, refer to Appendix C: "Assessing and Mitigating Surface Contamination of Carbon Electrode Materials".

3.6 Acknowledgements

This work is supported in part by ONR (N00014-18-1-2555)

4.0 Wettability of Soil Mineral Surfaces Influenced by Airborne Hydrocarbons

4.1 Introduction

Soil water repellency is a well-known phenomenon, but its causes are not completely understood. In this work we show how airborne adventitious hydrocarbons can adsorb to mineral surfaces to contribute to this effect. The water contact angle (WCA) is shown to increase from 0° to 25° for silica, and to 65° for alumina after 4 days of exposure in ambient air. The change in the amount of hydrocarbons is monitored by spectroscopic ellipsometry (SE) and X-ray photoelectron spectroscopy (XPS). Water drop penetration time (WDPT) is measured on kaolinite after treatments with either heat or ozone to show that adsorption of airborne hydrocarbons can increase the WDPT of mineral powders.

Understanding soil-water interactions is of importance to many fields of research, including climate change, erosion control and agriculture.[33, 89] Due to declining global water reserves and an expected decrease in rainfall in dry climates, increasing the efficiency of water absorption in soil is of great interest.[35, 90] Previously, it had been assumed that soils are typically hydrophilic and that repellent soils are the exception.[91] It might be expected that the water-absorptive properties of soil would be intermediate between the mineral and organic components, two major constituents of soil. As research interest increased, investigations revealed water repellency in soils to be quite prolific.[34] This counterintuitive finding has been largely attributed to organics coating the surface of hydrophilic minerals.[33, 89]

The organic component of soil is made of a large breadth of compounds sometimes referred to as humic substances, or humin. Humin is composed of many compounds that result from the

decay of plant and animal detritus.[92] These residues from dead plants and animals can include carbohydrates, proteins, lipids, and lignin. These common compounds decompose into various sized biopolymers, then to their constituent monomers.[93] The continuous decay, and contribution of new materials leads to a somewhat consistent composition of soil organic matter. Since decomposition rates affect the composition of the soil, the makeup of soil is also affected by rainfall, temperature, soil texture, and surface vegetation.[94]

There has been some difficulty determining which compounds are the cause of soil water repellency. Fatty acids and long chain aliphatic hydrocarbons have been suspected to be the organics that cause the coating of mineral grains.[95] It has been shown that fatty acids, and waxes are the likely cause of repellency in nonwetting sands.[96] Associations between water repellency and the proximity of certain plants and fungi have also been made.[97-98] Although progress has been made, the mechanism by which hydrophobic organics become bonded to soil particles remains unclear.[89]

It has been shown that the wetting properties of soil can be determined by macroscopic structures (*i.e.*, coatings on soil aggregates). [36-37, 99] Although there are macroscopic explanations for how soils can be water repellent, there is a gap in understanding where these structures are absent. The source of the mineral water repellency has been proposed as adsorption of organics such as pollutants, microbes, plant root exudates, and wildfires.[100-102] Yet, there is some disagreement as to what causes the minerals to be coated with organics, as hydrophobicity is not necessarily associated with the amount of organics in the soil.[103-104] Though the amount of organics does not affect the wettability, the molecular weight and polarity of the organics may, as Mainwaring *et al.* have shown.[105]

It has yet to be determined what mechanism causes the mineral surfaces to be coated by organics. Since as little as a monolayer coverage is enough to significantly change surface properties, many effects can potentially contribute to this phenomenon.[106] Herein we will propose a new mechanism to explain how this surface coverage could occur, and support these ideas with experimental evidence.

Our central hypothesis is that airborne hydrocarbons adsorb to mineral surfaces and contribute to the effect of soil water repellency. Airborne hydrocarbons are a natural component of ambient air; their concentrations range from parts-per-billion to parts-per-trillion, depending on the geographic location and pollution level. Airborne hydrocarbon adsorption is a known phenomenon that has been established for multiple material systems. This adsorption process occurs spontaneously over a time frame of several minutes to several days. Graphitic, metal, and oxide surfaces have all been shown to have their intrinsic wettability masked by adsorption of airborne hydrocarbons on their surfaces.[10, 107-108] However, its significance in the context of soil water repellency has not been established.

In this work, we show that adventitious hydrocarbons do adsorb to the surface of mineral particles commonly found in soil. We propose that hydrocarbon adsorption from air as a means of mass transport of organic material. We observed an increase in water drop penetration time (WDPT) in kaolinite powder upon its exposure to ambient air. We conclude that adsorption of adventitious atmospheric hydrocarbons contributes to the water repellency of soil.

4.2 Methods

4.2.1 Materials

Silicon wafers (University Wafer) used included both native oxide wafers and wafers with 300 nm of thermal oxide. Alumina crystals (Alfa Aesar) were polished on the C-plane. Natural kaolinite (Sigma-Aldrich) powder was the mineral model used.

4.2.2 Preparation of Coated Wafers

A thermal oxide silicon wafer was coated with 200 nm of Ti by electron beam physical vapor deposition (EBPVD) using a Plassys Electron Beam Evaporator MEB 550-S. The sample was then coated with the model mineral layers by atomic layer deposition (ALD) on a Ultratech/Cambridge Fiji G2 Plasma-Enhanced ALD. There are two different reactions used, one to coat with silica and the other for alumina. For silica, bis(diethylamino)silane (BDEAS) is used as the precursor, as well as a co-reactant of oxygen plasma. Twenty-seven cycles were performed at 150°C to deposit a film of ~ 2 nm. ALD of alumina was performed with trimethylaluminum and water. To obtain a film ~ 2 nm thick, twenty cycles were performed at 150 °C.

4.2.3 XPS Measurements

Measurements were taken in a Thermo Scientific ESCALAB 250Xi XPS, at a pressure of 10^{-9} torr. An Al Kα X-Ray source was used, with a take-off angle of 45° and a spot size of 400 microns. XPS scans were collected for silicon, oxygen, and carbon on the thermal oxide wafer,

and aluminum, oxygen, and carbon on the alumina crystal. A minimum of 30 scans was used for each test, and the pass energy was 50 eV. A flood gun was used to compensate for charge buildup. Samples were treated with the desired experimental conditions, then loaded into the preparation chamber. The preparation chamber was evacuated to 10^{-7} torr before loading the sample into the sample chamber, which took between 30-60 minutes depending on the sample. Each experiment required a different number of scanned elements and a different number of scans per element.

4.2.4 WCA Measurements

Measurements were taken on a VCA Optima XE video contact angle system. Samples were placed on a leveled stage, and either 0.5 or 1 µL of water was dropped on the surface. An optical image was then taken, and the instrument's software was used to calculate the contact angle.

4.2.5 Spectroscopic Ellipsometry Measurements

Thin film thickness was determined by spectroscopic ellipsometry. A J. A. Woollam Alpha-SE spectroscopic ellipsometer recorded data between the wavelengths 381 and 893 nm, at an incident angle of 70˚. The model used was a b-spline layer for the silica or alumina surface and a Cauchy layer for the hydrocarbon thin film. The Cauchy layer was set to B=1.45 and C= 0.01 to approximate the hydrocarbon layer. The first data point was used to define the b-spline layer, and the remaining points measured additional adsorption. This is a generalized model that works for any hydrocarbon adsorbing substrate.[99, 109]

4.2.6 Water Drop Penetration Time

Natural kaolinite was purchased from Sigma-Aldrich. The powder was placed in a cylindrical die that had a 1 cm internal diameter and pressed to 10,000 pounds of force. Enough kaolinite was added to result in a pellet that was ~ 1 mm thick. Each measurement is from a separately pressed pellet. The pellets were then treated with the desired experimental conditions before testing. For these samples, a video was recorded at 30 frames per second. We use the video images to measure the WDPT to within 0.033 seconds. The endpoint is determined by comparing each frame near the endpoint and assessing whether any part of the remaining drop is visible.

4.2.7 Heating

For the WDPT experiments, kaolin pellets were placed in an oven in a glass container. NaOH pellets were added to remove atmospheric water. The temperature was between 95 – 105 °C for the duration of the heating (as specified in each experiment). For the XPS experiments on powdered kaolin, the samples were heated in a glass tube furnace at 300 °C for 3 hours prior to analysis.

4.2.8 UV/Ozone Cleaning

Samples cleaned with UV/Ozone were placed in a Bioforce Nanosciences UV/Ozone Pro cleaner at intervals between 5 - 60 minutes (as specified for each experiment). The timer was started when the lamp was turned on and stopped when the lamp was turned off.

4.3 Results and Discussion

4.3.1 Measurements of Coated Wafers

For this study, we started with materials that are chemically similar to those in soil but are easier to study with surface sensitive characterization techniques. We first establish that a change in wettability of two model mineral surfaces (silica and alumina) is associated with an increase of hydrocarbons on the surface. To that end, we have performed both spectroscopic ellipsometry (SE) and water contact angle (WCA) measurements of silica and alumina surfaces, seen in figure 26. The two techniques were performed in parallel. Two pieces of coated wafer were cleaned by UV/Ozone and then immediately measured. The purpose of the UV/Ozone treatment is to oxidize and remove any pre-existing surface-adsorbed carbon species.[110]

WCA measurements show that UV/Ozone treatment allows the surface to be fully wetted (WCA = 0°) for both silica and alumina. However, upon exposure to ambient air, the WCA value started to increase. The increase begins to slow after a few days, with silica settling near 25° and alumina near 65°. This increase of WCA was previously reported for many materials and attributed to the adsorption of hydrocarbon compounds in the atmosphere. The hydrocarbon adsorption was directly measured in the SE data, which shows that a similar amount of material adsorbs to the surface of silica and alumina within seven days, leveling off near ~0.4 nm. The curve shape is similar between WCA and SE for both materials, suggesting they share the same origin. The ripple-like fluctuations in the SE data were correlated to temperature changes in the room; SE measurements are known to be sensitive to temperature.[111]

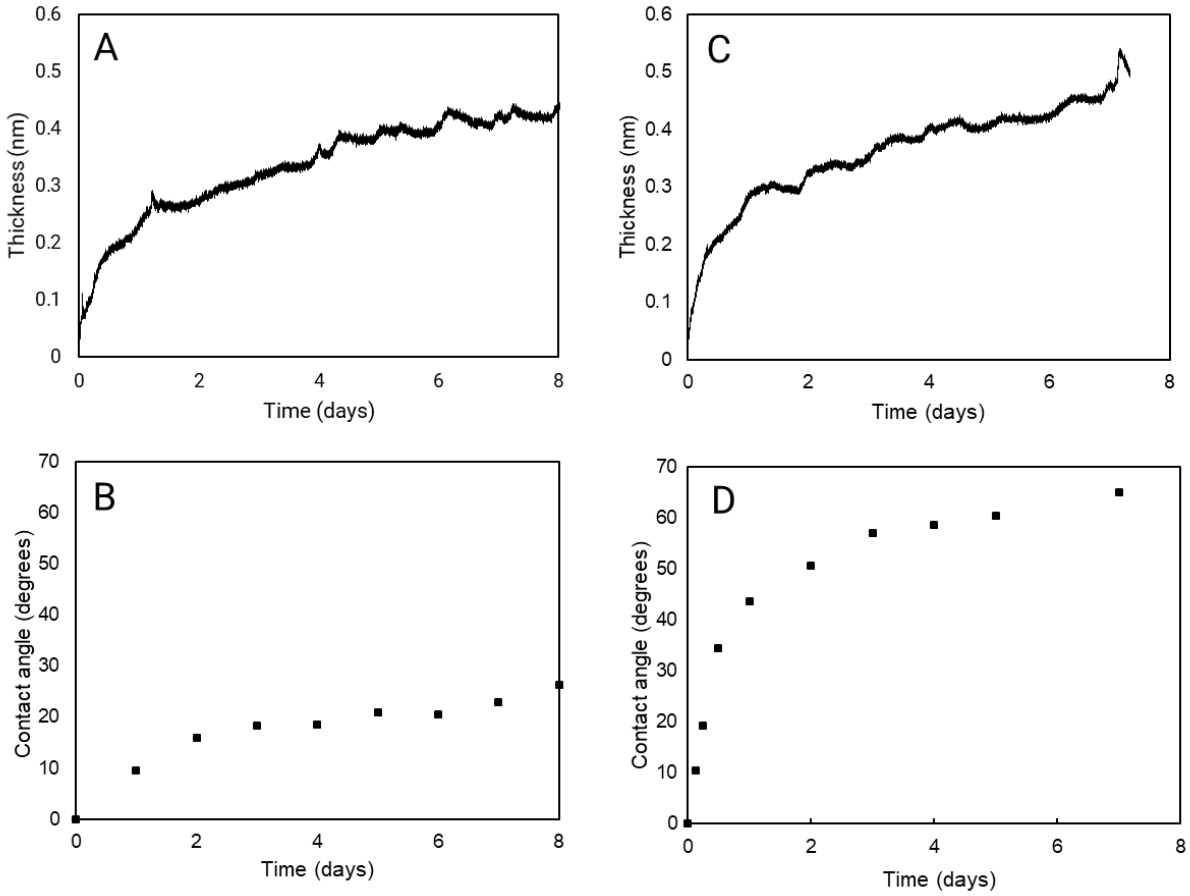

Figure 26. Effect of air aging of silica and alumina coated wafers after UV/ozone treatment. (A) SE of silica (B) WCA of silica (C) SE of alumina (D) WCA on alumina. The ripple-like fluctuations in the SE data were likely due to temperature changes in the room.

4.3.2 Measurements on Native Surfaces

There is a significant difference in the ending WCA of silica and alumina. Without the SE data, we might conclude that the amount of hydrocarbons adsorbed on alumina must be greater than that of silica. However, SE data suggests that there is very little difference in the amount of hydrocarbon adsorbed. This discrepancy could be explained by a difference in the type of adsorbed

hydrocarbons due to the difference in the substrate. The data suggests that silica preferentially adsorbs hydrocarbons that are more hydrophilic than the ones adsorbed on alumina.

Another surface sensitive technique, XPS, can identify the elemental composition of the first few nanometers of a surface. This technique was performed on a thermal oxide silica wafer, and an alumina crystal. The samples were cleaned with UV/ozone prior to analysis. In figure 27 below, we see that the percentage of carbon on the surface increases over the course of the experiment. After seven days, the percentage of surface carbon was about 14% on silica and 10% on alumina. Note that XPS is acquired in ultra-high vacuum, which could induce desorption of surface-adsorbed species.

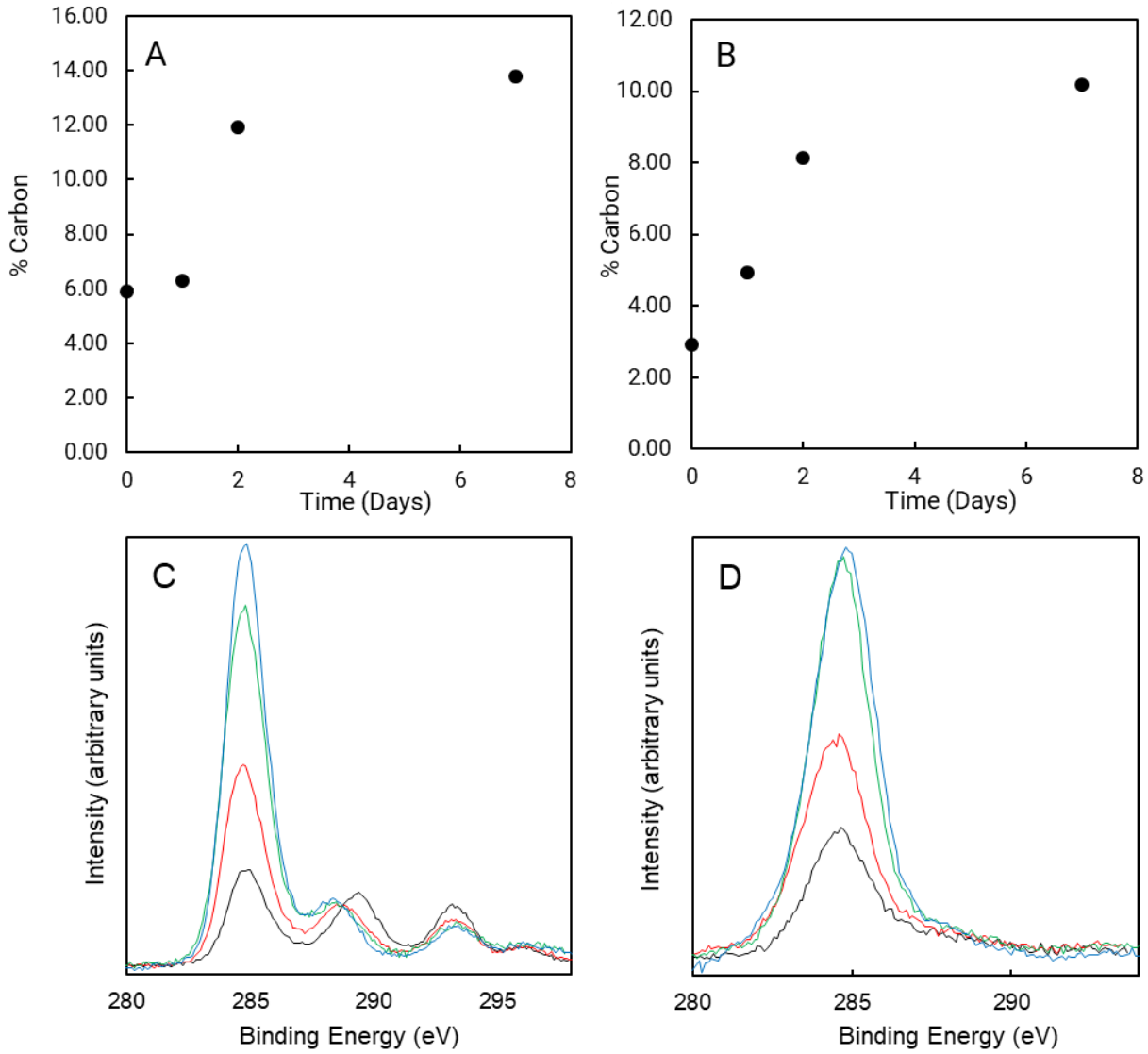

Figure 27. Surface carbon contents measured by XPS from a (A) 300 nm oxide silica wafer and an (B) alumina crystal. Elements scanned for were oxygen, carbon and (A) silicon or (B) aluminum. The carbon spectra for (C) silica and (D) alumina are also shown. The spectra shown are 0 days (black), 1 day (red), 2 days (green), and 7 days (blue). Carbon binding energies are corrected with reference to the known binding energy of either silicon or aluminum.[112-113]

Figures 27C and 27D show the XPS carbon peaks. Figure 27D shows that alumina adsorbs only one type of carbon species, which are most likely unsubstituted hydrocarbons. The carbon

spectra of the silica sample (figure 27C) is much more complex. The four peaks are likely differently substituted carbons on the surface. Higher binding energies correspond to carbons bonded to more electronegative heteroatoms.[114] With air aging, all of the 3 higher binding energy peaks decrease in intensity relative to the main peak at 285 eV, with the peak at 296 eV reducing to zero after 2 days. It is possible that the peak at 293 eV is an unexpected potassium contaminant but is more likely to correspond to a fluorinated carbon, as fluorine is seen in the survey scan. The peak at 288 eV corresponds to carboxylic carbons, which are likely oxidized species that remained after ozone cleaning. A comprehensive list of spectra and integrations can be found in the supporting information. It should be noted that the hydrocarbons with electronegative heteroatoms seen here are not expected on the silica surface initially, and are possibly a consequence of the ozone treatment.[115]

From the techniques above, we conclude that there is a growth of carbon-containing species on silica and alumina after cleaning with UV/ozone. The data is consistent with UV/ozone removal of carbon species followed by re-adsorption of airborne hydrocarbons upon air exposure. Measurements on flat surfaces are helpful for understanding adsorption phenomena, as they are suitable for many surface sensitive analytical techniques. These data provide a reference point for us to understand the adsorption of airborne hydrocarbons on powder samples and their impact on wetting, which are likely more complex than the flat ones.

To quantify the effect of airborne hydrocarbon contamination on the wettability of soil, we have used kaolinite powder as a model substrate to measure water drop penetration time (WDPT). Kaolinite is an aluminum silicate mineral with a chemical composition of $Al_2Si_2O_5(OH)_4$ and is commonly found in soils. Using kaolinite should allow us to investigate soil minerals that are

chemically and morphologically more consistent with real soil minerals. We chose WDPT to quantify soil hydrophobicity as it is commonly used, and has much literature precedent.[61]

4.3.3 Measurements of Kaolinite

In one experiment, we simulated the effect of high temperature, low humidity environment on the wettability of soil. We heated kaolinite pellets in an oven for extended periods of time. The high temperature will remove surface-adsorbed water from kaolinite. We previously showed that desorption of water accelerates adsorption of hydrocarbons in the case of graphitic carbons.[116] Here we expect a similar effect; the heat treatment will promote airborne hydrocarbon adsorption on kaolinite and increase its hydrophobicity. The WDPT data is shown in figure 28A. The first data point, zero day, is tested before heating; upon heating, we see a significant increase in the WDPT, which indicates that the kaolinite pellet indeed becomes more water repellent. The WDPT remained at about 20 seconds after 24 hours or longer of being heated in an oven.

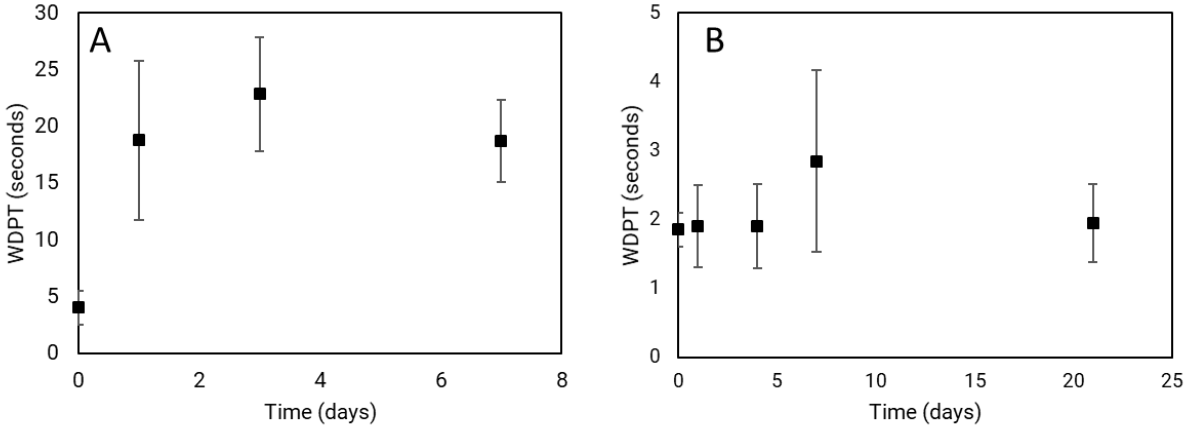

Figure 28. WDPT of kaolinite pellets. Treatment conditions are (A) untreated at 0 day, then in an oven at 95 °C for the time indicated, and (B) treated with UV/ozone for one hour, then measured after the designated amount of time. Note that the vertical scales are different in (A) and (B).

In another experiment, we measured the WDPT of kaolinite pellet after it is cleaned by UV/ozone, followed by storage in air at room temperature. The data is shown in Figure 28B, with the first data point being measured after the pellet was treated with UV/ozone for one hour. We observed that UV/ozone slightly reduced the WDPT: ~ 2 seconds compared to the ~ 4 seconds for the zero day data point in figure 28A. In contrast to the data figure 28A, the WDPT remained within *ca.* 2 - 3 seconds for up to 3 weeks.

Treating kaolin pellets with ozone is therefore shown to reduce the WDPT and heating increases the WDPT. The difference between untreated and treated samples are statistically different to 95% confidence. A summary of the WDPT results can be seen in figure 29. UV/Ozone resulted in a reduced WDPT, and heat treatment resulted in an increase. When heated samples were treated with ozone, the WDPT was again reduced. To understand these effects, we also conducted XPS measurements on powdered kaolin samples treated under similar conditions; these data are also shown in figure 29.

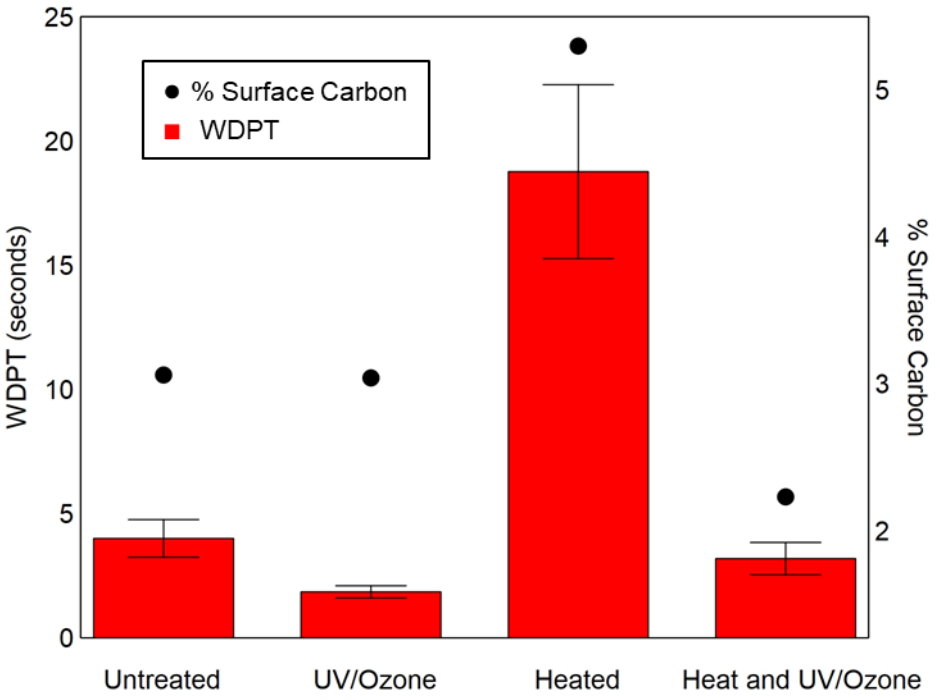

Figure 29. Correlation between surface carbon content and WDPT of kaolin under different experimental conditions. WDPT data and XPS data (% surface carbon) are shown as bars and dots, respectively. Note that the WDPT and XPS measurements are not identical conditions but are similar and shown together for illustrative purposes. Detailed experimental conditions are explained in Appendix B.2.

We found that the carbon content on the untreated kaolin sample was much lower than those measured on the flat silica (figure 27); the UV/ozone treatment did not significantly reduce the surface carbon content. However, heating did increase the amount of carbon on the surface as we proposed; this effect can be explained by the competition between the adsorption of water and airborne hydrocarbons, which we reported for the case of graphitic carbons.[116] Finally, for the sample that was heated then treated with UV/ozone, we observed a significant reduction in the surface carbon content by XPS, as expected. Overall, this data confirms that the change of WDPT

time is highly correlated with the amount of hydrocarbons on the kaolin surface, with higher amount of hydrocarbons results in longer WDPT.

4.4 Conclusion

Our data shows that adventitious hydrocarbons affect the surface wetting properties of silica, alumina, and kaolin. We controlled the amount water or hydrocarbons on the surface by treating the surfaces with heating or ozone treatment, respectively. This resulted in a change in the WCA for the silica and alumina, and a change in WDPT for the kaolin pellets. We also provide SE and XPS data to verify that carbon-containing species adsorb onto these surfaces over time. Previous studies have identified a number of contributing factors to soil water repellency, such as macroscopic structure (*i.e.* particle size, coatings on aggregates), and the type of organics in the soil.[91, 117] Our data shows that adventitious hydrocarbon adsorption is a means of mass transport of organic coatings on mineral particles and should be taken as an additional contributing factor to soil water repellency.

4.5 Acknowledgements

This work is supported in part by ONR (N00014-18-1-2555)

5.0 Conclusion

5.1 Summary

The role of adventitious hydrocarbon adsorption is emphasized as a contributing factor for several surface related phenomena. Although adventitious hydrocarbon adsorption has been documented since the early days of vacuum science, it has reemerged in the literature as more sensitive techniques allow for its characterization on more surfaces. This has allowed for the unmasking of the intrinsic surface properties of many surfaces. In this document, the importance of including hydrocarbon adsorption as a consideration is shown with multiple techniques on kaolinite and graphite.

The importance of graphite as an electrode material for batteries and capacitors and its recent unveiling of intrinsic surface properties has necessitated an investigation of its electrical properties. This work has shown that exposing a freshly exfoliated HOPG surface to ambient air and 1-octadecene vapor (*ca.* 1 ppm) caused a *ca.* 30% and 70% decrease in its double layer capacitance, respectively. Similarly, a 38% decrease of capacitance was observed within 1500 min after freshly cleaved HOPG was immersed in 1 M NaCl solution. Investigation by SE showed a growth of 0.6 – 2 nm on the surface of graphite in solution.

Graphite was also measured in an organic electrolyte, BMIM PF_6. It was found that previous literature on the shape of the capacitance vs. potential curve was flawed, and that the u-shaped curved predicted by Kornyshev theory is valid for this system. Liquid phase aging shows the reduction in capacitance can be as much as 25% in 8 hours. There is little difference between intentionally contaminated electrolyte and pure electrolyte, implying that the effect is primarily

from adventitious adsorbates, or is intrinsic to the interface. Although there was an effect of atmosphere on the interface, it could not be determined to be separate from controls due to the uncertainty in the measurement.

Soil water repellency is another surface sensitive matter that was investigated. First, a model system of a silica coated wafer, and an alumina coated wafer was tested for changes in water contact angle, and thickness of adsorbed material after cleaning. The water contact angle increased from 0° to 25° for silica, and to 65° for alumina after 4 days of exposure in ambient air. SE showed an adsorbed layer of about 0.5 nm for both. XPS showed an increase in carbon on the native surface; from 6% to 14% carbon on native oxide silica, and from 3% to 10% on an alumina crystal. WDPT measurements on kaolinite pellets showed an increase for heated samples, and a decrease for cleaned samples compared to a control. XPS measurements of similar conditions showed an increase in carbon for heating, but no decrease in surface carbon upon cleaning. When heated and cleaned the surface carbon was lower than that of the control (with a corresponding lower WDPT), showing that the % carbon and WDPT are related.

5.2 Future Directions

As new techniques emerge and new types of surfaces are discovered, there will be a continued need for analysis of surface characteristics. As these specialized materials are developed, the interplay of adventitious adsorbents with the system will be important for an accurate understanding of their function. Hydrophobic and dust resistant surfaces may be able to benefit from hydrocarbon adsorption. It could then be possible that some surfaces designed to be hydrophobic could be intrinsically misunderstood, yet still functional. Atomically thin 2D

materials should be greatly influenced by surface adsorption. With every new application conceived for graphene, boron nitride, or phosphorene there should be a commensurate consideration of adsorption phenomena. The same properties that make these materials useful, also make them susceptible to hydrocarbon adsorption. Finally, it should also be considered that even well studied materials can be influenced by hydrocarbon adsorption. As shown in this work with graphite and soil, even substrates with decades of research history can be studied for a different reason and be in need of an updated understanding.

Appendix A Supplementary Information for Adventitious Hydrocarbons and the Graphite-water Interface

Figure 30. Electrochemical cell used for EIS measurements.

Appendix A.1 EIS Equivalent Circuit Modelling

The method chosen for determining the double layer capacitance of HOPG was equivalent circuit modelling of electrochemical impedance spectroscopy (EIS) data. EIS is a useful tool for understanding the electronic properties of a system. EIS measures both the resistive and capacitive impedances when an AC signal is applied to a system. The impedance can then be fit to a model equivalent circuit. There are two models that can appropriately describe the system in question. For this study, a circuit with a constant phase element will be used to establish a fit to the data.

The constant phase element (CPE) replaces the capacitor in Randle's cell (figure 31). An electrochemical cell that is at a sufficiently low potential that no redox occurs can be displayed by the circuit in figure 31. Rs is the solution resistance, Rct is the charge transfer resistance, and Cdl is the capacitance of the electrical double layer.

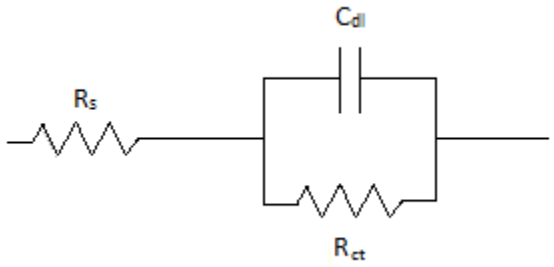

Figure 31. Randle's cell equivalent circuit.

The impedance of the constant phase element is given by equation 1. The similarities between the impedance of a CPE and a capacitor should be noted.

$$Z=\frac{1}{Y_0(j\omega)^n} \quad [1]$$

Although the CPE yields a fitting with low error, it lacks physical meaning. Correct interpretations of the parameters Y_0 and n are essential for proper understanding of a system. Y_0, must be converted to capacitance through equation 2.

$$C=Y_0(\omega''_{max})^{n-1} \quad [2]$$

ω''_{max} is the frequency at which the imaginary (capacitive) impedance is at a maximum. For derivation and use of this equation refer to the note by Hsu and Mansfield.

Appendix A.2 Analysis of EIS Data

It is difficult to control for the variation in true surface area of graphite when testing for surface sensitive properties. Measuring the basal plane capacitance is in fact one of the best methods of testing for the true surface area.[118] We cannot use this method to control for surface area and to probe for surface cleanness simultaneously. Other calculation based methods that rely on double layer theory are complicated by the nature of the double layer structure on graphite, which is largely determined by a space charge within the graphite itself.[32] Other adsorption based models could potentially be helpful, but only on a surface at a steady state, which our data shows to be difficult to attain on graphite.

We shall then determine the variability in surface area by taking the average of clean capacitance measurements (separate exfoliations) to compare to the aged samples. The largest contribution to the difference between the capacitance values of the clean samples should be from the change in surface area. We can then calculate the standard deviation due to surface area variability, and determine if the reason for the capacitance change with aging could be explained only with surface area changes. Applying the error to the 24 hours aged samples (from figure 15A) and comparing to our clean samples, the two data sets will not overlap with a 90% confidence interval.

Table 1. A collection of clean HOPG capacitance measurements and the average of the two 24-hour aged samples.

Clean Measurements ($\mu F/cm^2$)	
4.769231	Clean samples:
4.658907	$4.3 \pm 0.7\ \mu F/cm^2$
4.511134	
3.483806	24 hours aged samples:
4.311741	$1.8 \pm 0.6\ \mu F/cm^2$
5.134615	
3.064777	
4.754049	

Appendix A.3 Spectroscopic Ellipsometry Modelling

Spectroscopic ellipsometry (SE) is a technique that measures the change in polarization and intensity of light as it is reflected off a material. The measured values are Δ, the phase difference and Ψ, the amplitude component. These two values can be decomposed into r_s and r_p which are the respective perpendicular and parallel amplitudes of reflected light from Fresnel's equations. The values of r_s and r_p can be modelled to determine the physical and optical properties of the material.

B-spline parameterization of the dielectric function serves well to model a supporting layer for which no phenomenological model is required.[57, 119] As for our purposes, the dielectric properties of graphite can be experimentally determined, then applied to a subsequent experiment.

For in situ studies of contamination growth, the first measurement is taken as the "clean" measurement for determining the properties of the graphite.

In order to model the contamination layer, a Cauchy model is used. The Cauchy dispersion equation, equation 3, is applicable to transparent thin films. A and B are material specific constants. We use a value of 1.45 for A, and 0.01 for B. These values have been successfully applied to hydrocarbon thin films in literature, with a refractive index of 1.45 being appropriate for long chain hydrocarbons.[120-121]

$$n(\lambda) = A + \frac{B}{\lambda^2} \quad [3]$$

Appendix A.4 Ellipsometry Error

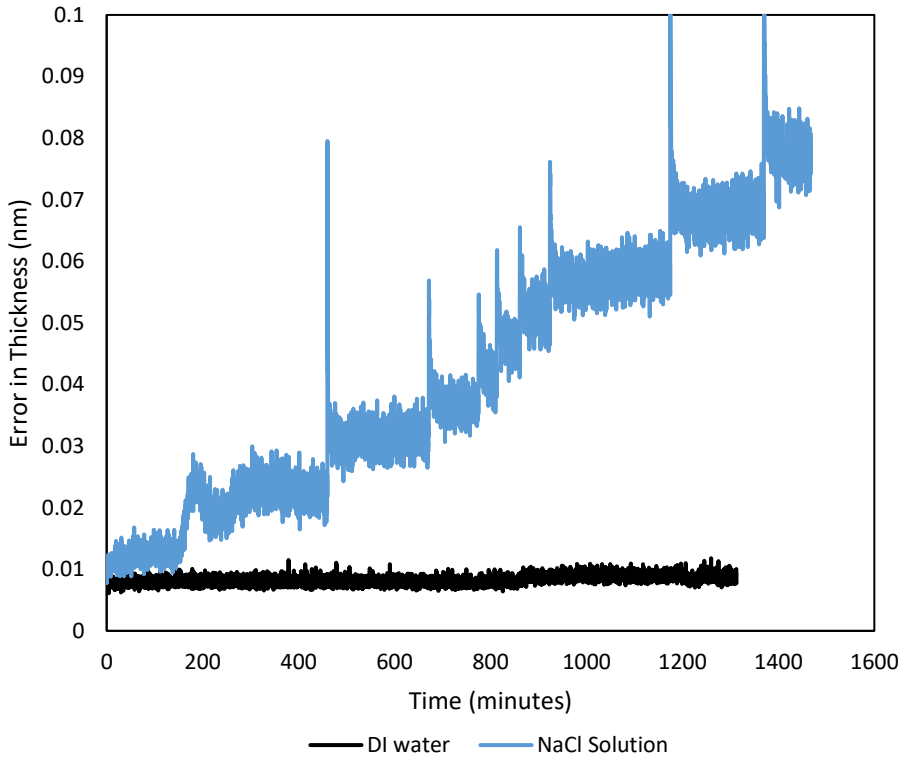

Figure 32. Error in the ellipsometry measurement over time. The data is related to figure 16 in the text.

As stated in the text, there is an increase in error over time in the waterborne aging experiment in NaCl solution. SE measurements are good at determining the change in either thickness or dielectric properties separately, but if both change simultaneously only the fitted value will be affected. This allows for the possibility of an apparent thickness change that is truly a change in the dielectric function of the surface. One source of such a change could be dynamic exchange of the thin film with the ambient solution. It is possible that molecules containing different functional groups will adsorb with different rates and with different stability. Conversely,

a change in the substrate could be the source. Specific adsorption of chloride, or surface functionalization would affect the measurement.

The DI water measurement saw no increase in error. It is then likely that the model chosen describes the system well throughout the course of the experiment. The value of the error and the lack of change is representative of all the DI water measurements seen in figure 16.

Appendix A.5 Additional ATR-FTIR Data

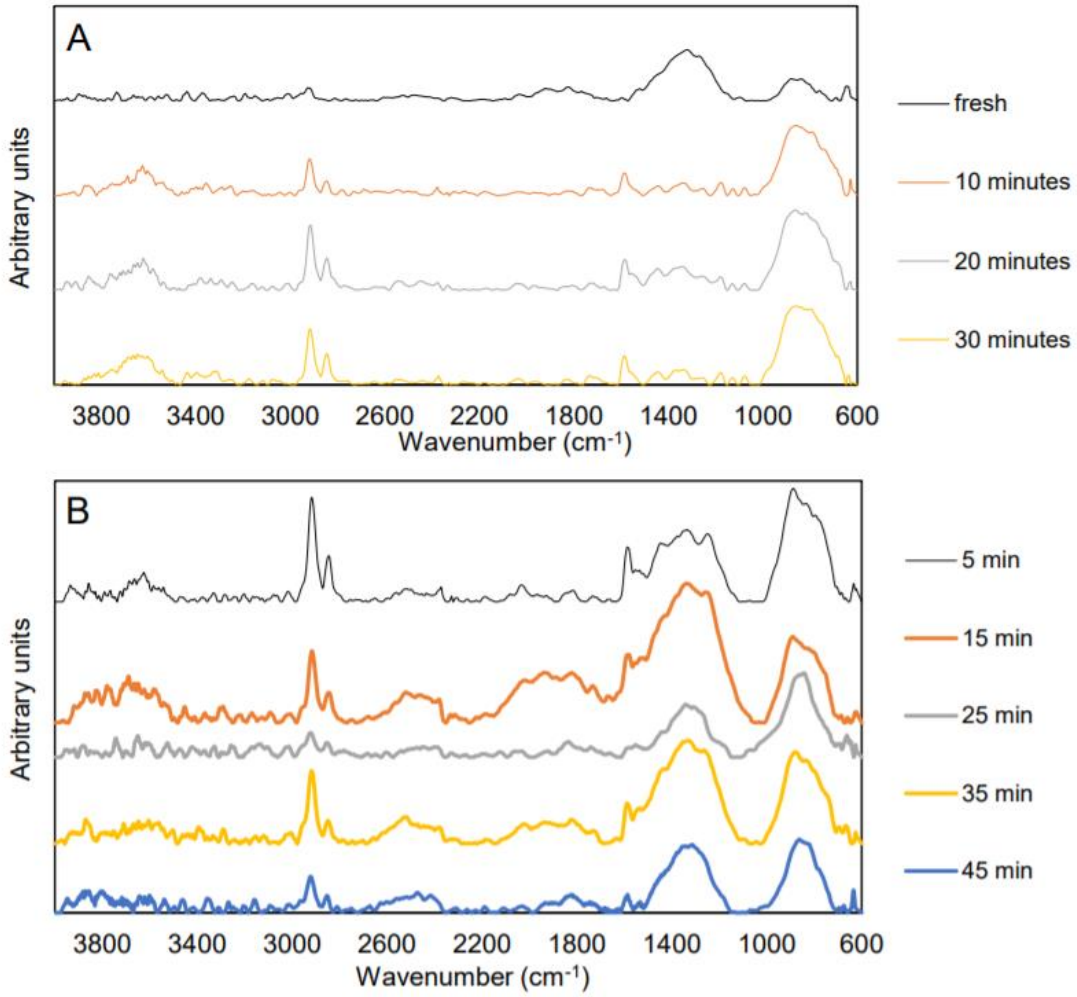

Figure 33. A separate set of ATR-FTIR data of graphite aged in (A) air and (B) 1-octadecene. The data were recorded following the same experimental parameters as in the manuscript except using 128 scans instead. Note the absence of peaks in 3100 cm^{-1} in (A).

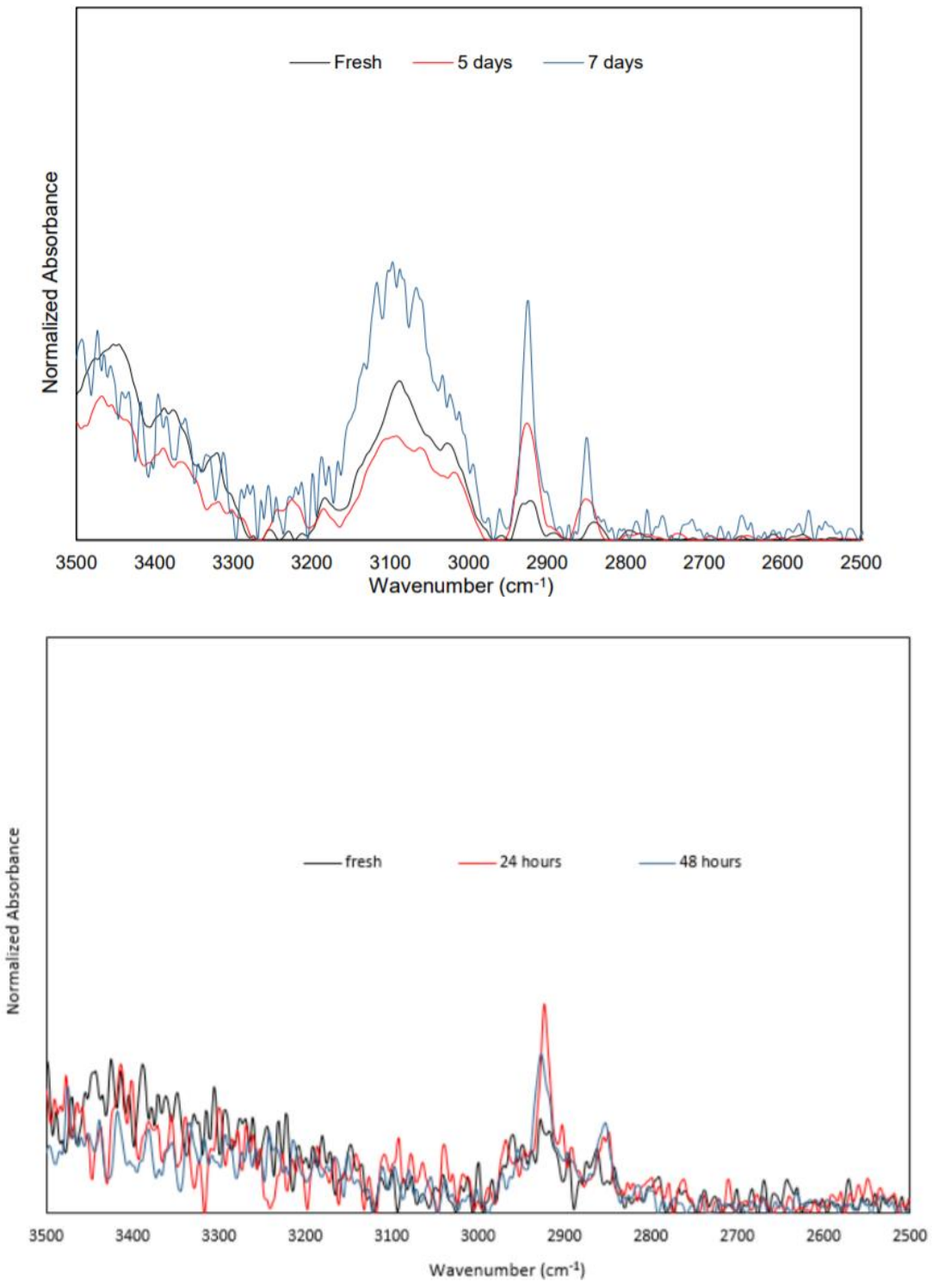

Figure 34. Overlaid FTIR spectra of aged and fresh HOPG. The spectra were selected from Figure 15C (top) and 15D (bottom). The spectra have been overlaid to emphasize the difference of the -CH2- stretch peaks between the fresh and well-aged samples.

Appendix A.6 Waterborne Contamination of Air-aged HOPG

The behavior of HOPG when aged, then placed in an aqueous environment is relevant to determine if the contaminants continue to influence the system for the long term. It is also relevant to determine if the contamination layer changes when placed in solution. We see the results in figure 3.

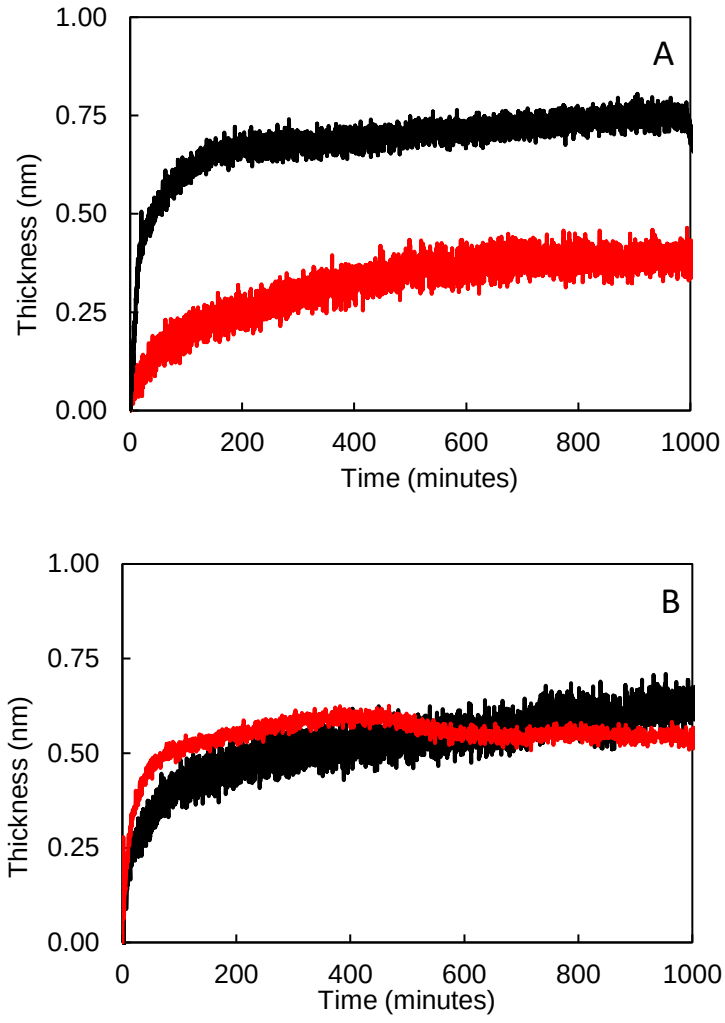

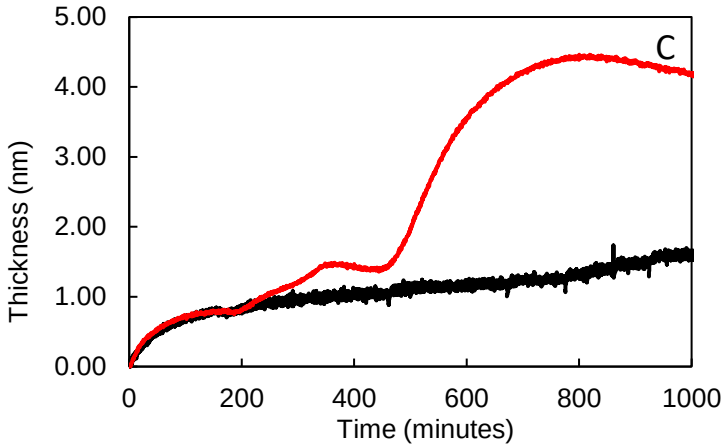

Figure 35. Comparison of fresh graphite in aqueous solutions with graphite aged for 24 hours before testing. Black: freshly exfoliated, Red: Aged 24 hours. The aqueous solutions were deionized water in panel A, 1 M NaCl solution in panel B, and saturated stearic acid solution in Panel C.

Perhaps the most intuitive behavior is seen in panel A, where the contamination growth is smaller for the aged sample than for the freshly exfoliated. The final value for the thickness is also lower. There seems to be little difference between the two experiments in panel B. It is possible that the stearic acid is more strongly adsorbed to the surface than the airborne contaminants, and any exchange that may occur is rapid. Interpretation of the data in panel C is more difficult. The growth of the contamination layer seen is also marked by a significant increase in the error. It is difficult to determine whether the changes in thickness correspond to a true physical change or if they are an artifact.

Appendix B Supplementary Information for Wettability of Soil Mineral Surfaces Influenced by Airborne Hydrocarbons

Appendix B.1 Survey Scans and All Detailed Spectra of Figure 25

Below in figures 34 - 37 are the spectra corresponding to ozone cleaned alumina XPS measurements. The data corresponds to figure 25B in the main text. Survey scans were taken immediately after cleaning and after one week. Tables of the elemental percentages are also included. The question mark labels on the survey scans signify that the software had a low confidence in the peak origin.

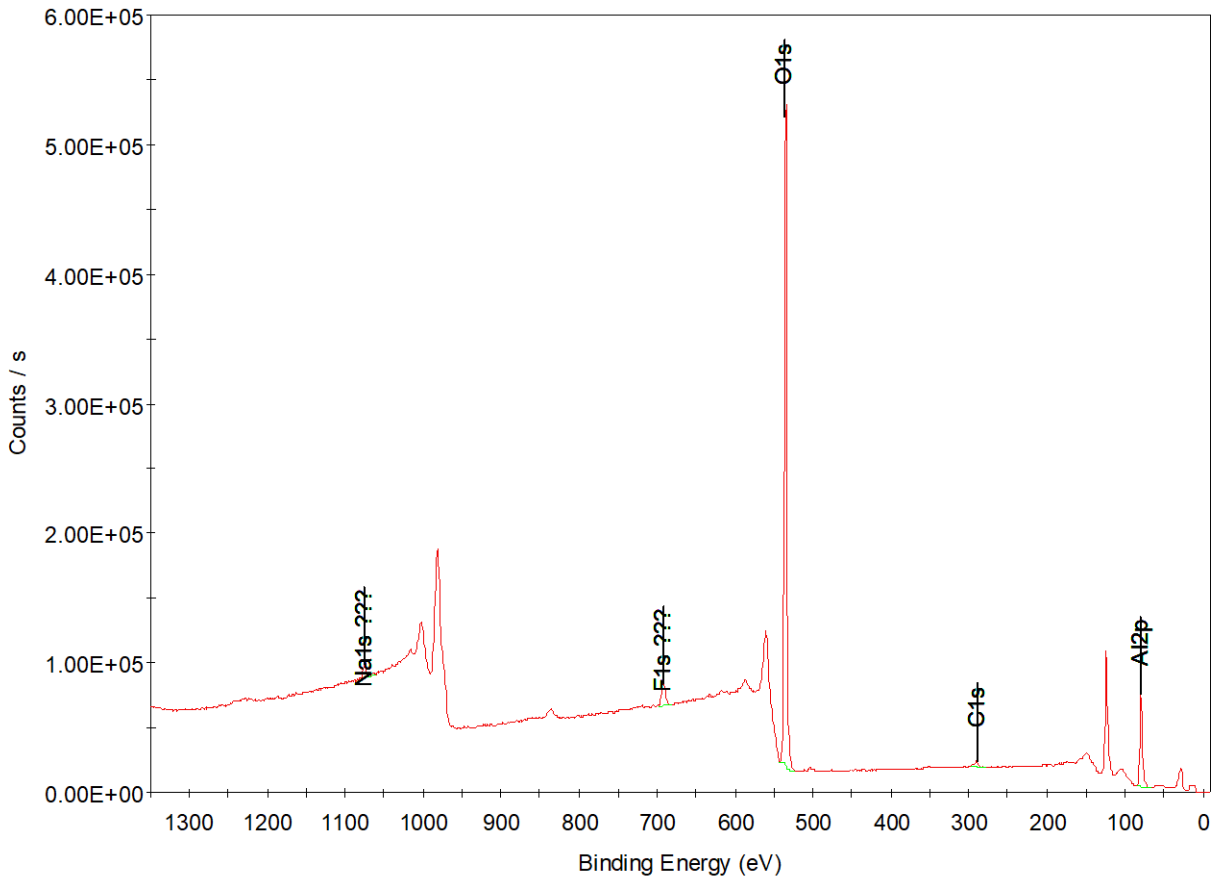

Figure 36. Survey scan of the ozone cleaned alumina surface.

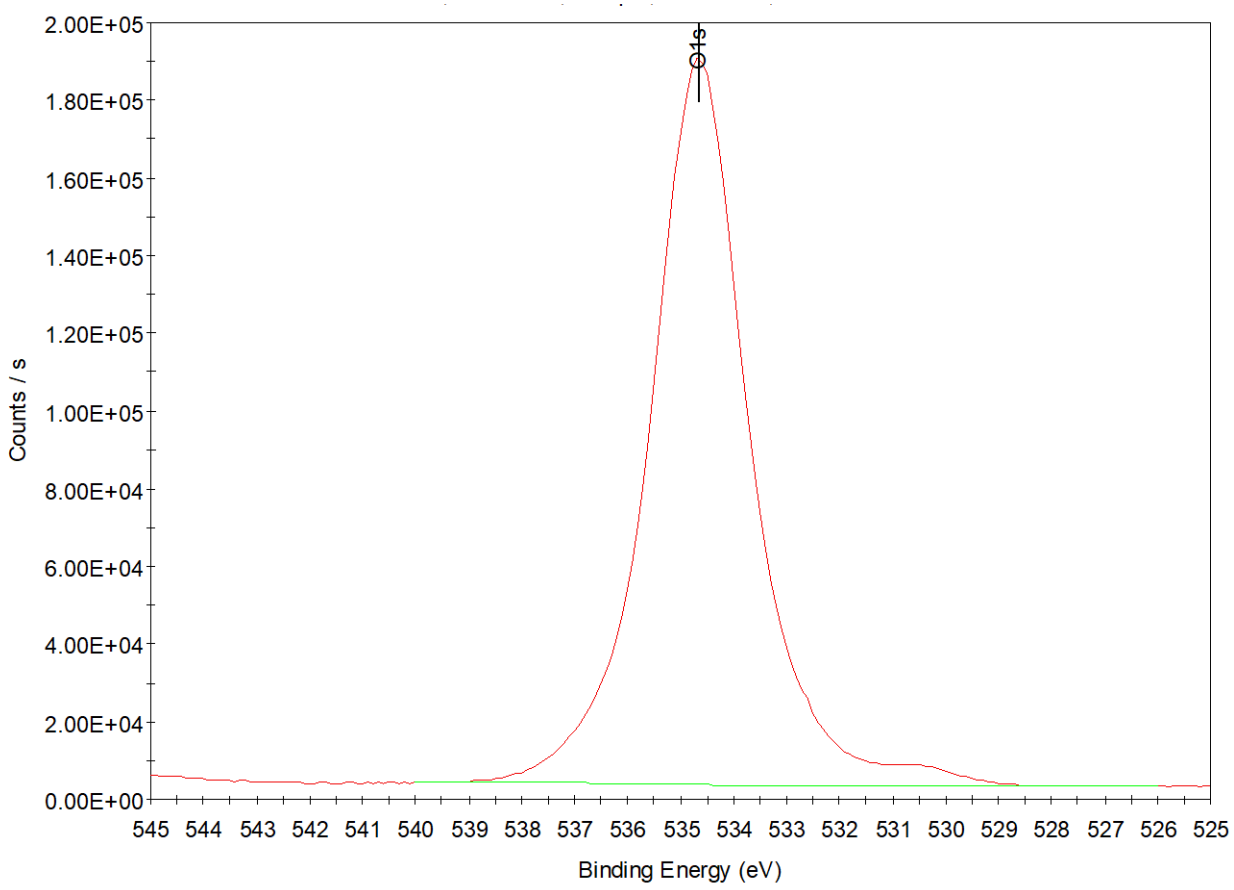

Figure 37. Elemental scan of oxygen (1s) on the ozone cleaned alumina surface.

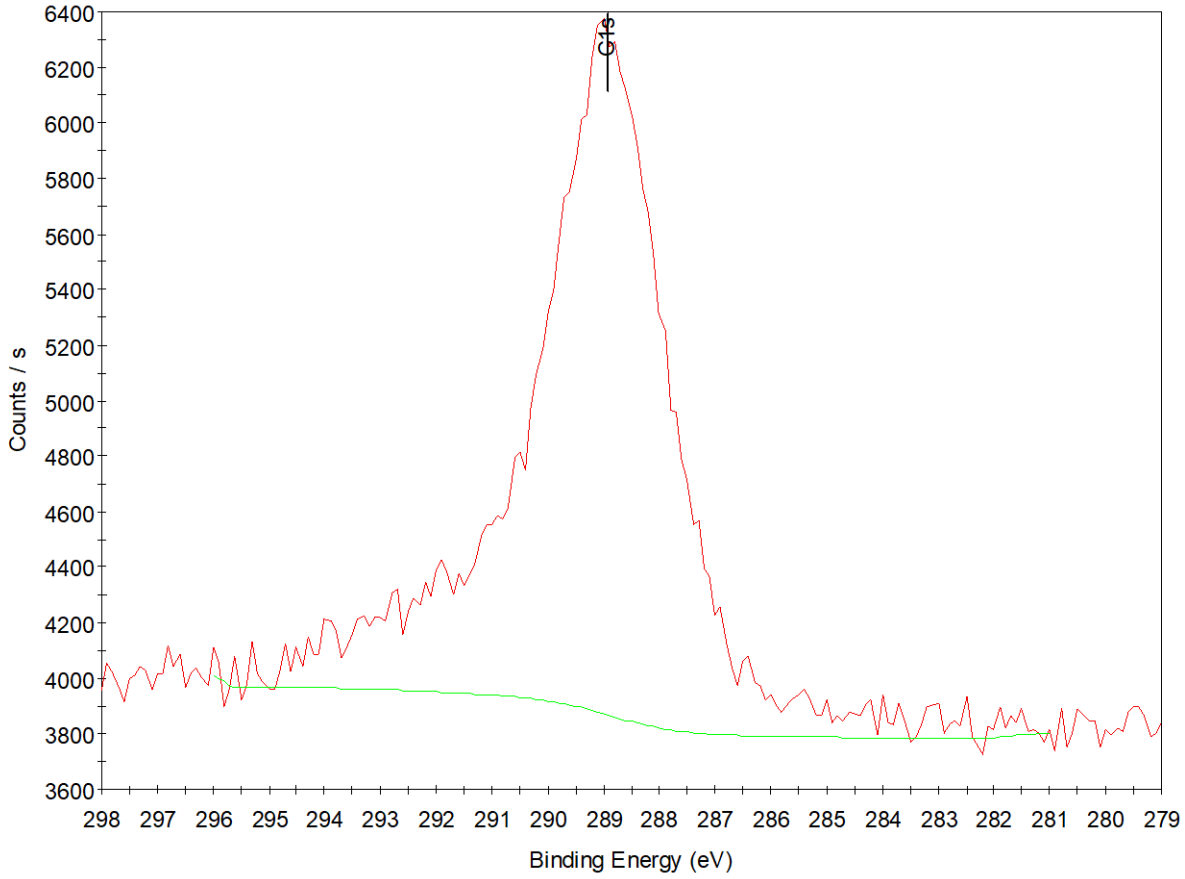

Figure 38. Elemental scan of carbon (1s) on the ozone cleaned alumina surface.

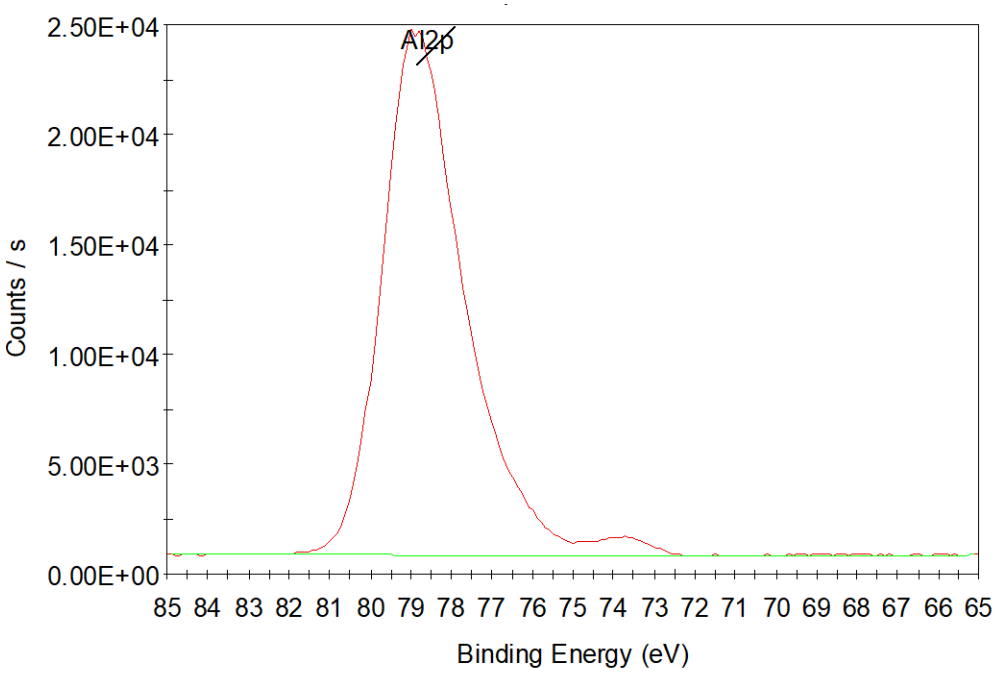

Figure 39. Elemental scan of aluminum (2p) on the ozone cleaned alumina surface.

The figures above show the detailed spectra of the XPS data gathered on ozone cleaned alumina. Below, in figures 40-42, we see the XPS peaks of 24 hours aged alumina.

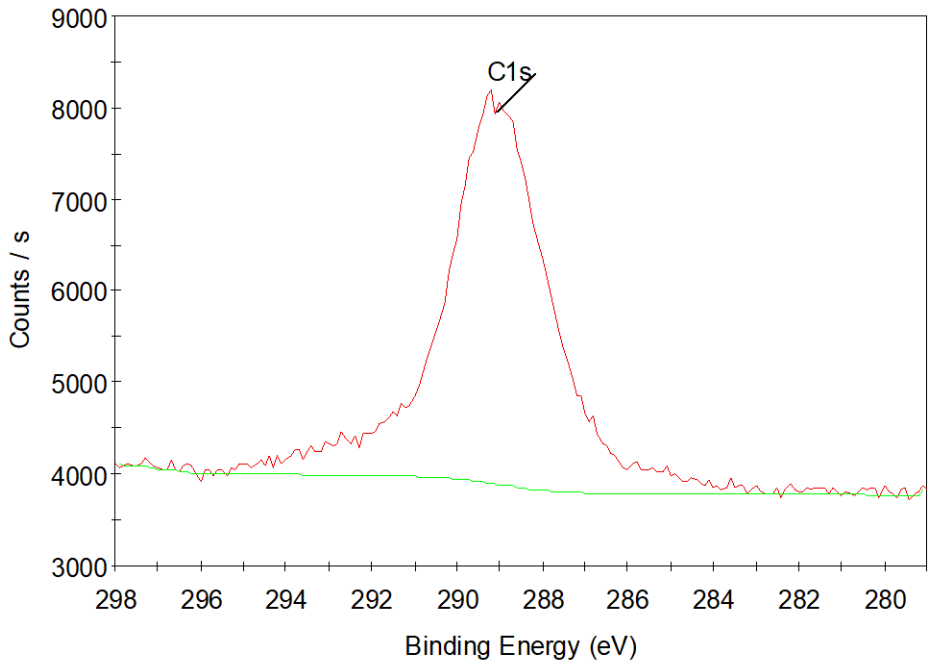

Figure 40. Elemental scan of carbon on a 24 hours aged alumina surface.

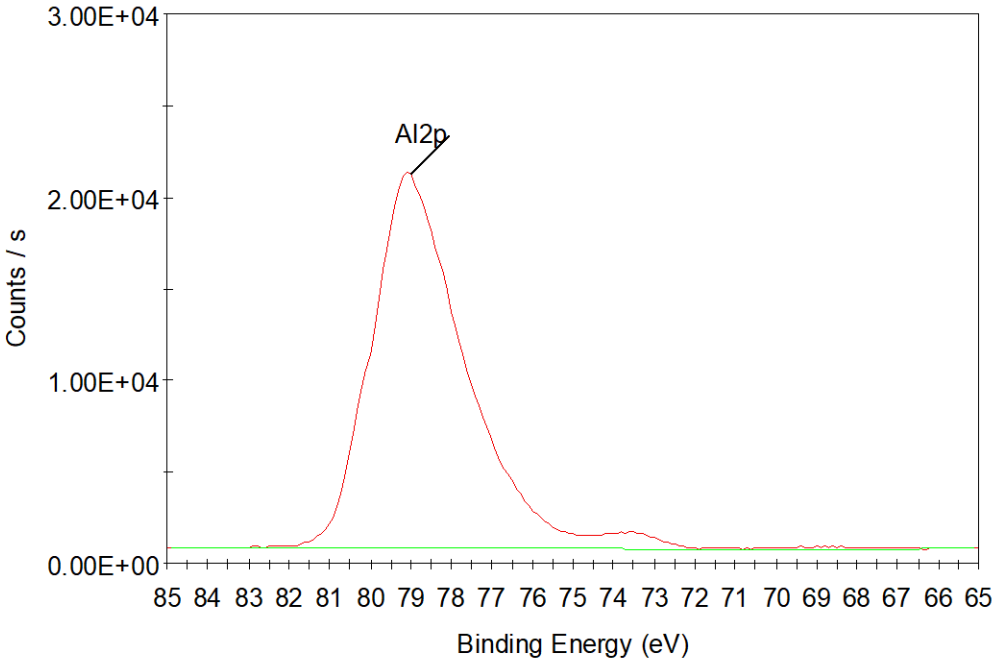

Figure 41. Elemental scan of aluminum on a 24 hours aged alumina surface.

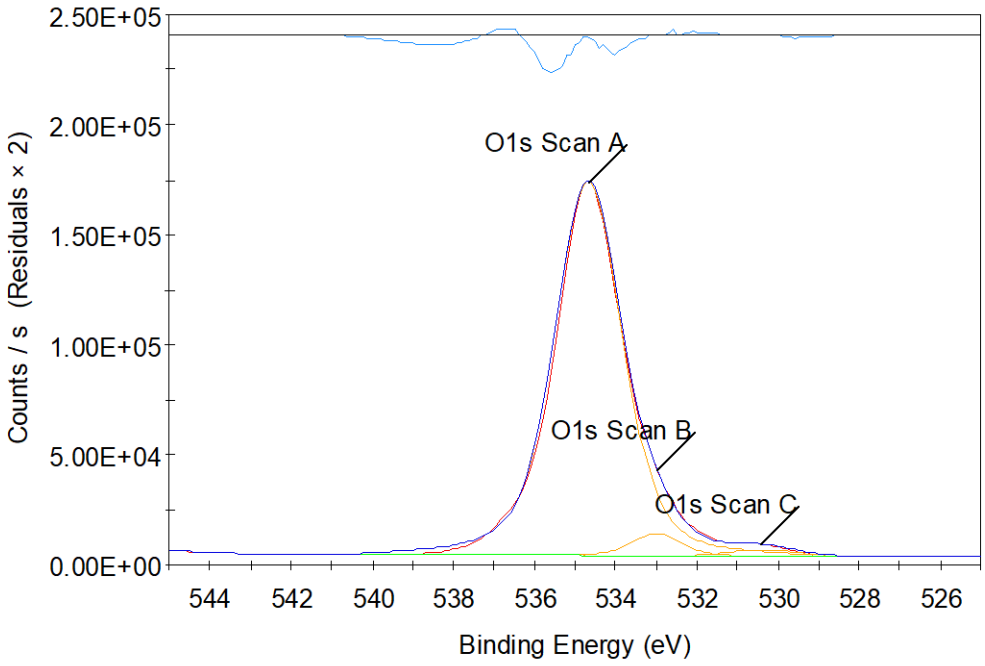

Figure 42. Elemental scan of oxygen on a 24 hours aged alumina surface.

Figures 43-45 below are measurements 48 hours after cleaning.

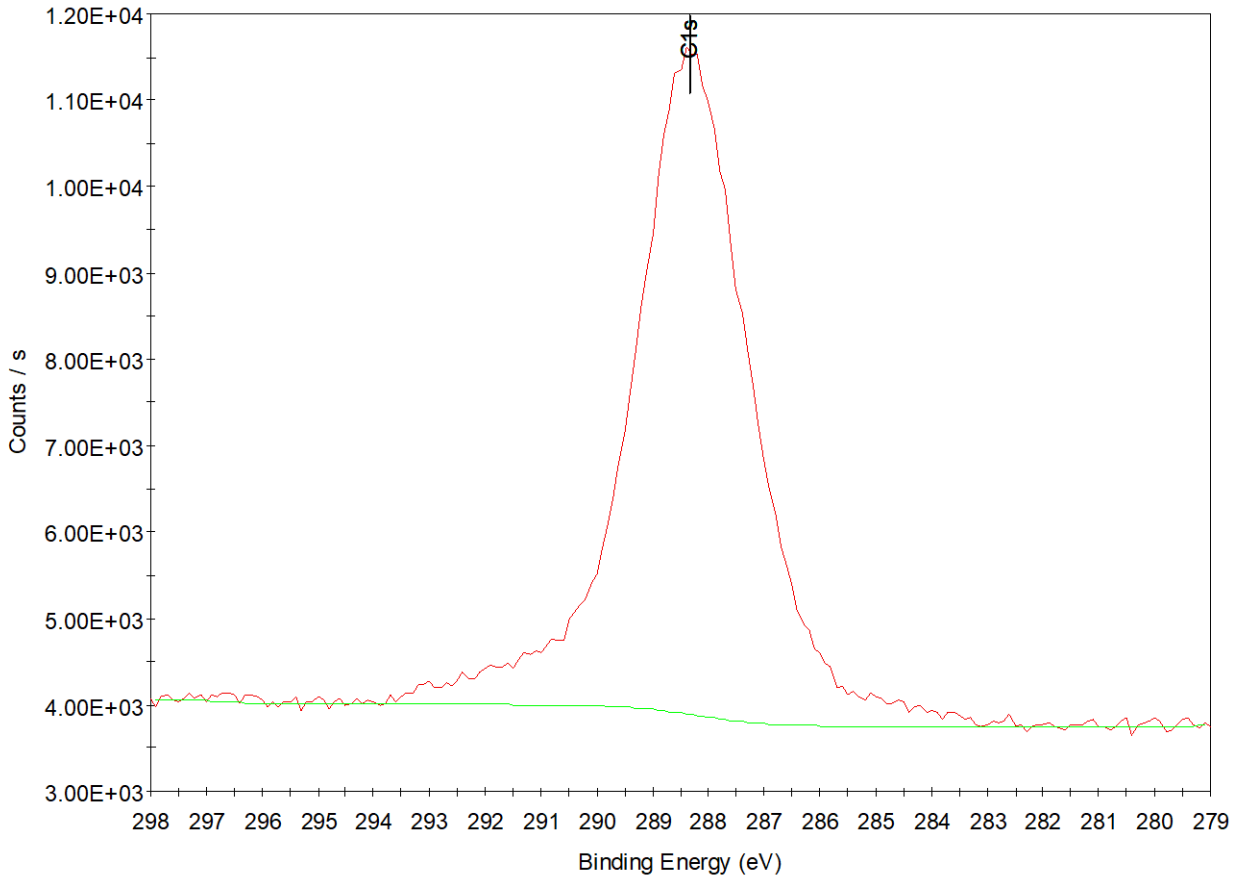

Figure 43. Elemental scan of carbon on a 48 hours aged alumina surface.

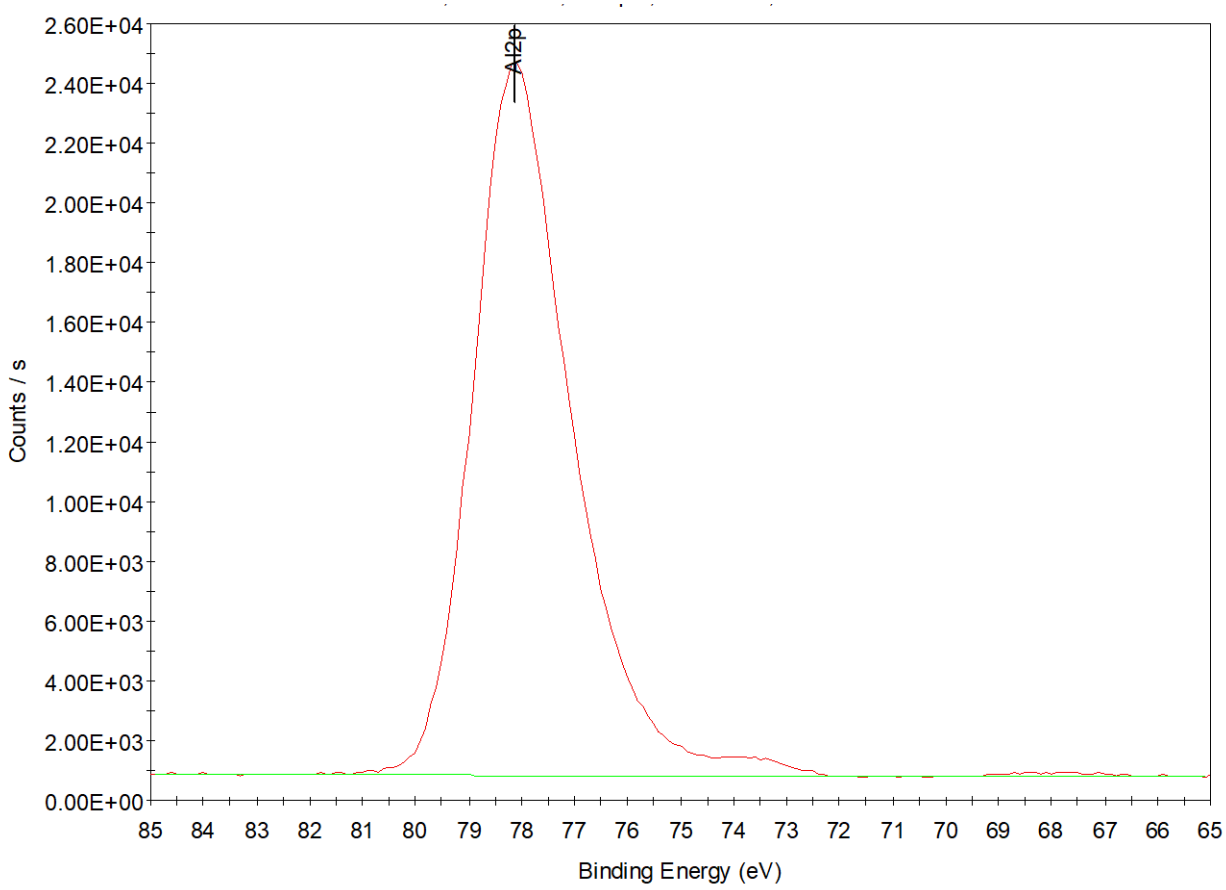

Figure 44. Elemental scan of aluminum on a 48 hours aged alumina surface.

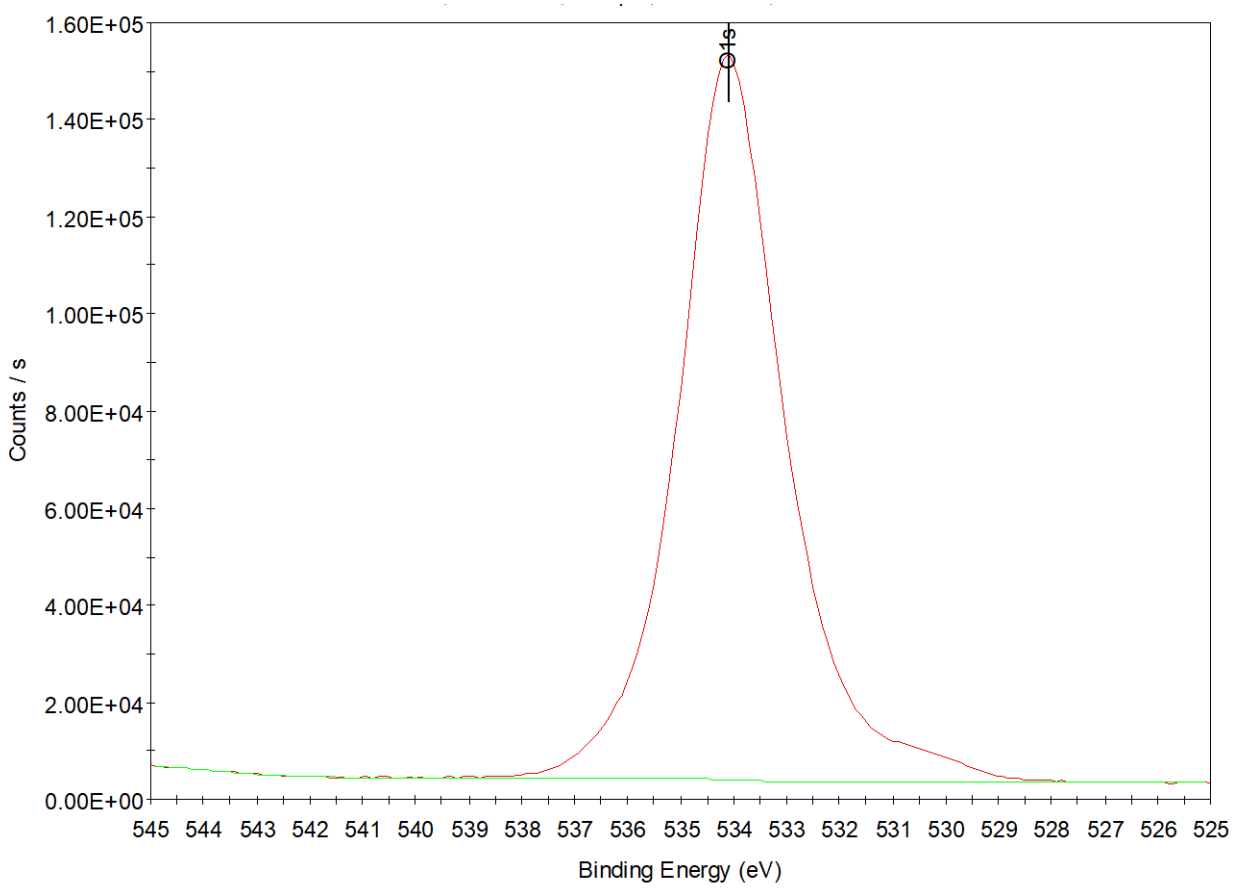

Figure 45. Elemental scan of oxygen on a 48 hours aged alumina surface.

Below is the set of data for 1 week aged alumina in figures 46-48.

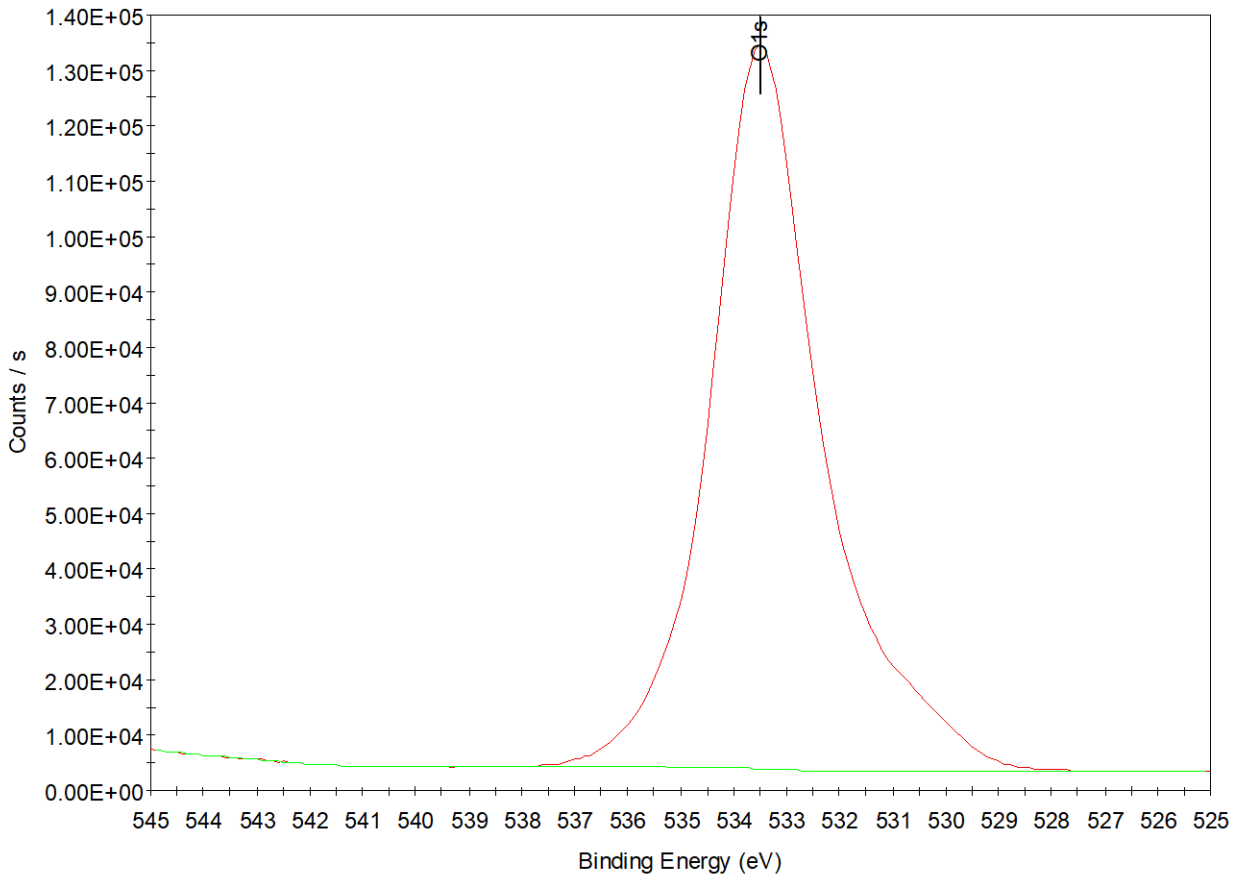

Figure 46. Elemental scan of oxygen on a 1 week aged alumina surface.

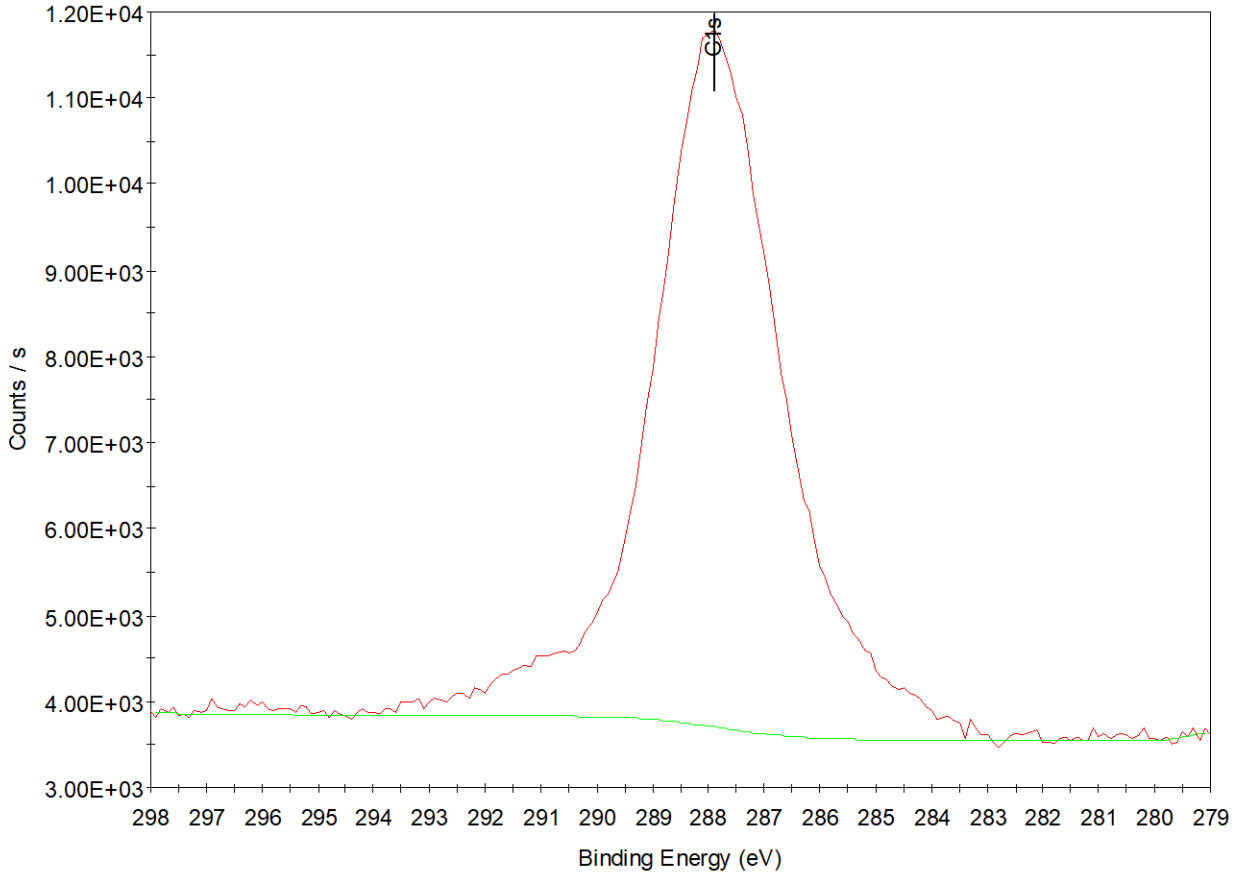

Figure 47. Elemental scan of carbon on a 1 week aged alumina surface.

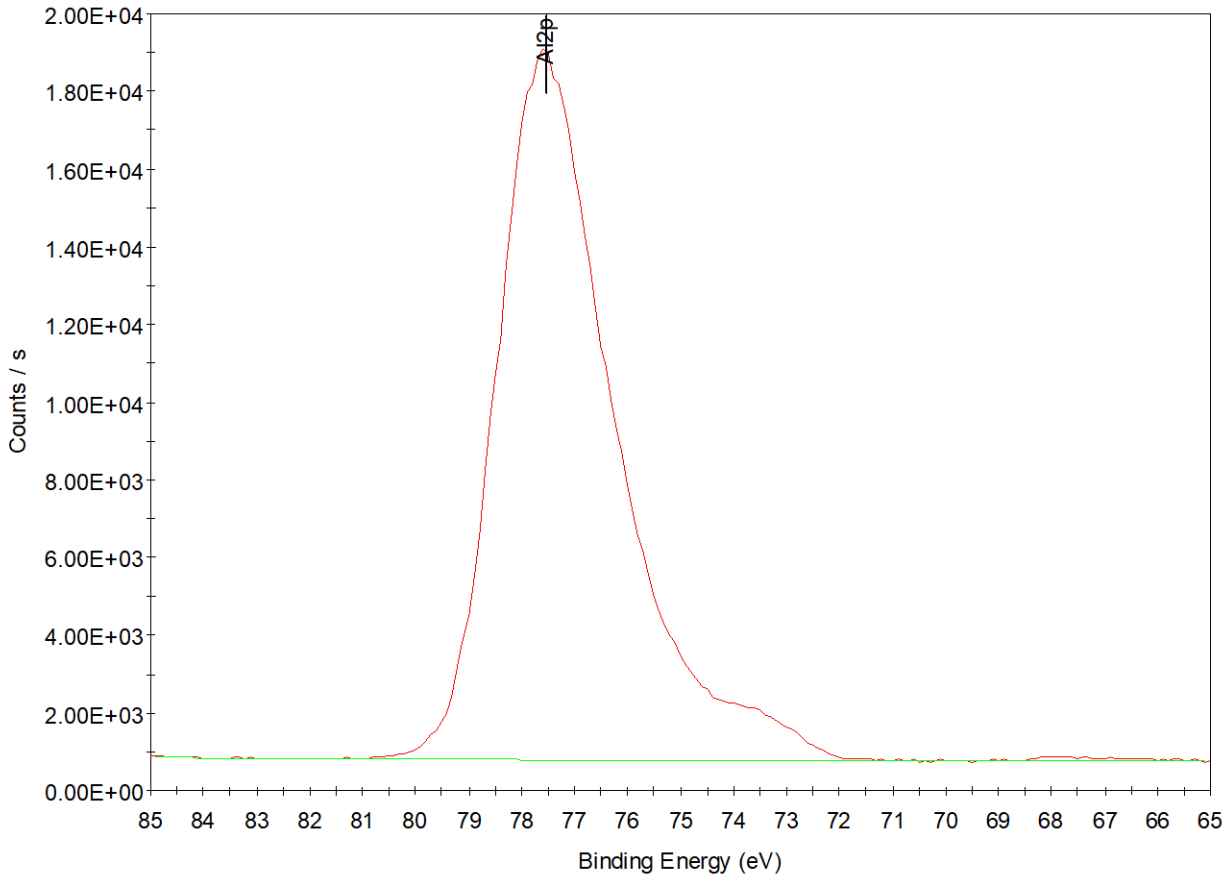

Figure 48. Elemental scan of oxygen on a 1 week aged alumina surface.

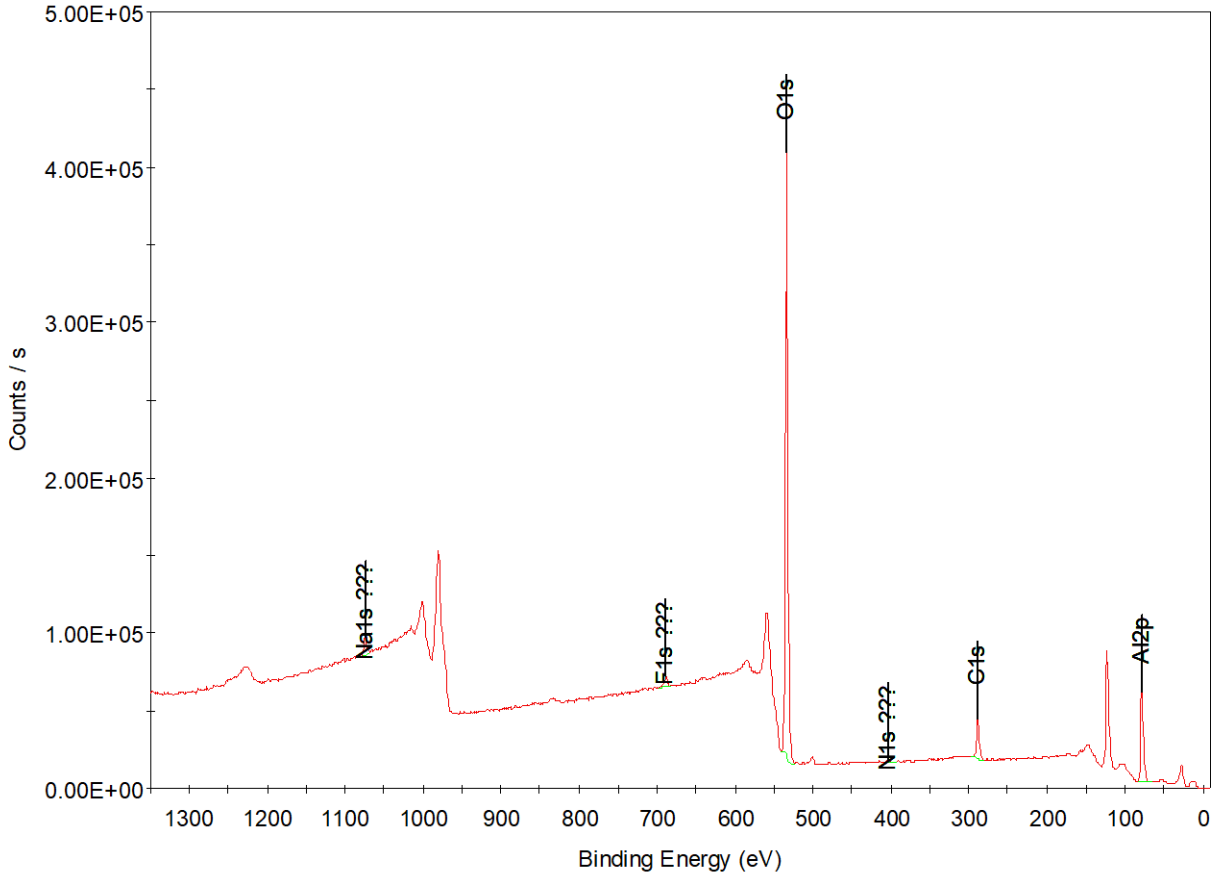

Figure 49. Survey scan on a 1 week aged alumina surface.

Below in **Table 2**, the elemental percentages are shown. This was calculated by the software and is based on the integrations of each peak.

Table 2. Elemental percentages of XPS peaks for alumina.

Days aged	Al2p	O1s	C1s
0	36.45	60.62	2.93
1	35.14	59.92	4.93
2	35.4949	56.3607	8.1444
7	34.6405	55.1686	10.191

The XPS data below corresponds to the air aging of silica in figure 27A in the main text. Survey scans for ozone cleaned and 1 week aged are also included. The carbon spectra include multiple peaks for the silica experiments. The carbon peaks above 285 eV correspond to carbons substituted with heteroatoms. The higher the binding energy, the more electronegative the heteroatom(s). It is likely that there are some oxygenated species on the surface.

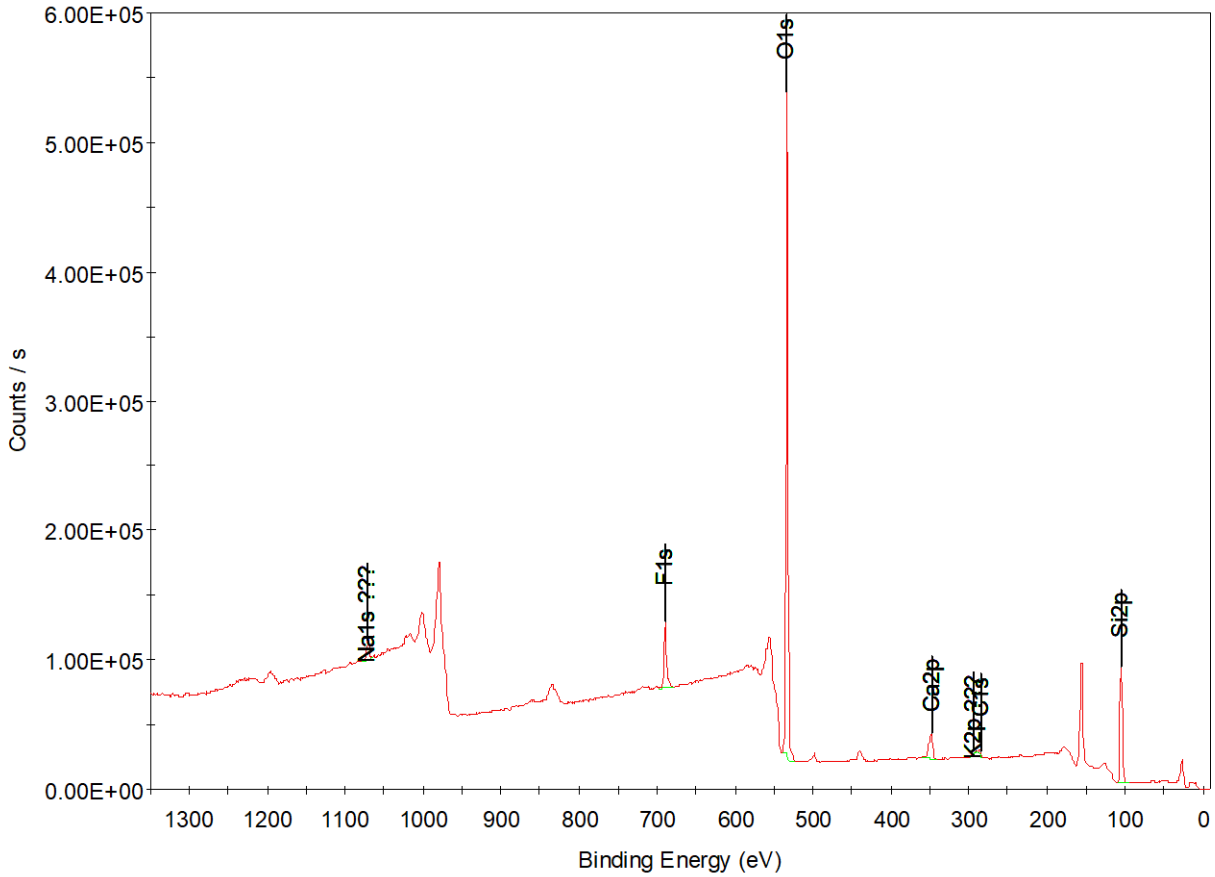

Figure 50. Survey scan on an ozone cleaned silica surface.

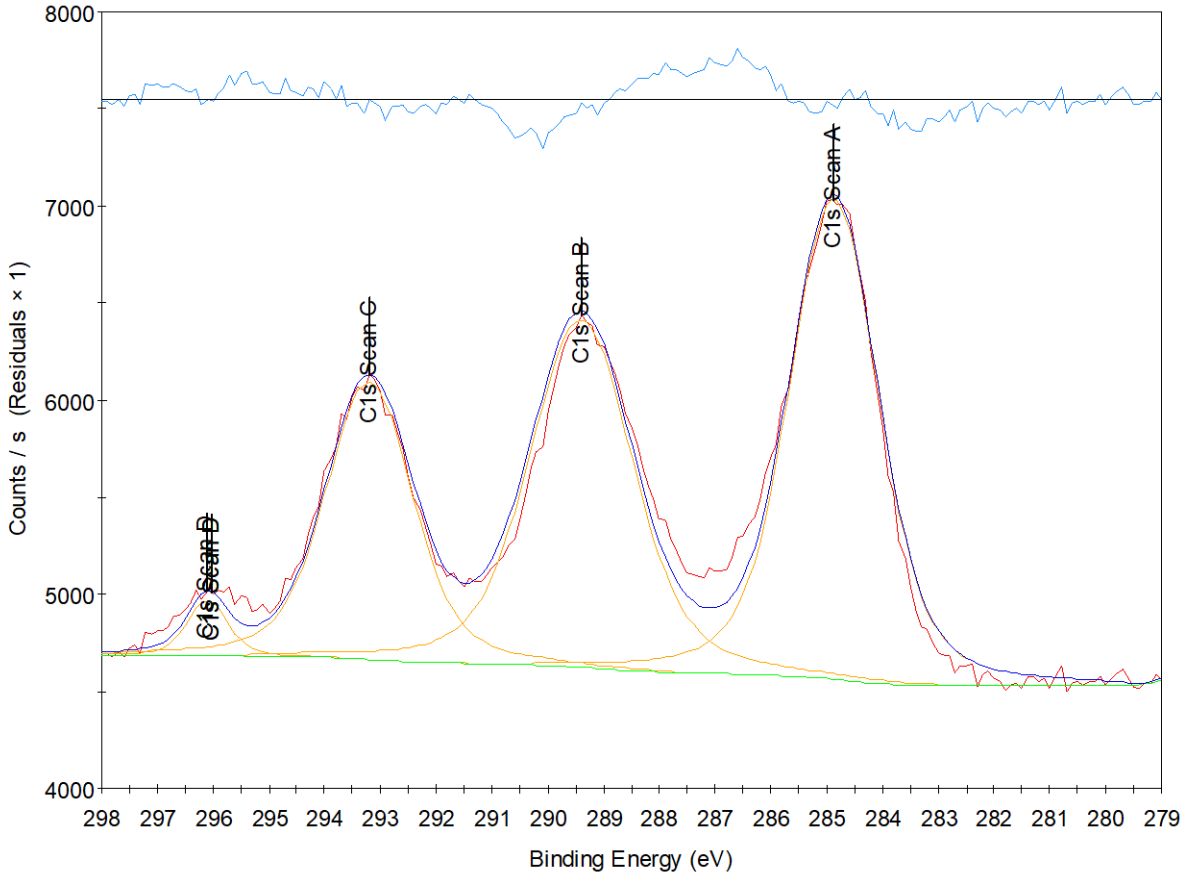

Figure 51. Elemental scan of carbon on an ozone cleaned silica surface.

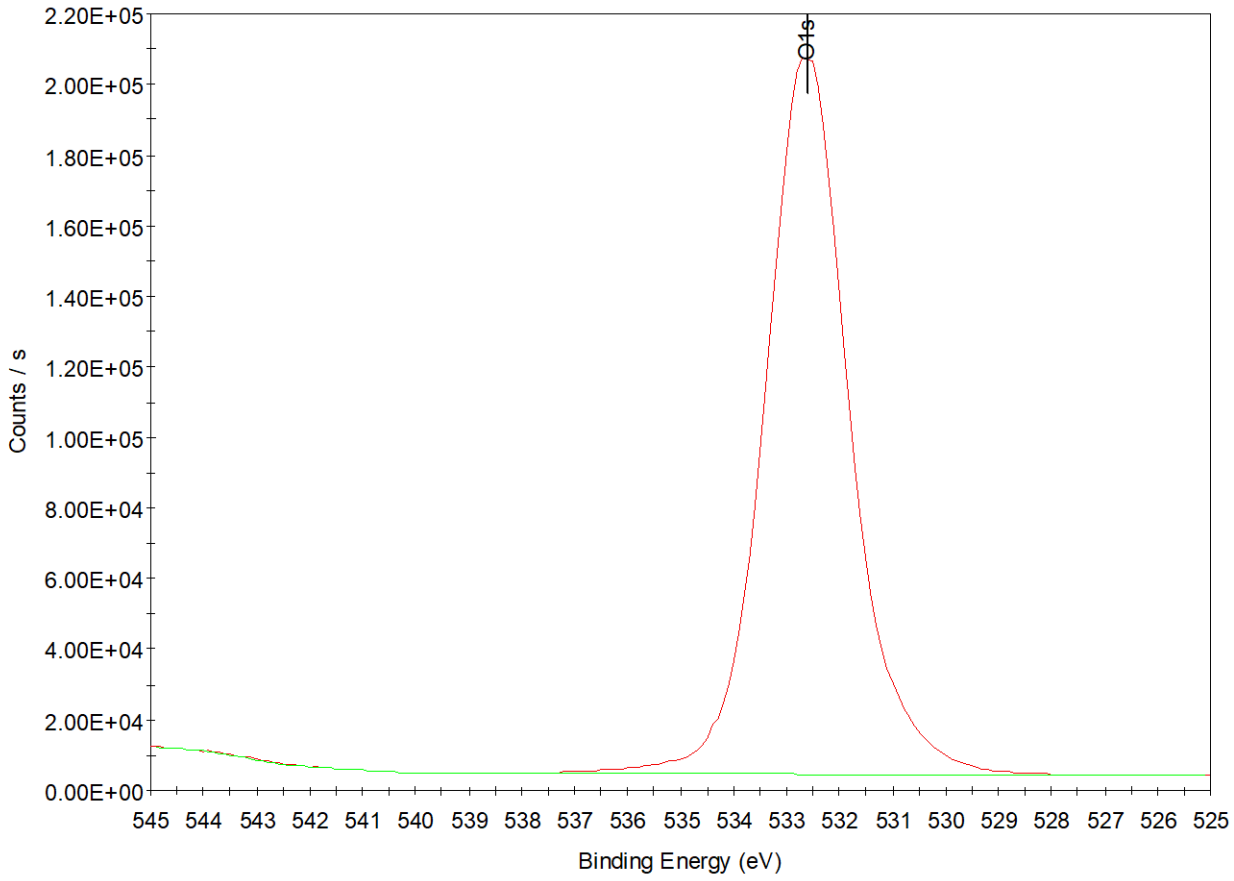

Figure 52. Elemental scan of oxygen on an ozone cleaned silica surface.

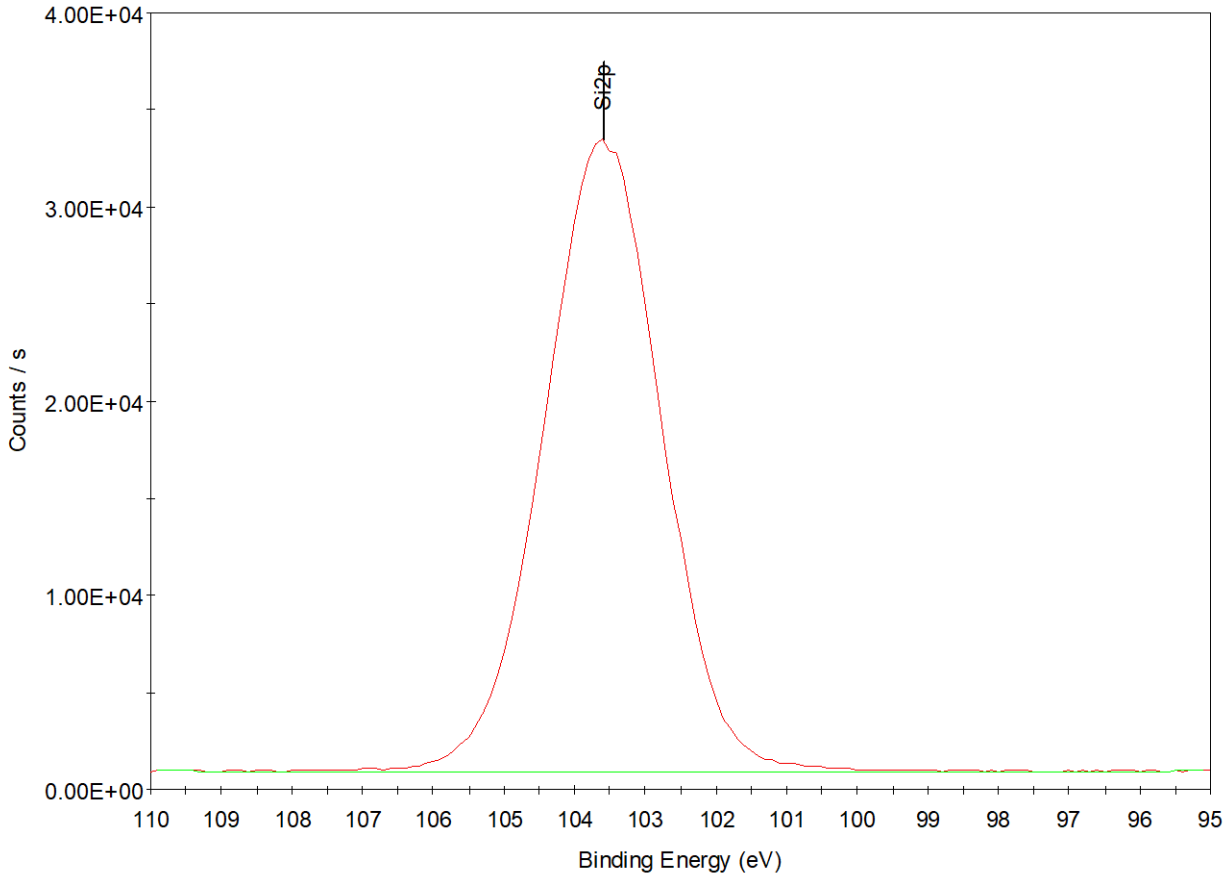

Figure 53. Elemental scan of silicon on an ozone cleaned silica surface.

Figures 54-56 below are of silica aged in air for 24 hours.

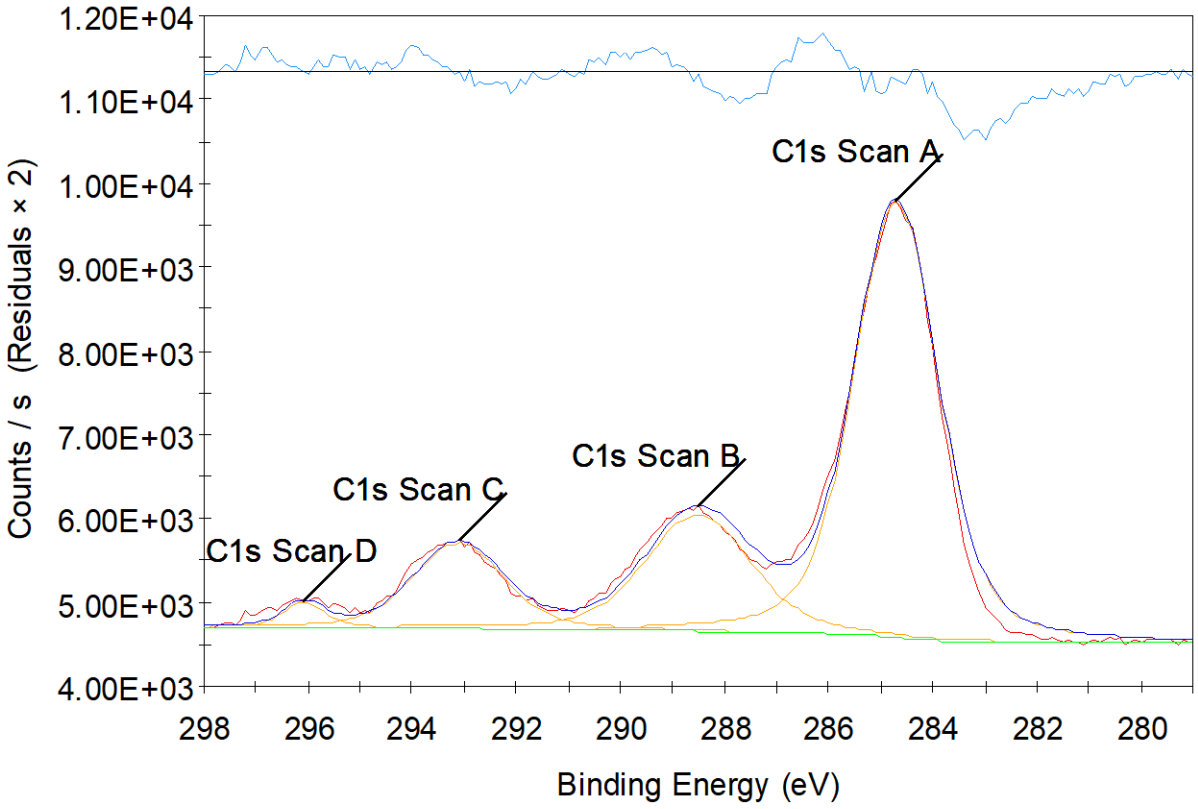

Figure 54. Elemental scan of carbon on a 24 hours aged silica surface.

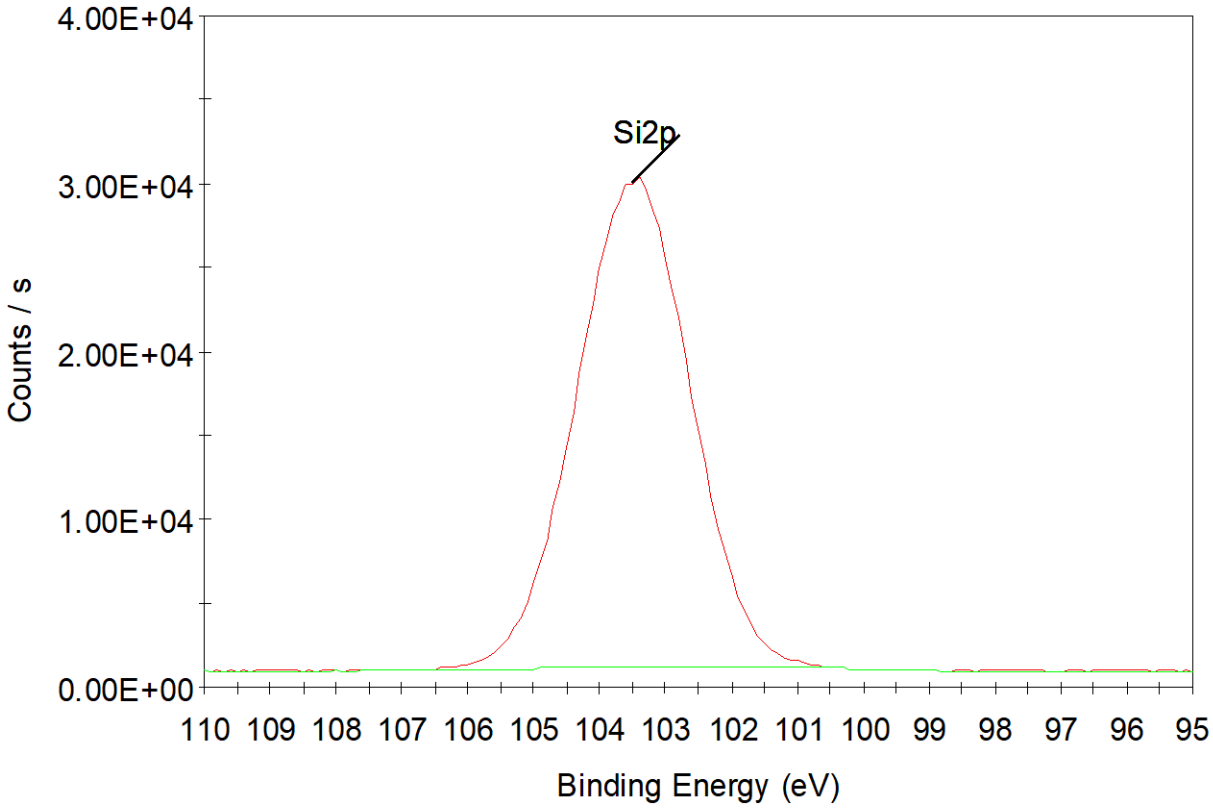

Figure 55. Elemental scan of silicon on a 24 hours aged silica surface.

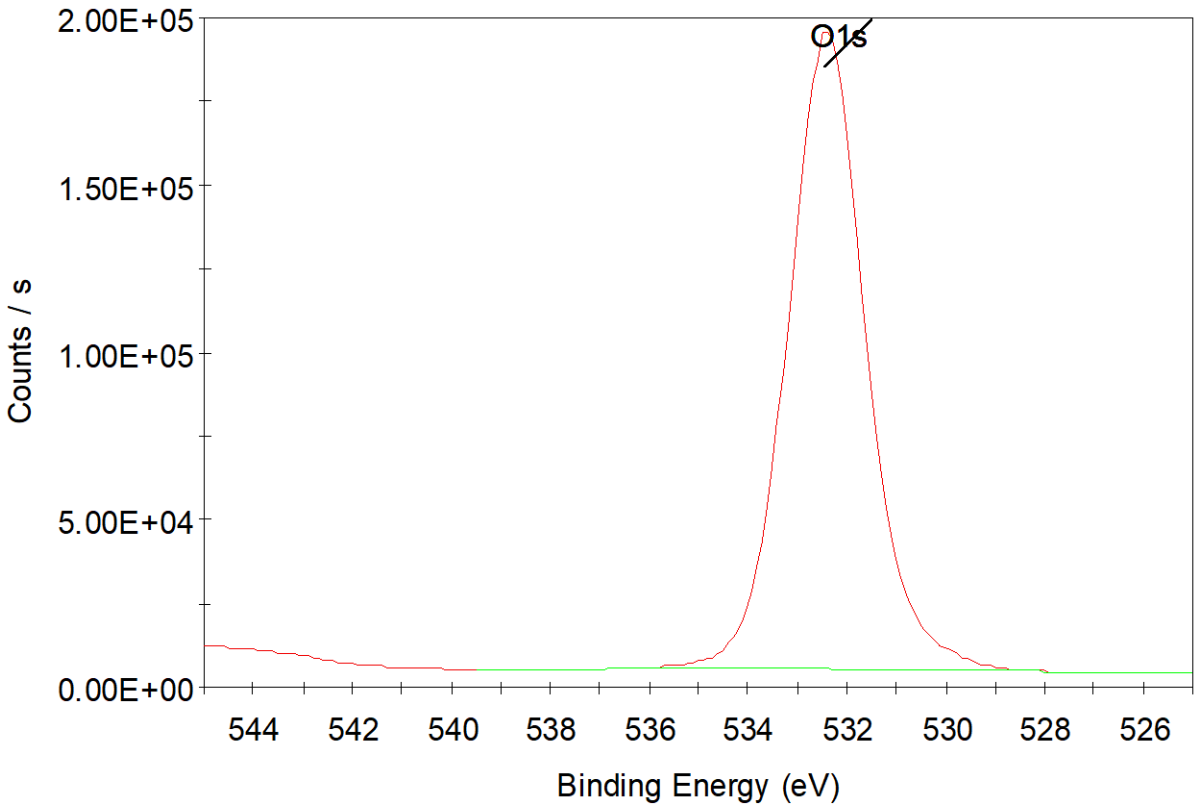

Figure 56. Elemental scan of oxygen on a 24 hours aged silica surface.

Figures 57-59 below are of a silica wafer aged 48 hours in air.

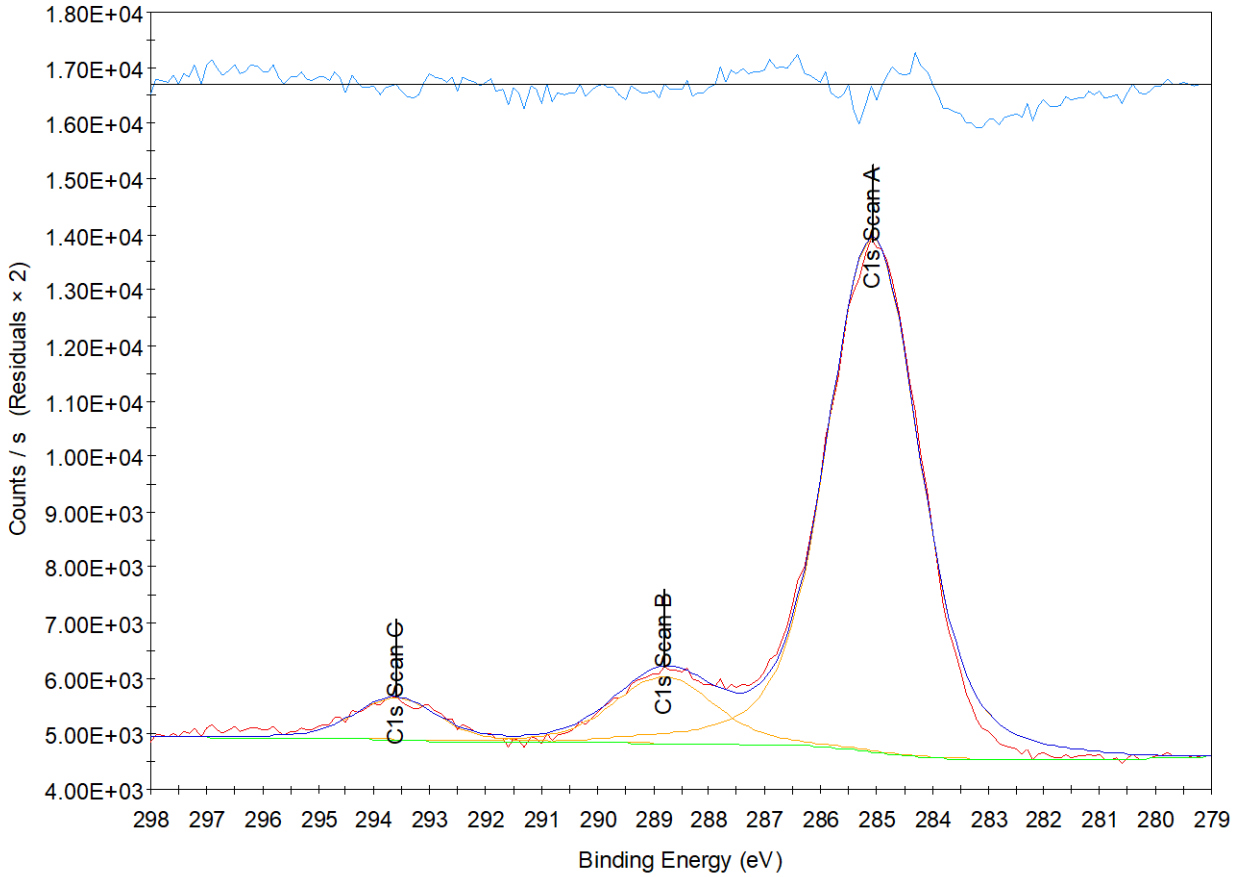

Figure 57. Elemental scan of carbon on a 48 hours aged silica surface.

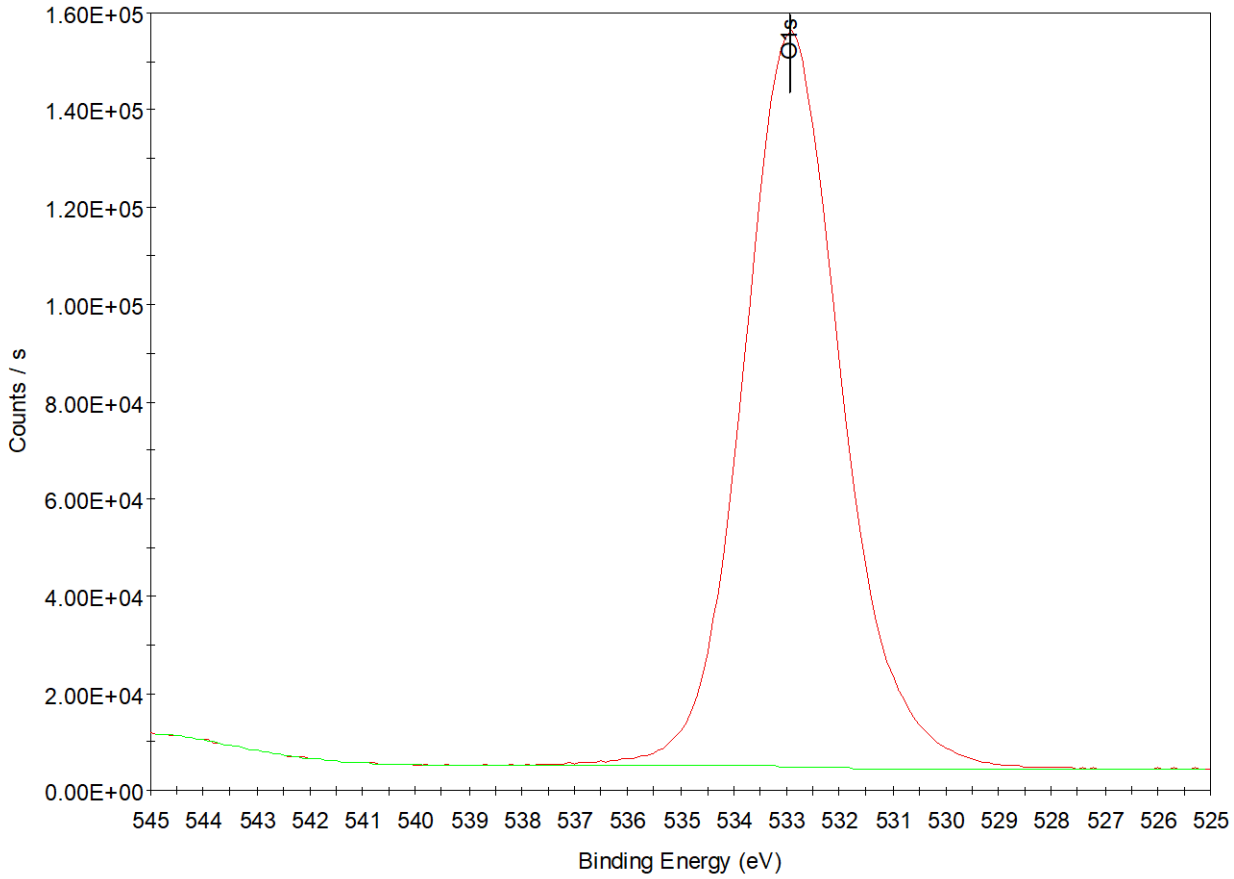

Figure 58. Elemental scan of oxygen on a 48 hours aged silica surface.

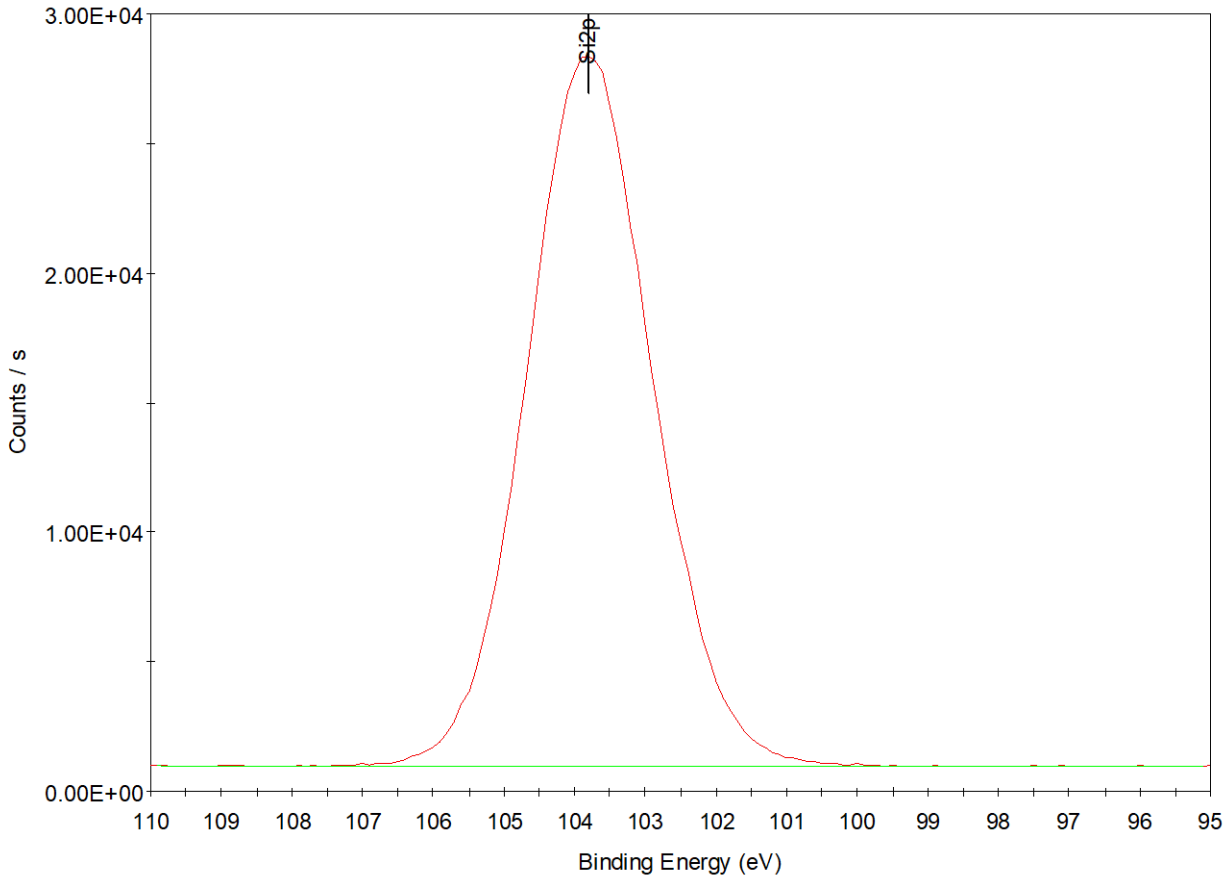

Figure 59. Elemental scan of silicon on a 48 hours aged silica surface.

Figures 60-62 below are of a silica wafer aged 1 week in air.

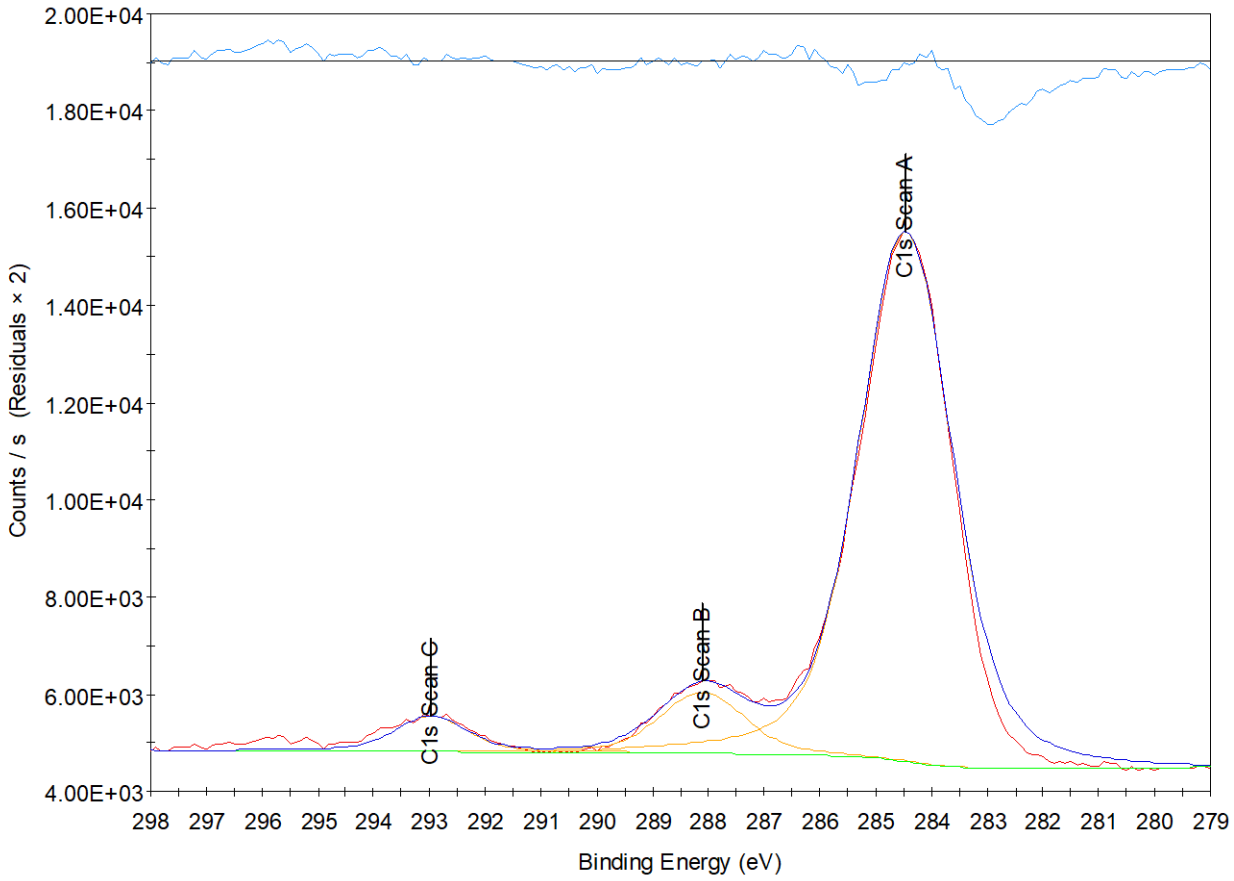

Figure 60. Elemental scan of carbon on a 1 week aged silica surface.

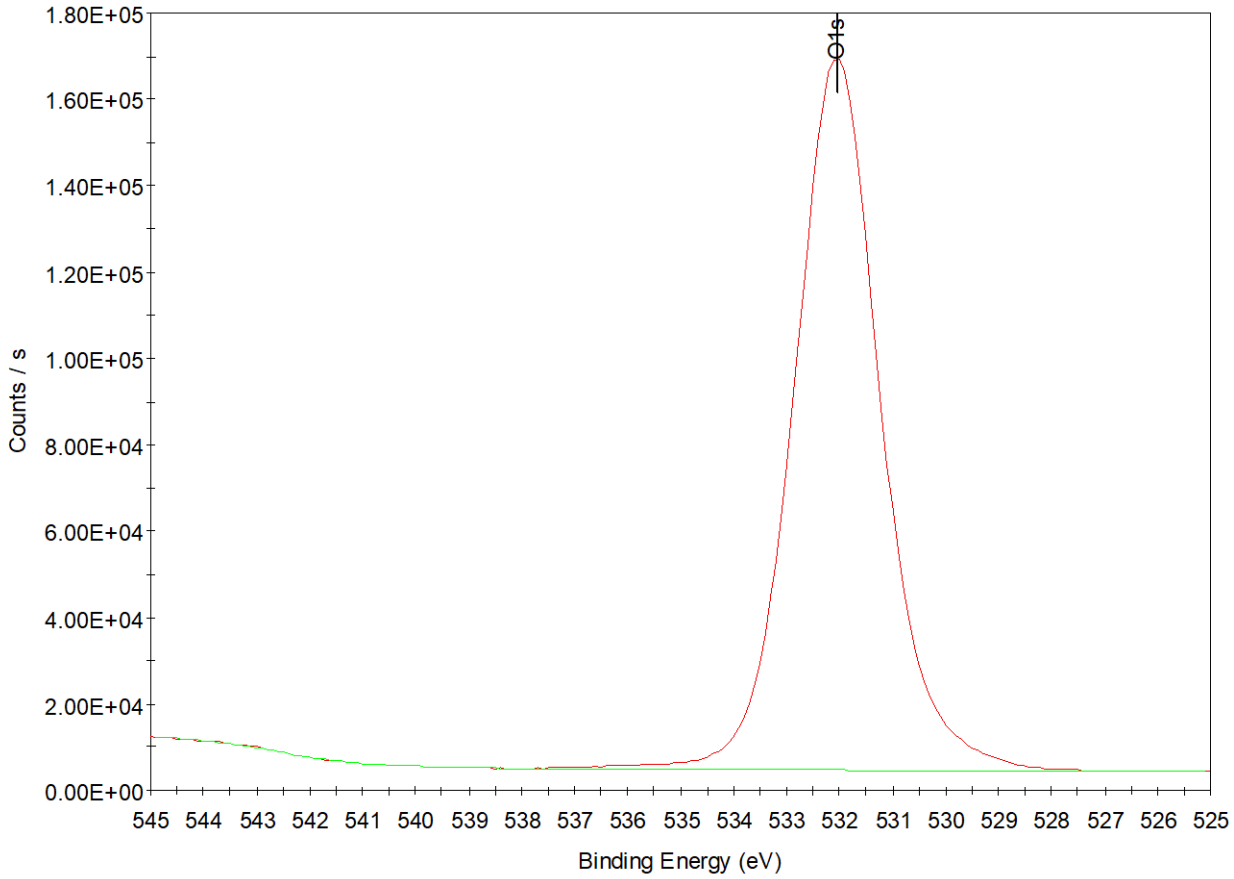

Figure 61. Elemental scan of oxygen on a 1 week aged silica surface.

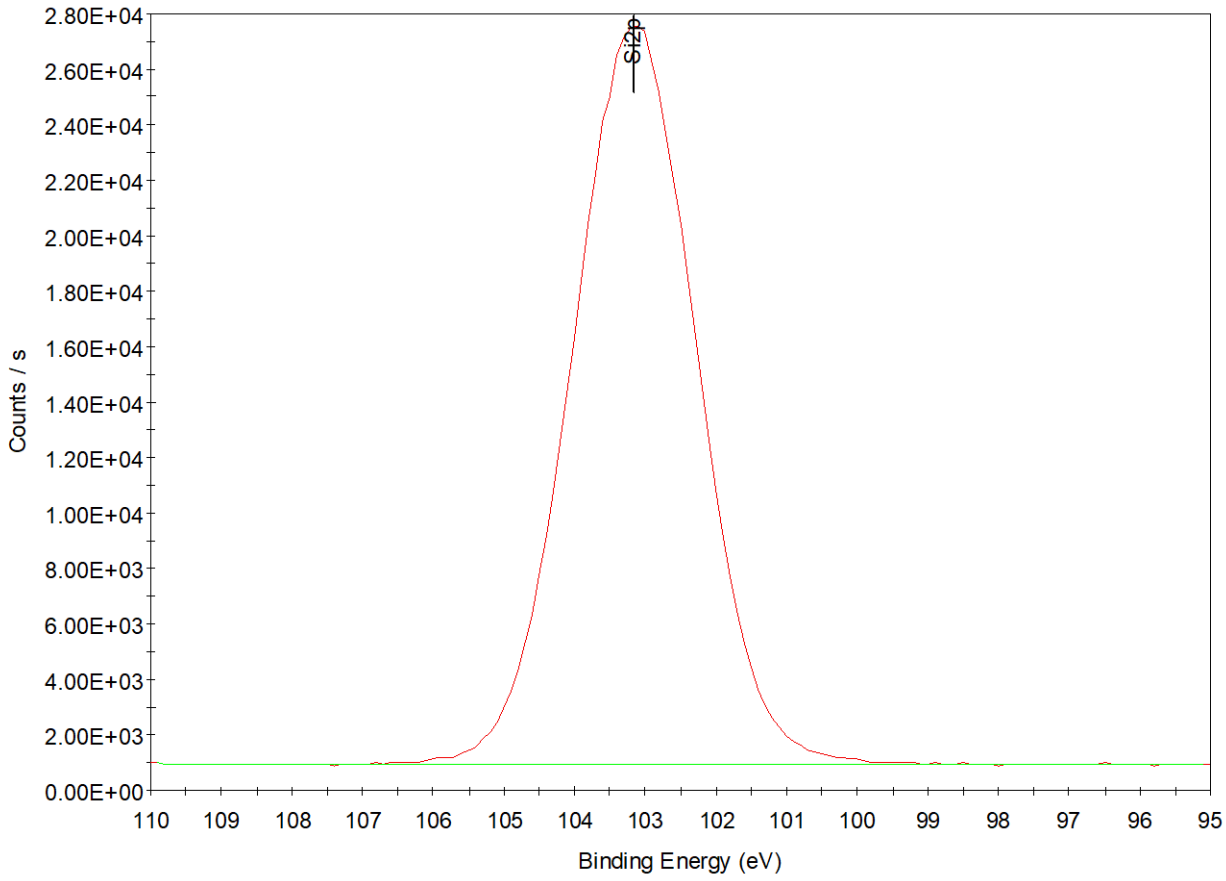

Figure 62. Elemental scan of silicon on a 1 week aged silica surface.

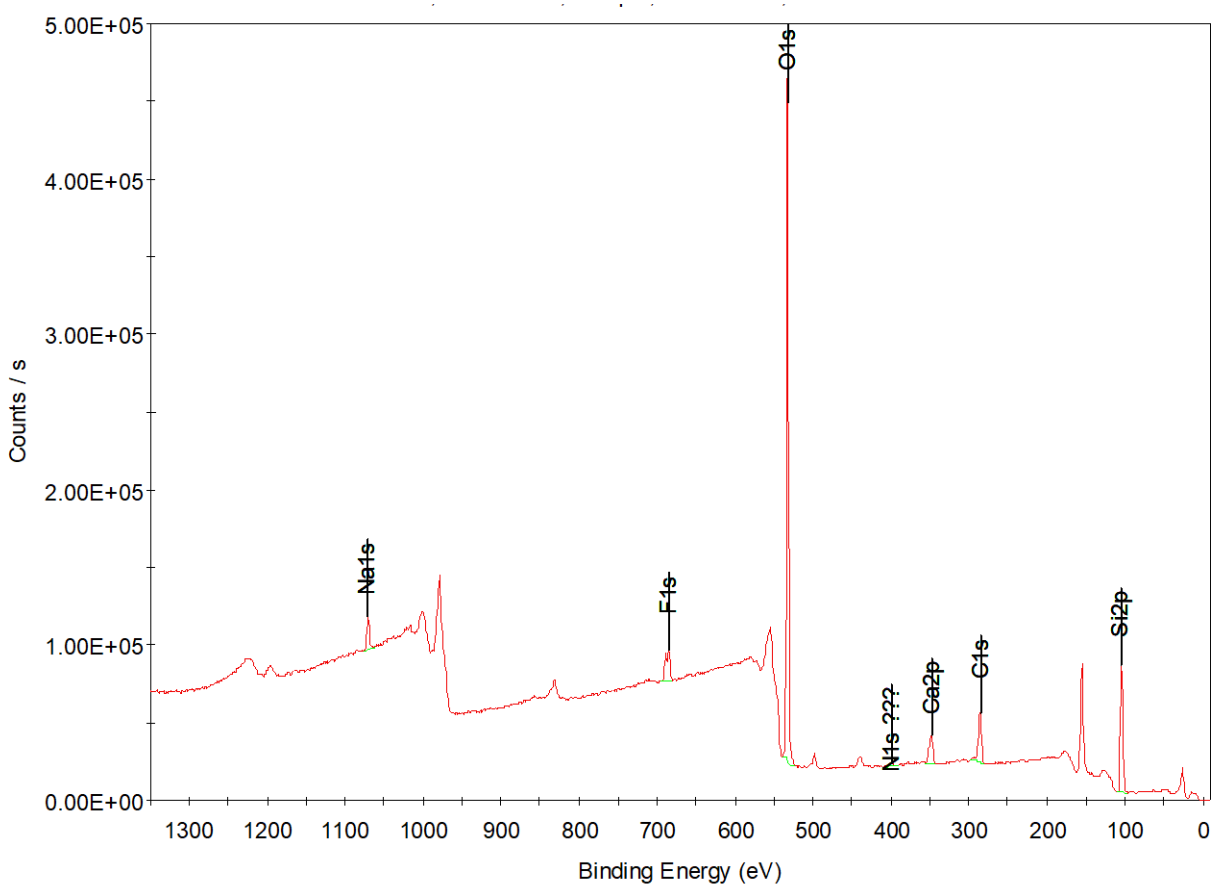

Figure 63. Survey scan on a 1 week aged silica surface.

Table 3. Elemental percentages of the XPS peaks for silica.

Days aged	O1s	Si2p	C1s Scan A	C1s Scan B	C1s Scan C	C1s Scan D	C 1s total
0	64.9715	29.1423	2.4007	2.006	1.3519	0.1276	5.8862
1	64.4	29.33	3.83	1.44	0.87	0.14	6.28
2	59.7264	28.3489	9.8006	1.3934	0.7307	0	11.9247
7	58.6986	27.5257	11.9199	1.237	0.6188	0	13.7757

Appendix B.2 Detailed Experimental Conditions of Figure 29

As stated in figure 29 of the main text, here we will reiterate the specific experimental conditions experienced by each of the samples in figure 29. Untreated, UV/Ozone, and Heated WDPT tests are replotted and share the same data as several points in figure 28. UV/Ozone treatment is for one hour, and heat treatment is at 95 °C for one hour. The heat and ozone test is unique to this figure, and shares the experimental conditions.

Percent surface carbon was determined by XPS. Ozone treatment was for one hour, and heat treatment was 3 hours at 300°C. The heat and ozone XPS experiment was ozone treated for 5 minutes after being heated for 3 hours at 300°C. Note that the ultra-high vacuum (UHV) required for XPS measurements may result in partial desorption of carbon-containing species on the kaolin particle surface as in the case of SiO_2 and Al_2O_3. The amount of time between heat treatment and measurement was several minutes, but the UV/ozone treatment immediately preceded the measurement (< 5 min. between treatment and measurement). There is the added time of pumping down the vacuum chamber for the XPS measurements. Also, the XPS measurements are performed on a small amount of powder, whereas the WDPT experiments were on the pressed pellets.

Appendix C Assessing and Mitigating Surface Contamination of Carbon Electrode Materials

Appendix C.1 Preface

The content of this section has been published in the journal *Chemistry of Materials*.

List of authors*:* Justin Mitchell Hurst[†], Min A Kim[†], Zhenbo Peng, Lei Li[*], and Haitao Liu[*]

[†]: these authors contributed equally.

*: corresponding authors: lel55@pitt.edu (L.L.) and hliu@pitt.edu (H.L.)

Despite a few studies reporting otherwise, graphitic carbon surfaces were generally thought to be hydrophobic prior to 2010s. However, many reports in the past six years showed that they are much more hydrophilic than previously thought. It was revealed that hydrocarbons adsorbed from ambient air masked the intrinsic surface wettability. Later work showed that other surface properties such as double layer capacitance and heterogeneous electron transfer rate were also impacted by the same contamination phenomenon. Since surface contamination is difficult to avoid completely, it is increasingly important to take this effect into consideration in both experimental design and data analysis. Will the experiment be negatively impacted by the unintentional contamination from the environment? How is one to properly characterize the surface to detect potential contamination? How can the contamination be removed if it has already occurred? In this protocol paper, we try to answer these questions by reviewing the background of

airborne contamination of graphitic carbon materials and outlining procedures to properly handle them in the research lab to minimize its negative impact on experiments.

Appendix C.2 Introduction

In ambient conditions, volatile organic compounds in air can affect the interfacial properties of the substrate by partially or completely passivating the surface. Unlike bulk materials, the number of atoms in the surface layer is limited to the order of 10^{15} atoms/cm^2. Therefore, even a very small amount of contaminant from ambient environments can have significant effects on the characteristics of the surface. It is well known that polar surfaces, such as metals and ceramics, attract non-polar organic compounds in air to reduce their surface energy. For example, the effect of surface contamination and cleaning on the electrode performance has been reported for many metal and metal oxide materials, such as indium tin oxide,[122-123] Pt,[124-125] Au,[126] and even diamond.[127] In the semiconductor industry, extensive indoor air control is often used due to the anticipation of the adsorption of airborne molecular contaminants on the material surface upon their exposure to the atmosphere.[128-131] Hydrocarbon adsorption has also been a well-known phenomenon in ultra-high vacuum (UHV) surface science.[4, 132-134]

Graphitic materials are good electrical conductors with chemical inertness. With plentiful natural reserves, graphitic carbons are one of the most extensively studied materials in chemistry and materials science. Their applications are widespread in many areas, such as electrochemistry, energy storage, lubrication, and composite materials. Unlike the cases of metals and ceramics, many researchers did not expect surface contamination when using pristine graphitic materials in ambient conditions. This expectation is not totally unwarranted because graphitic surfaces (*e.g.*,

basal plane graphite and graphene) are non-polar and usually have very low defect density. As such, one expects them to be low surface energy and less susceptible to the contamination by airborne hydrocarbons. We note that the effect of contamination on defect-rich carbon materials, such as glassy carbon, has been extensively studied. For example, the presence of minute amount of organic contaminants, even that from the operator's hand, was reported to significantly degrade the performance of glassy carbon electrodes.[135-136]

Since 2013, several research groups, including ours, have reported the effect of unintentional surface contamination on wettability and other surface properties of graphitic carbon materials.[28, 137-142] During the same time period, the rise of graphene research also rekindled the interest in the intrinsic surface properties of carbon materials, as contamination greatly reduces material and device performances of graphene. Although adsorption of organic compounds on graphitic surfaces has been extensively studied within the surface science community under ultra-high vacuum (UHV) conditions, surface contamination from the *environment* is a much more complicated process and also a new concept to many researchers in the material science community. The goal of this paper is to review the airborne hydrocarbon contamination of graphitic carbon materials and provide detailed guidelines for properly handling these materials to minimize such contamination. Due to the widespread use of graphitic carbon materials in electrochemistry, many of our discussions are related to such applications. However, the characterization techniques and handling guidelines are applicable to other research fields (*e.g.*, tribology) as well. We hope this information will help researchers to better design their experimental protocols and improve their data analysis, reducing the inconsistencies and irreproducibility issues in the community.

Appendix C.3 Surface Contamination of Graphitic Carbon Surfaces

Once a clean solid surface is exposed in the ambient air, high molecular weight molecules (*e.g.*, hundreds of Daltons) in air can adsorb at room temperature to form an adlayer on the surface. Thus, it is important to be aware of the possible sources of volatile organic compounds near the material preparation area. Many polymeric materials can outgas (*e.g.,* plasticizer emission) and affect the hydrocarbon concentration of local air.[143-145] In order to minimize the volatile contamination sources, a separate air-controlled enclosed area could be used such as a specialized cleanroom.[128-129, 146] The UHV environment is also a good option to study well-defined clean surface. For measurements that require atmospheric pressure, specialized UHV system (*e.g.*, electrochemical cells coupled with an UHV chamber[147-149]) can be used to circumvent the airborne contamination.

For carbon materials, chemisorption typically occurs at step edges or point defects. Since the surface defect density of high-quality graphitic materials is typically very low, the contamination phenomenon we discuss in this paper are mostly physisorption in nature. Thermodynamically, the formation of an airborne hydrocarbon contamination layer on the graphitic carbon surface is governed by an adsorption isotherm, which is a function of partial pressure and temperature. In addition, the change in temperature can enhance or suppress the type of adsorbate interaction (physisorption vs. chemisorption). Other environmental controls should also be considered to avoid inconsistent contamination behavior. For example, relative humidity changes significantly depending on the season and weather conditions as well as the climate control setting of the research lab.[116] Water could rapidly adsorb onto graphitic carbon surfaces in high humidity and change the kinetics of hydrocarbon adsorption as well as the adlayer composition.

Specific to graphene, the adsorption kinetics could also be impacted by the supporting substrate. Due to the atomic thinness of graphene, adsorbed molecules can 'sense' the substrate through long range van der Waals interactions. In addition, the substrate could also change the adsorbate-graphene interaction by charge doping of graphene. As a result, the surface energy of graphene as well as its interaction with the adsorbates could be enhanced by the presence of a high surface energy substrate and vice versa.[150] This effect was first identified in the study of wetting properties of supported and suspended graphene and termed "wetting transparency".[151-153] Since the initial reports on the wetting transparency of graphene, contradicting studies have been reported on the wetting properties of graphene coated substrates which showed either complete, partial or no transparency.[137, 150, 154-158] The observed inconsistency was suggested to be due to many variable conditions, such as: intrinsic defects in CVD grown graphene, the graphene transferring process, surface charges, and adsorbate contamination. Most recent work concluded partial transparency. Careful consideration of those conditions should be practiced to avoid misinterpretations of contact angle measurement of graphene. For example, dynamic contact angle measurements can be used to identify the possible discrepancy induced by the defect density of graphite materials.[153, 159] A captive air bubble measurement and polymer free transfer method had been also used to reduce the contamination of graphene.[156-158]

Finally, it is worth noting that, in the ambient, the chemical composition of the contamination layer is often not well-defined, since the adsorbates could differ from lab to lab and region to region, thus impacting the kinetics of the adsorption process and the nature of the adlayer. This situation is very different from the traditional UHV-based surface science studies, where well-defined surfaces and adlayers are prepared and investigated. Despite these complications, labs across the world reported very similar results for the effect of airborne contamination on the

wettability of graphite and graphene,[27-28, 137-142, 158, 160-163] suggesting that some commonality exists in the properties of the airborne contaminants around the globe.

Appendix C.4 Negative Impact of Surface Contamination on the Interfacial Properties of Graphitic Carbon Surfaces

The end result of surface contamination is the formation of a *ca.* 0.5 nm thick hydrocarbon layer on the graphitic material surface.[27] This contamination layer has very different properties from those of the graphitic carbon itself. In particular, it is of much lower surface energy, has lower dielectric constant, and also electrically non-conductive. Any surface properties/processes that are sensitive to the composition of the top monolayer of the surface can potentially be impacted by the surface contamination. These properties/processes include, but are not limited to wettability, surface energy, friction, adhesion, adsorption, electron transfer, and double layer capacitance. Consequently, a wide range of applications can be sensitive to surface contamination, such as sensors, energy storage, lubrication, composite materials and water/air purification. Below we briefly discuss these issues.

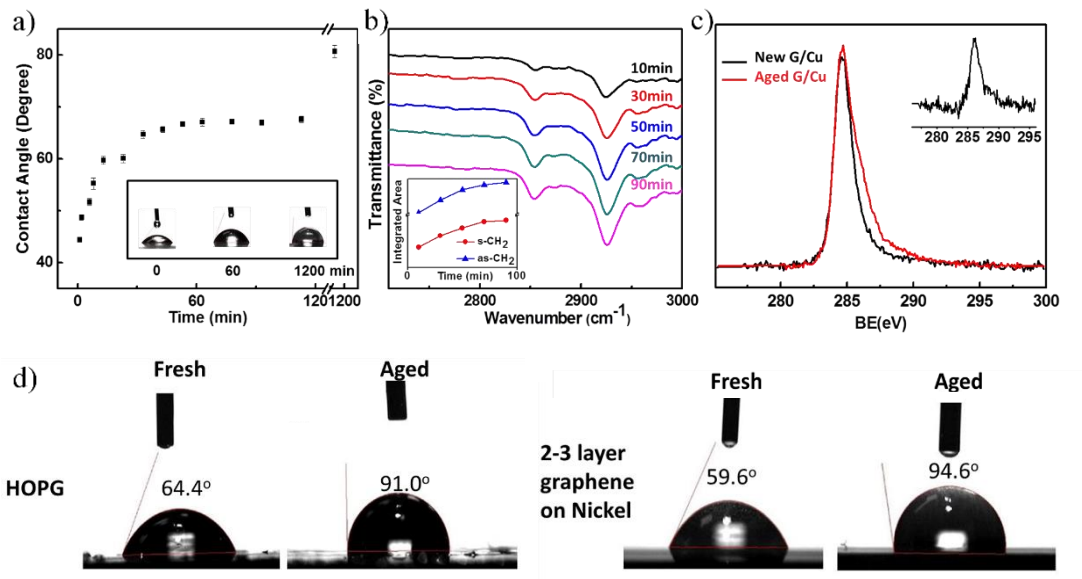

Figure 64. Airborne hydrocarbon contamination on copper supported graphene as characterized by a) water contact angle, b) ATR-FTIR, and c) XPS measurements. Panel a) and d) also highlight the effect of substrate (single layer graphene on copper vs graphite vs 2-3 layer graphene on nickel). Reprinted by permission from Nature Materials 2013, 12, 925. Copyright 2013 Springer Nature.

Since 1940, graphitic surfaces were generally accepted as being hydrophobic with a water contact angle of *ca.* 90 degrees.[164-165] Although significantly lower water contact angle of graphitic materials were reported in the 1970s,[160, 166] they did not change the mainstream view on the wettability of graphitic carbons.[153, 167-171] It was in 2013 that Li *et al.* reported the contamination of graphitic materials upon exposure to air.[137] They found significant hydrocarbon contamination on the graphene surface within minutes of ambient exposure via attenuated total reflectance – Fourier transform infrared spectroscopy (ATR-FTIR) and X-ray photoelectron spectroscopy (XPS) (Figure 64a-c). Similarly, such contamination also resulted in a significant change in water contact angle of highly oriented pyrolytic graphite (HOPG) and multi-layered graphene (2 – 3

layers on Ni) when the surfaces were aged in air for 2 days (Figure 64d). Following this work, a large number of groups have independently reproduced the major conclusions of Li *et al.* and have extended the study to other 2D materials, such as BN and MoS_2.[70, 172-176]

Hydrocarbon contamination significantly affects electrochemical properties, such as double layer capacitance and heterogeneous electron transfer rate.[71, 85, 141, 177] The contamination layer has low dielectric constant and its presence also pushes hydrated ions away from the electrode surface; both effects should lead to a decrease of the double layer capacitance.[71, 85, 178-179] Figure 65a-c shows that the double layer capacitance of HOPG decreased by about 30% after extended air exposure, and by 38% when aged in 1 M NaCl solution. Addition of intentional contaminants (1-octadecene) to the atmosphere caused a 70% reduction in the capacitance. In contrast, adding benzyl alcohol to the electrolyte slightly reduced the capacitance loss compared to the case of NaCl solution only; this unexpected observation was attributed to the high dielectric constant of benzyl alcohol. [85] Duignan *et al.* has reported a detailed model to account for the effect of surface contamination on the double layer capacitance of graphite.[178]

Traditionally, it was believed that the basal plane of HOPG has very low electrochemical activity and that high electron-transfer kinetics originates from step edges and other defect sites.[180-185] With the advances in electrochemical imaging techniques, recent studies claimed that the defect-free basal plane is also highly electroactive.[186-192] The time dependency of those electrochemical measurements was reported independently by different researchers.[141, 177, 191-196] Although the exact mechanism behind the conflicting results is still elusive,[194-196] the fact that some early studies used graphite/mineral oil paste (*i.e.*, a potential source for airborne hydrocarbon) to fix graphite electrode[197] as well as the observed correlation between the hydrocarbon contamination and the reduced electroactivity of HOPG surface suggests that the

ambient surface contamination is a likely factor. For example, the electron transfer kinetics (k^0) of air aged HOPG electrodes have been shown to be 2 to 250-fold slower than *in situ* cleaved ones, depending on the redox couple used in the measurement.[177] Scanning electrochemical microscopy (SECM) measurements have shown an unprecedentedly large k^0 of ~15 cm/s, approaching that of noble metal electrodes, by reducing the airborne hydrocarbon contamination and limiting the total organic carbon (TOC) in the electrolyte to 1 ppb (Figure 65d).[141] In an SECM measurement, an electrode with a micrometers sized surface area is brought within nanometer distance of the electrode being studied. Such small distance increases mass transport efficiency to allow measurement of extremely high k^0 values. Shown in Figure 65d, reducing the TOC in the electrolyte from 20 ppb to 1 ppb significantly increased the collected current, which was attributed to the reduced contamination of the surface. Using SECM imaging, Frederix *et al.* observed an anomalously low activity of HOPG that did not correspond to a topological structure. [188] This feature was later attributed to hydrocarbon contamination by Nioradze *et al*.[141] For a more detailed discussion, refer to this review.[186]

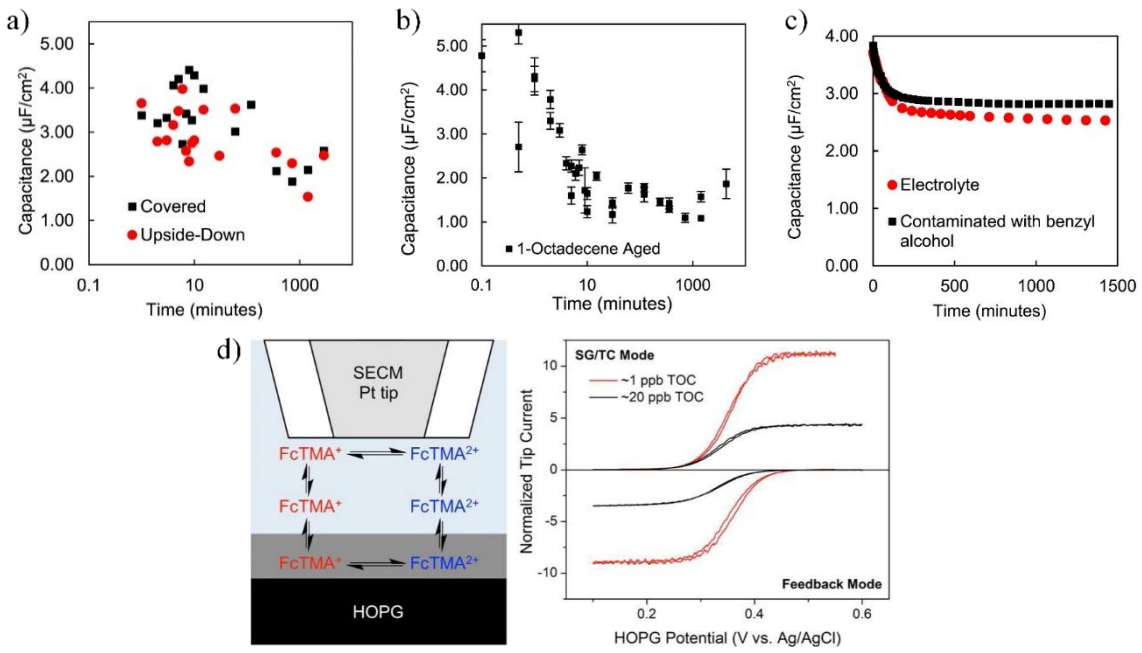

Figure 65. The effects of hydrocarbon contamination on the electrochemical properties of HOPG. Double layer capacitance measurements on HOPG aged in (a) ambient air and (b) 1-octadecene vapor, and c) 1 M NaCl solution without and with added benzyl alcohol. Reprinted with permission from Hurst et al., *Carbon* 2018, 134, 464. Copyright 2018 Elsevier. d) Nanogap voltammograms measured on HOPG in ~1 ppb TOC and ~20 ppb-TOC water containing 0.3 mM $FcTMA^+$ and 0.05 M KCl. Reprinted with permission from Nioradze et al., *Analytical Chemistry* **2015**, *87*, 4836-4843. Copyright 2015 American Chemical Society.

Appendix C.5 Characterization of the Contamination Layer

Given its significant impact on interfacial properties, it is important to assess the presence and magnitude of surface contamination on graphitic carbons. Unfortunately, many techniques that may otherwise be appropriate for surface analysis are insufficient for studying hydrocarbon

contamination on graphitic carbon materials. As both the substrate and the contaminant are largely carbon, they can be difficult to differentiate. For example, XPS can detect elemental composition for the top *ca.* 10 nm of the surface. Although there is a difference in binding energy between sp^2 and sp^3 hybridized carbon, proper deconvolution requires high resolution instruments. In addition, XPS is typically done in UHV, which could desorb weakly bound contaminants and change the adlayer composition. Ambient pressure XPS measurements are possible, but the same issue of peak deconvolution remains.[198] Another example in this case is secondary ion mass spectrometry (SIMS). SIMS can liberate ions from the first 1 – 2 nm of the surface. Harder ionization sources, such as oxygen or argon ion guns, can produce fairly small fragments that can provide some functional group information. Ashraf *et al.* used cesium sputtering to assess the amount of hydrocarbons on the surface.[161] They found various fragments ranging from elemental carbon to 5 carbon chains. However, it is difficult to determine the identity of the contaminant molecule with these sources. To detect molecular ions requires softer sources such as a fullerene ion gun.

The easiest method to qualitatively determine the level of contamination on graphite or graphene surface is water contact angle measurements. The water contact angle measured immediately after graphite exfoliation (*i.e.*, clean surface) should be within ~ 60 ° – 65 °, depending on the defect density of the sample.[159] The contact angle increases to about 90 ° after extended air exposure, although such change can occur as short as 10 min.[27] Major limitations of contact angle measurements are the limited time resolution due to the need to manually add droplets and the lack of chemical information. Contact angle measurements should also be considered destructive for many situations. Depositing water on the surface, and any possible contaminants in that water, will change the surface such that it can no longer be considered pristine.

Spectroscopic ellipsometry is non-destructive and offers much better time resolution compared to contact angle measurements. In ellipsometry, the measured data is fitted to a mathematical model, from which the average film thickness is obtained. Ellipsometry is highly sensitive; change of average adlayer thickness at the sub-angstrom level can be routinely detected with a time resolution of several seconds or less. However, similar to contact angle measurements, ellipsometry does not provide any chemical information. An added complication for graphite is that its optical properties often vary noticeably between exfoliations, possibly due to the variations in step edge density and end group functionalization. For this reason, ellipsometry is best used to measure the rate of adsorption. The kinetic data is referenced to the initial measurement, which is assumed to be a substrate with zero film thickness.

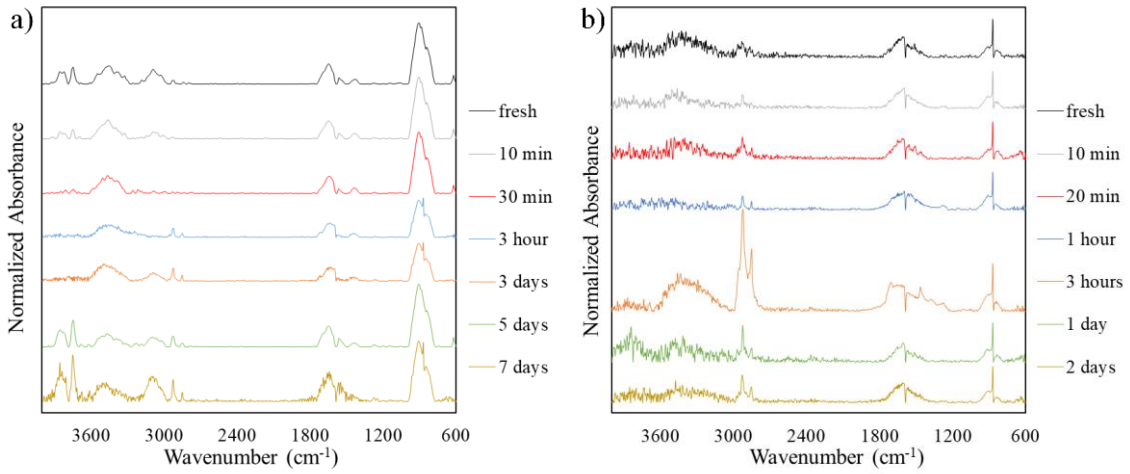

Figure 66. ATR-FTIR spectra with a) air aging and b) aging in 1-octadecene of HOPG. The data was reproduced with permission from Hurst, *et al.*; *Carbon* **2018,** *134*, 464-469. Copyright 2018 Elsevier.

For chemical analysis of the adlayer, reflectance FTIR (*e.g.*, ATR-FTIR) is the most often used technique. The most telling feature in the IR spectra are the methylene stretch peaks at 2850-

2950 cm^{-1} (Figure 66). The existence of such peaks is clear evidence of surface contamination. Generally, these peaks increase with longer aging times and increased contamination, but they are not always well behaved in our experience. For example, the initial peak intensity for HOPG varies greatly between exfoliations, and intermediate aging times do not always show a continuous trend. However, in almost all experiments, the freshly exfoliated measurement has the lowest peak intensity. Other peaks also appear in the FTIR spectra, but their behavior is not well understood. For example, peaks associated with aromatic hydrocarbons (*e.g.*, 3100-3000 cm^{-1} for aromatic C-H stretch, and 900-700 cm^{-1} for out-of-plane bending) can appear at early aging times but disappear during intermediate aging times (3 hours to 3 days) and reappear again at even longer air exposures (Figure 66). The intensity change of these peaks does not synchronize, suggesting that they may be originated from different molecules. One possibility is that the surface selection rule is changing the measured absorbances based upon the orientation of the molecules on the surface. Although graphite is a semimetal, it is possible that a limited selection rule may still apply.[199] Aromatics that lay flat against the surface may have their IR absorbances dampened below the detection limit of ATR-FTIR. Conversely, if the molecule is oriented perpendicular to the surface, the IR absorption could be slightly enhanced. To summarize, general trends do exist to qualitatively assess the level of surface contamination, but more work is needed to fully understand the types of organics that adsorb to graphitic surface and their dynamics.

Although we do not have positive identification of the contaminants on the surface of graphite, we do have some clues as to what they may be. As just discussed, there are peaks in the FTIR spectrum that correspond to aliphatic, and aromatic hydrocarbons. We also know from XPS data, that the amount of oxygen containing species on the surface increases over time. Recent work on ultraviolet photoelectron spectroscopy shows that the surface is contaminated very quickly with

low molecular weight, or weakly bound compounds, that slowly exchange for larger molecular weight hydrocarbons.[200] Most of the evidence we have points towards a model where small molecular weight species (including water) adsorb quickly, and are slowly replaced with larger molecular weight species that are more hydrophobic. We believe that the small molecular weight contaminants adsorb first due to faster kinetics, while the larger adsorbates are thermodynamically more stable on the surface.

Appendix C.6 Mitigating the Surface Contamination

Completely avoiding hydrocarbon contamination of graphitic surfaces is challenging, as hydrocarbons are quite ubiquitous in air. Although hydrocarbon-free air can be produced by using liquid nitrogen-cooled charcoal filters,[201] they are not practical for most research labs. Instead, we will address some procedural points that can be readily implemented to minimize the contamination from ambient exposure.

The first consideration is limiting the time the sample spends in air before measurement. Some prototypical ellipsometry data shown in Figure 67 will aid us in our discussion. In these measurements, we fixed the graphite to the sample holder and started the ellipsometry measurement before the graphite was exfoliated. By doing so, we can ensure that when the first data point is taken, the exfoliated surface has not been exposed to air for more than 15 seconds, which is the fixed acquisition time of our instrument. We can see that after about 1 hour in air the rate of adsorption slows and is very near its equilibrium thickness of ~0.5 nm. Although there are significant variations in the measured kinetics (Figure 67a), Figure 67b also shows that when water contact angle and ellipsometry data were measured at the same time, there is remarkable

correlation between the two. From these data, we can see that the adlayer thickness increases almost linearly in the early times. A contamination level of 1% corresponds to about 10 seconds to 1 minute of air exposure (Figure 67a), depending on the local environment. Note that the thickness reported by ellipsometry is the average over a macroscopic area. The smaller thickness levels correspond to partial surface coverage.

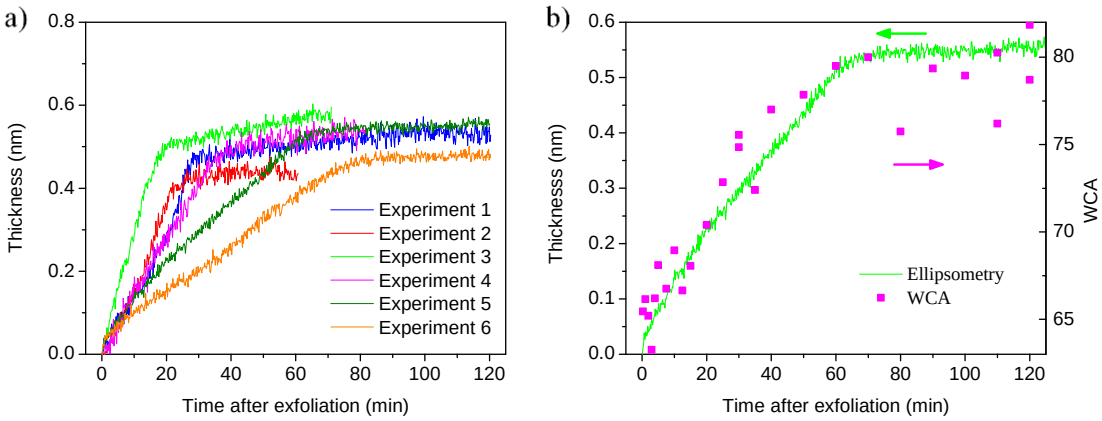

Figure 67. Spectroscopic ellipsometry (SE) monitoring of hydrocarbon layer thickness on HOPG exposed to ambient air after exfoliation at 0 min. Water contact angle and ellipsometry measurements on HOPG taken on the same sample, on the same day, and in the same lab. Reprinted with permission from Kozbial et al. "Understanding the intrinsic water wettability of graphite". *Carbon* **2014**, *74*, 218-225. Copyright 2014 Elsevier.

It has been shown that a purposefully adsorbed water layer on graphite or graphene can temporarily protect the surface from hydrocarbon contamination.[116] This technique could be useful if the experiment requires a significant amount of time between exfoliation and measurement, and hydrocarbon contamination needs to be minimized. Figure 68a-b show that when a graphite surface was covered with a monolayer of water (produced by low temperature condensation), its

contamination by ambient air was significantly slowed down. The same technique can also reduce the negative impact of the contamination on the electrochemical performance. Shown in Figure 68c-d, the water-covered HOPG sample, even after prolonged air exposure, showed no performance degradation in the cyclic voltammogram measurement and its ΔE_p (the separations between the oxidation and reduction peaks) also matches that predicted by the Nernst equation (Figure 68e).

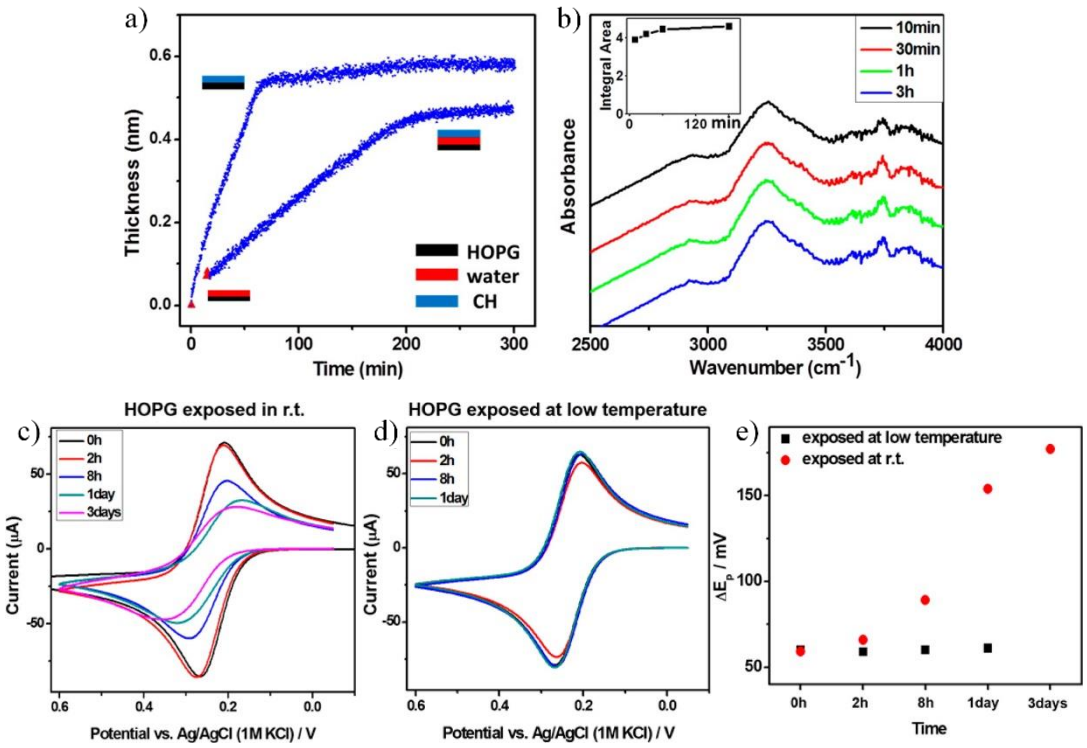

Figure 68. Measurements of hydrocarbon contamination. (a) Spectroscopic ellipsometry monitoring of hydrocarbon thickness on an exfoliated HOPG surface exposed in ambient air with (right) and without (left) low-temperature treatment to trigger water condensation. (b) ATR-FTIR spectrum of a freshly exfoliated HOPG sample after low-temperature treatment. Note the absence of CH_2 peaks. Cyclic voltammograms (1 mM $Fe(CN)_6^{4-}$ in 1.0 M KCl at 0.1 V s^{-1}) measured on freshly exfoliated HOPG exposed in air (c) at room temperature and (d) at low temperature. (e)

ΔEp (separation between the oxidation and reduction peaks) of HOPG stored in air under the two conditions. Reprinted with permission from Li et al., ACS Nano 2016, 10 (1), 349-359. Copyright 2016 American Chemical Society.

A common misconception is that a glovebox can protect the graphitic surface from contamination. Gloveboxes are designed to maintain low levels of oxygen and/or water but not hydrocarbons. In fact, the hydrocarbon concentrations are likely much higher inside a glovebox due to the use of rubber gloves and storage of organic solvents. In addition, since water adsorption is competitive with hydrocarbons, a water free atmosphere may contaminate graphitic surface more quickly than ambient conditions. Similarly, standardized classification of cleanroom is often strictly particulate-defined environments (*e.g.*, ISO 14644-1). Further restrictions on the environmental factors including airborne molecular contaminants had been recognized and became the standard practice. However, airborne molecular contamination control is less rigorous in many cleanroom facilities compare to airborne particulates due to its complexity, thus should be confirmed prior to surface-sensitive measurements.

When measurements can be done in high or ultra-high vacuum, one can drastically reduce the incident contaminant flux to circumvent the surface contamination.[202-205] Although there will still be adsorption in high vacuum (*e.g.*, by back diffused pump oil vapor), an UHV environment provides a much wider time window for researchers to study intrinsic surfaces. Heat treatment can be used to clean the surface of materials once the target material is loaded into UHV chamber if the material has high thermal stability. For example, various heating conditions (900 °C – 1500 ° C) had been reported to obtain a clean surface of graphite comparable to an UHV-cleaved graphite surface.[206-209] On the other hand, a clean surface can be obtained by directly using the mechanical

cleavage method inside the UHV chamber, as UHV-cleaved surfaces are free from ambient airborne contaminant exposure. The downside of UHV cleavage method is the required mechanical movement inside the UHV chamber,[210-212] but it is easily achievable with HOPG or other layered materials without specialized devices (Figure 69a). Typically, there is a sample preparation chamber separated from the UHV chamber, which is used to transfer samples into the UHV via a manipulator. The manipulator arm can be used to exfoliate HOPG after the prep chamber is already pumped down by affixing the tape to the inside of the prep chamber and simply pushing the manipulator forward. Figure 69b and 69c shows the clear difference in UPS spectrum of HOPG aged in UHV versus air.[200] UHV-cleaved graphite showed negligible change in its UPS spectra after 18 hours of aging in an UHV chamber compared to a distinct increase in the VOC signal in air aged HOPG. In addition, an immediate change in the surface composition was also observed in air-cleaved HOPG compared to UHV-cleaved HOPG.

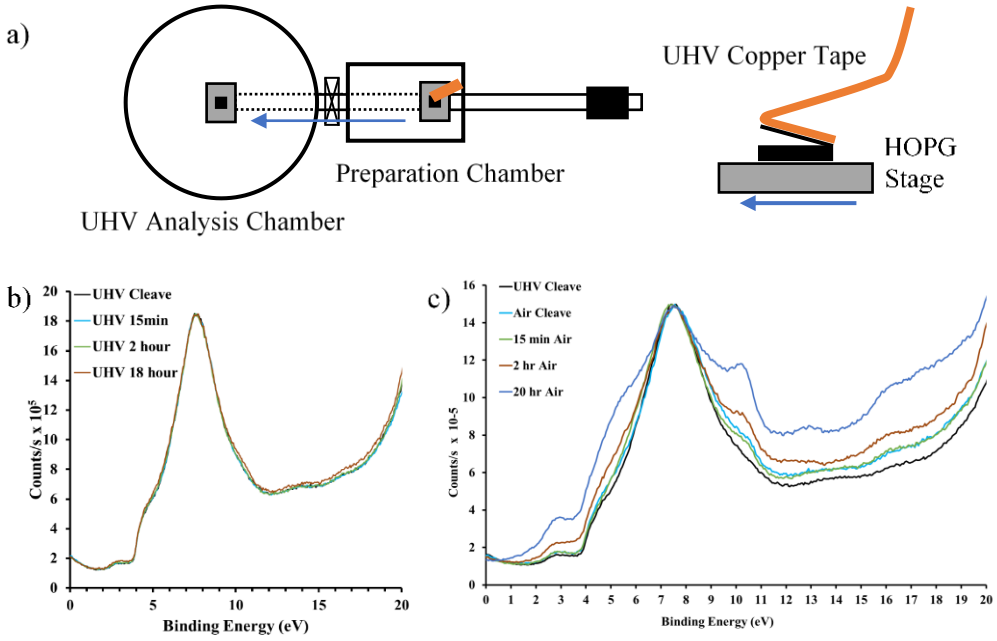

Figure 69. UHV methods. a) High vacuum cleavage of HOPG. HOPG is exfoliated via transferring motion of a horizontal manipulator from preparation chamber to the UHV analysis

chamber of the ESCALAB 250Xi spectrometer. UPS spectra (He II, 10 eV pass energy) of HOPG cleaved and aged in b) UHV and c) air. Spectra intensities are normalized to the highest peak. Arrows denote binding energy regions. Reprinted with permission from Salim et al., *Journal of Electron Spectroscopy and Related Phenomena* **2019**, *235*, 8-15. Copyright 2019 Elsevier.

For graphene, the contamination from ambient exposure can be even harder to avoid. Mechanically exfoliated graphene using HOPG has limited control in size and number of layers being exfoliated. Therefore, it often requires a time-consuming fabrication process once exfoliated onto the target substrates. Unless the sample fabrication process is done under UHV, one should assume the contamination is at equilibrium with the ambient. In the case of chemical vapor deposition (CVD) grown graphene, the low-pressure synthesis chamber can help to keep the surface clean before graphene is taken out to ambient conditions. Thus, one can minimize the effect of airborne contamination by performing measurements as soon as taking the graphene out of the CVD chamber. However, when a different substrate is desired (other than the catalyst metal substrate used in CVD growth), avoiding contamination can be challenging due to the transfer process.

Wet transfer methods often involve the deposition of a supportive layer on the graphene surface which is removed once graphene is placed onto the desired substrate. These supportive layers can be hard to remove completely, and residues of supporting materials can have a significant impact on the electronic, chemical, and mechanical properties of graphene. Therefore, surface sensitive measurements on graphene, are often done with transfer methods that expose the surface of graphene originally in contact with the metal substrates used in CVD synthesis. For example, a graphene electrode can be fabricated by attaching graphene/Cu on the target substrate

and placing in an etchant solution to etch Cu and expose the side of graphene surface that was originally in contact with Cu.[213] In this type of transfer, the contamination of the graphene surface occurs on the solid-liquid interface, therefore the contamination is often not as severe due to the reduced availability of contaminant and their slower diffusion in the liquid phase.

Another type of graphene transfer method that is useful to avoid airborne contamination is the hot-press method. Typically, graphene on a metal substrate is placed on a soft substrate, and heat and pressure are applied to form conformal contact between the graphene and the soft/flexible substrate. Once graphene is attached to the flexible substrate, the metal substrate is etched away. Again, the surface of graphene subjected to study in this case was initially in contact with the metal substrate and only exposed to the liquid phase, slowing down the adsorption of airborne contamination. It is worth noting that the adhesion strength between graphene and polymers can be increased to the point that the initial metal substrate (*e.g.*, Cu) can be simply peeled off, leaving graphene transferred onto the target substrate without using an etching process.[214-215]

Above we have reviewed many best practices for mitigating hydrocarbon contamination on carbon surfaces. Although it is possible to limit the amount of contamination, it may not always be obvious what change in the system would occur from contamination, were it there. For these systems it may be necessary to employ positive and negative control experiments to determine to what degree the surface is affected. A sample that is left in the same container as a long chain hydrocarbon for a few hours can serve as a positive control. After measuring this sample and comparing the results to a clean measurement, one should be able to determine the effect of hydrocarbon adsorption on their system. Although it may not always be necessary, one may consider studying the kinetics of adsorption so as to extrapolate what a truly clean surface would be.

Finally, it may also be useful to use this standard for interpretation of other published data. If the authors are careful to explain the controls they used, and were attentive to cleanness and time spent in air, then their data is likely trustworthy. If no such considerations were mentioned in the work, then one may need to view the data with a more critical eye.

Appendix C.7 Conclusions

We have reviewed the pervasiveness of hydrocarbon contamination on graphitic carbon, its characterization, and ways to mitigate its negative impact on material properties. For graphite, reducing the amount of time between exfoliation and measurement is of great importance. Under typical conditions, the surface converge of contaminants remains <1 % within the first 10 – 60 seconds after exfoliation. It is also possible to use an adsorbed water protection layer to slow down hydrocarbon contamination. For experiments under UHV, airborne contamination can be avoided by exfoliating graphite *in situ*. CVD graphene can be protected from hydrocarbons contaminants by choosing a transfer method that exposes the face of graphene originally in contact with the metal growth substrate.

By using the techniques outlined here, one can properly quantify the magnitude of the contamination and limit its negative impact on the planned experiments. We hope the readers will find this protocol paper helpful in their study of the intrinsic properties of carbon materials. Indeed, although carbon is an old material, there are many new discoveries to be made on a clean surface!

Appendix C.8 Acknowledgements

This work is supported in part by ONR (N00014-18-1-2555)

6.0 References

1. Duke, C., The birth and evolution of surface science: Child of the union of science and technology. *Proceedings of the National Academy of Sciences* **2003,** *100* (7), 3858-3864.

2. Ertl, G., Elementary processes at gas/metal interfaces. *Angewandte Chemie International Edition in English* **1976,** *15* (7), 391-400.

3. Young, R.; Ward, J.; Scire, F., Observation of metal-vacuum-metal tunneling, field emission, and the transition region. *Physical Review Letters* **1971,** *27* (14), 922.

4. Swift, P., Adventitious carbon—the panacea for energy referencing? *Surface and Interface Analysis* **1982,** *4* (2), 47-51.

5. Dukes, C. A.; Baragiola, R. A., Compact plasma source for removal of hydrocarbons for surface analysis. *Surface and Interface Analysis: An International Journal devoted to the development and application of techniques for the analysis of surfaces, interfaces and thin films* **2010,** *42* (1), 40-44.

6. Sherman, R.; Hirt, D.; Vane, R., Surface cleaning with the carbon dioxide snow jet. *Journal of Vacuum Science & Technology A: Vacuum, Surfaces, and Films* **1994,** *12* (4), 1876-1881.

7. Zubkov, T.; Stahl, D.; Thompson, T. L.; Panayotov, D.; Diwald, O.; Yates, J. T., Ultraviolet light-induced hydrophilicity effect on TiO2 (110)(1× 1). Dominant role of the photooxidation of adsorbed hydrocarbons causing wetting by water droplets. *The Journal of Physical Chemistry B* **2005,** *109* (32), 15454-15462.

8. Boinovich, L. B.; Emelyanenko, A. M.; Pashinin, A. S.; Lee, C. H.; Drelich, J.; Yap, Y. K., Origins of thermodynamically stable superhydrophobicity of boron nitride nanotubes coatings. *Langmuir* **2012,** *28* (2), 1206-1216.

9. Shinozaki, A.; Arima, K.; Morita, M.; KOJIMA, I.; AZUMA, Y., FTIR-ATR evaluation of organic contaminant cleaning methods for SiO2 surfaces. *Analytical Sciences* **2003,** *19* (11), 1557-1559.

10. Li, Z.; Wang, Y.; Kozbial, A.; Shenoy, G.; Zhou, F.; McGinley, R.; Ireland, P.; Morganstein, B.; Kunkel, A.; Surwade, S. P.; Li, L.; Liu, H., Effect of airborne contaminants on the wettability of supported graphene and graphite. *Nat Mater* **2013,** *12* (10), 925-931.

11. Goodenough, J. B.; Abruna, H.; Buchanan, M. In *Basic research needs for electrical energy storage*, Report of the basic energy sciences workshop for electrical energy storage, 2007.

12. Thackeray, M. M.; Wolverton, C.; Isaacs, E. D., Electrical energy storage for transportation-approaching the limits of, and going beyond, lithium-ion batteries. *Energy & Environmental Science* **2012,** *5* (7), 7854-7863.

13. Tarascon, J. M.; Armand, M., Issues and challenges facing rechargeable lithium batteries. *Nature* **2001,** *414* (6861), 359-367.

14. Simon, P.; Gogotsi, Y., Materials for electrochemical capacitors. In *Nanoscience and technology: a collection of reviews from Nature journals*, World Scientific: 2010; pp 320-329.

15. Lewandowski, A.; Galinski, M., Practical and theoretical limits for electrochemical double-layer capacitors. *Journal of Power Sources* **2007,** *173* (2), 822-828.

16. Miller, J. R.; Simon, P., Electrochemical Capacitors for Energy Management. *Science* **2008,** *321* (5889), 651-652.

17. Frackowiak, E.; Béguin, F., Carbon materials for the electrochemical storage of energy in capacitors. *Carbon* **2001,** *39* (6), 937-950.

18. Zhang, Y.; Feng, H.; Wu, X.; Wang, L.; Zhang, A.; Xia, T.; Dong, H.; Li, X.; Zhang, L., Progress of electrochemical capacitor electrode materials: A review. *International Journal of Hydrogen Energy* **2009,** *34* (11), 4889-4899.

19. Bard, A. J.; Faulkner, L. R., Fundamentals and applications. *Electrochemical Methods, 2nd ed.; Wiley: New York* **2001**.

20. Conway, B. E.; Bockris, J. O. M.; Ammar, I. A., The dielectric constant of the solution in the diffuse and Helmholtz double layers at a charged interface in aqueous solution. *Transactions of the Faraday Society* **1951,** *47* (0), 756-766.

21. Liu, C.; Yu, Z.; Neff, D.; Zhamu, A.; Jang, B. Z., Graphene-Based Supercapacitor with an Ultrahigh Energy Density. *Nano Letters* **2010,** *10* (12), 4863-4868.

22. Gamby, J.; Taberna, P. L.; Simon, P.; Fauvarque, J. F.; Chesneau, M., Studies and characterisations of various activated carbons used for carbon/carbon supercapacitors. *Journal of Power Sources* **2001,** *101* (1), 109-116.

23. Pandolfo, A. G.; Hollenkamp, A. F., Carbon properties and their role in supercapacitors. *Journal of Power Sources* **2006,** *157* (1), 11-27.

24. Novoselov, K. S.; Falko, V. I.; Colombo, L.; Gellert, P. R.; Schwab, M. G.; Kim, K., A roadmap for graphene. *Nature* **2012,** *490* (7419), 192-200.

25. McCreery, R. L.; McDermott, M. T., Comment on electrochemical kinetics at ordered graphite electrodes. *Analytical chemistry* **2012,** *84* (5), 2602-2605.

26. Novoselov, K.; Jiang, D.; Schedin, F.; Booth, T.; Khotkevich, V.; Morozov, S.; Geim, A., Two-dimensional atomic crystals. *Proceedings of the National Academy of Sciences of the United States of America* **2005,** *102* (30), 10451-10453.

27. Kozbial, A.; Li, Z.; Sun, J.; Gong, X.; Zhou, F.; Wang, Y.; Xu, H.; Liu, H.; Li, L., Understanding the intrinsic water wettability of graphite. *Carbon* **2014,** *74*, 218-225.

28. Martinez-Martin, D.; Longuinhos, R.; Izquierdo, J. G.; Marele, A.; Alexandre, S. S.; Jaafar, M.; Gómez-Rodríguez, J. M.; Bañares, L.; Soler, J. M.; Gomez-Herrero, J., Atmospheric contaminants on graphitic surfaces. *Carbon* **2013,** *61*, 33-39.

29. Preston, D. J.; Miljkovic, N.; Sack, J.; Enright, R.; Queeney, J.; Wang, E. N., Effect of hydrocarbon adsorption on the wettability of rare earth oxide ceramics. *Applied Physics Letters* **2014,** *105* (1), 1-5.

30. Sullivan, N.; Mai, T.; Bowdoin, S.; Vane, R., A STUDY OF THE EFFECTIVENESS OF THE REMOVAL OF HYDROCARBON CONTAMINATION BY OXIDATIVE CLEANING INSIDE THE SEM. *Microscopy and Microanalysis* **2002,** *8* (SupplementS02), 720-721.

31. Taylor, C. E.; Garvey, S. D.; Pemberton, J. E., Carbon Contamination at Silver Surfaces: Surface Preparation Procedures Evaluated by Raman Spectroscopy and X-ray Photoelectron Spectroscopy. *Analytical Chemistry* **1996,** *68* (14), 2401-2408.

32. Gerischer, H., An interpretation of the double layer capacity of graphite electrodes in relation to the density of states at the Fermi level. *The Journal of Physical Chemistry* **1985,** *89* (20), 4249-4251.

33. Hallett, P. D., A brief overview of the causes, impacts and amelioration of soil water repellency–a review. *Soil and Water Research* **2008,** *3* (1), 521-528.

34. Dekker, L. W.; Oostindie, K.; Ritsema, C. J., Exponential increase of publications related to soil water repellency. *Soil Research* **2005,** *43* (3), 403-441.

35. Allen, M. R.; Ingram, W. J., Constraints on future changes in climate and the hydrologic cycle. *Nature* **2002,** *419* (6903), 224.

36. Tisdall, J. M.; Oades, J. M., Organic matter and water-stable aggregates in soils. *Journal of soil science* **1982,** *33* (2), 141-163.

37. Jarvis, N., A review of non-equilibrium water flow and solute transport in soil macropores: Principles, controlling factors and consequences for water quality. *European Journal of Soil Science* **2007,** *58* (3), 523-546.

38. Dekker, L. W.; Ritsema, C. J.; Oostindie, K.; Boersma, O. H., Effect of drying temperature on the severity of soil water repellency. *Soil Science* **1998,** *163* (10), 780-796.

39. Macdonald, J. R., Impedance spectroscopy. *Annals of Biomedical Engineering* **1992,** *20* (3), 289-305.

40. Mansfeld, F.; Lin, S.; Chen, Y. C.; Shih, H., Minimization of High-Frequency Phase Shifts in Impedance Measurements. *Journal of The Electrochemical Society* **1988,** *135* (4), 906-907.

41. Mahdavian, M.; Attar, M. M., Another approach in analysis of paint coatings with EIS measurement: Phase angle at high frequencies. *Corrosion Science* **2006,** *48* (12), 4152-4157.

42. Macdonald, D. D., Reflections on the history of electrochemical impedance spectroscopy. *Electrochimica Acta* **2006,** *51* (8–9), 1376-1388.

43. Boukamp, B. A., A nonlinear least squares fit procedure for analysis of immittance data of electrochemical systems. *Solid state ionics* **1986,** *20* (1), 31-44.

44. Randles, J. E. B., Kinetics of rapid electrode reactions. *Discussions of the Faraday Society* **1947,** *1* (0), 11-19.

45. Brug, G.; Van Den Eeden, A.; Sluyters-Rehbach, M.; Sluyters, J., The analysis of electrode impedances complicated by the presence of a constant phase element. *Journal of electroanalytical chemistry and interfacial electrochemistry* **1984,** *176* (1), 275-295.

46. Jorcin, J.-B.; Orazem, M. E.; Pébère, N.; Tribollet, B., CPE analysis by local electrochemical impedance spectroscopy. *Electrochimica Acta* **2006,** *51* (8–9), 1473-1479.

47. Zoltowski, P., On the electrical capacitance of interfaces exhibiting constant phase element behaviour. *Journal of Electroanalytical Chemistry* **1998,** *443* (1), 149-154.

48. Hsu, C. H.; Mansfeld, F., Technical Note: Concerning the Conversion of the Constant Phase Element Parameter Y0 into a Capacitance. *Corrosion* **2001,** *57* (9), 747-748.

49. Roche, A.; Wyon, C.; Marthon, S.; Ple, J.; Olivier, M.; Rochat, N.; Chabli, A.; Danel, A.; Juhel, M.; Tardif, F. In *Detection of organic contamination on silicon substrates: Comparison of several techniques*, Characterization and Metrology for ULSI Technology 2000, AIP Publishing: 2001; pp 297-301.

50. Tompkins, H.; Irene, E. A., *Handbook of ellipsometry*. William Andrew: 2005.

51. Jenkins, F. A.; White, H. E., *Fundamentals of optics*. Tata McGraw-Hill Education: 1957.

52. Jellison, G., The calculation of thin film parameters from spectroscopic ellipsometry data. *Thin Solid Films* **1996,** *290*, 40-45.

53. Chiu, M.-H.; Lee, J.-Y.; Su, D.-C., Complex refractive-index measurement based on Fresnel's equations and the uses of heterodyne interferometry. *Applied optics* **1999,** *38* (19), 4047-4052.

54. Jellison, G. E., Data analysis for spectroscopic ellipsometry. *Thin Solid Films* **1993,** *234* (1-2), 416-422.

55. Jellison, J. G. E., Spectroscopic ellipsometry data analysis: measured versus calculated quantities. *Thin Solid Films* **1998,** *313–314*, 33-39.

56. Hilfiker, J. N.; Synowicki, R. A.; Bungay, C. L.; Carpio, R., Spectroscopic ellipsometry for polymer thin films. *Solid state technology* **1998,** *41* (10), 101-107.

57. Weber, J. W.; Hansen, T. A. R.; van de Sanden, M. C. M.; Engeln, R., B-spline parametrization of the dielectric function applied to spectroscopic ellipsometry on amorphous carbon. *Journal of Applied Physics* **2009,** *106* (12), 123503-1-123503-9.

58. Michelson, A., The relation motion of the Earth and the Luminiferous Aether. *Amer. J. of Sci.(3). XXXII* **1881**, 220.

59. Nugent, K. A., Interferogram analysis using an accurate fully automatic algorithm. *Applied Optics* **1985,** *24* (18), 3101-3105.

60. Stuart, B. *Infrared spectroscopy: fundamentals and applications. JohnWiley & Sons, Ltd. ISBNs: 0-470-85427-8 (HB)*; 0-470-85428-6 (PB): 2004.

61. Doerr, S. H., On standardizing the 'water drop penetration time'and the 'molarity of an ethanol droplet'techniques to classify soil hydrophobicity: a case study using medium textured soils. *Earth Surface Processes and Landforms: The Journal of the British Geomorphological Group* **1998,** *23* (7), 663-668.

62. Hsu, C.; Mansfeld, F., Technical note: concerning the conversion of the constant phase element parameter Y0 into a capacitance. *Corrosion* **2001,** *57* (9), 747-748.

63. Scott, A. S.; Max, P. B.; Christopher, K. M., The Infrared Spectra of Polycyclic Aromatic Hydrocarbons with Excess Peripheral H atoms (H n -PAHs) and Their Relation to the 3.4 and 6.9 μm PAH Emission Features. *The Astrophysical Journal Supplement Series* **2013,** *205* (1), 8.

64. Silverstein, R. M.; Webster, F. X.; Kiemle, D. J.; Bryce, D. L., *Spectrometric identification of organic compounds*. John Wiley & Sons: 2014.

65. Randin, J. P.; Yeager, E., Differential Capacitance Study of Stress-Annealed Pyrolytic Graphite Electrodes. *Journal of The Electrochemical Society* **1971,** *118* (5), 711-714.

66. Randin, J.-P.; Yeager, E., Differential capacitance study on the basal plane of stress-annealed pyrolytic graphite. *Journal of Electroanalytical Chemistry and Interfacial Electrochemistry* **1972,** *36* (2), 257-276.

67. Delahay, P.; Trachtenberg, I., Adsorption kinetics and electrode processes. *Journal of the American Chemical Society* **1957,** *79* (10), 2355-2362.

68. Uematsu, M.; Frank, E. U., Static Dielectric Constant of Water and Steam. *Journal of Physical and Chemical Reference Data* **1980,** *9* (4), 1291-1306.

69. Hasted, J. B.; Ritson, D. M.; Collie, C. H., Dielectric Properties of Aqueous Ionic Solutions. Parts I and II. *The Journal of Chemical Physics* **1948,** *16* (1), 1-21.

70. Kozbial, A.; Gong, X.; Liu, H.; Li, L., Understanding the Intrinsic Water Wettability of Molybdenum Disulfide (MoS2). *Langmuir* **2015,** *31* (30), 8429-8435.

71. Zou, Y.; Walton, A. S.; Kinloch, I. A.; Dryfe, R. A. W., Investigation of the Differential Capacitance of Highly Ordered Pyrolytic Graphite as a Model Material of Graphene. *Langmuir* **2016,** *32* (44), 11448-11455.

72. CS Hsu, F. M., Concerning the Conversion of the Constant Phase Element Parameter Yo into a Capacitance. *Corrosion* **2001,** (57).

73. Robert M. Silverstein, F. X. W., David J. Keimle, In *Spectrophotometric Identification of Organic Compounds*, John Wiley & Sons: 2005; pp 72-126.

74. Hernandez, O., SIDS Initial Assessment Report for 12 th SIAM. UNEP Publications, Paris: 2001.

75. Fan, J.; Trenary, M., Symmetry and the Surface Infrared Selection Rule for the determination of the Structure of Molecules on Metal Surfaces. *Langmuir* **1994,** *10* (10), 3649-3657.

76. Francis, S. A.; Ellison, A. H., Infrared Spectra of Monolayers on Metal Mirrors. *J. Opt. Soc. Am.* **1959,** *49* (2), 131-138.

77. Mähler, J.; Persson, I., A study of the hydration of the alkali metal ions in aqueous solution. *Inorganic chemistry* **2011,** *51* (1), 425-438.

78. Bockris, J. M.; Devanathan, M.; Muller, K. In *On the structure of charged interfaces*, Proceedings of the Royal Society of London A: Mathematical, Physical and Engineering Sciences, The Royal Society: 1963; pp 55-79.

79. Kar, S.; Miramond, C.; Vuillaume, D., Properties of electronic traps at silicon/1-octadecene interfaces. *Applied Physics Letters* **2001,** *78* (9), 1288-1290.

80. Kornyshev, A. A., Double-Layer in Ionic Liquids: Paradigm Change? *The Journal of Physical Chemistry B* **2007,** *111* (20), 5545-5557.

81. Islam, M. M.; Alam, M. T.; Ohsaka, T., Electrical Double-Layer Structure in Ionic Liquids: A Corroboration of the Theoretical Model by Experimental Results. *The Journal of Physical Chemistry C* **2008,** *112* (42), 16568-16574.

82. Islam, M. M.; Alam, M. T.; Okajima, T.; Ohsaka, T., Electrical Double Layer Structure in Ionic Liquids: An Understanding of the Unusual Capacitance−Potential Curve at a Nonmetallic Electrode. *The Journal of Physical Chemistry C* **2009,** *113* (9), 3386-3389.

83. Kornyshev, A.; Luque, N.; Schmickler, W., Differential capacitance of ionic liquid interface with graphite: the story of two double layers. *Journal of Solid State Electrochemistry* **2014,** *18* (5), 1345-1349.

84. Müller, C.; Németh, K.; Vesztergom, S.; Pajkossy, T.; Jacob, T., The interface between HOPG and 1-butyl-3-methyl-imidazolium hexafluorophosphate. *Physical Chemistry Chemical Physics* **2016,** *18* (2), 916-925.

85. Hurst, J. M.; Li, L.; Liu, H., Adventitious hydrocarbons and the graphite-water interface. *Carbon* **2018,** *134*, 464-469.

86. Bonnaud, C.; Billard, I.; Papaiconomou, N.; Chainet, E.; Leprêtre, J., Rationale for the implementation of reference electrodes in ionic liquids. *Physical Chemistry Chemical Physics* **2016,** *18* (11), 8148-8157.

87. Baldelli, S., Surface structure at the ionic liquid− electrified metal interface. *Accounts of chemical research* **2008,** *41* (3), 421-431.

88. Lu, J.-Y.; Lai, C.-Y.; Almansoori, I.; Chiesa, M., The evolution in graphitic surface wettability with first-principles quantum simulations: the counterintuitive role of water. *Physical Chemistry Chemical Physics* **2018,** *20* (35), 22636-22644.

89. Doerr, S.; Shakesby, R.; Walsh, R., Soil water repellency: its causes, characteristics and hydro-geomorphological significance. *Earth-Science Reviews* **2000,** *51* (1-4), 33-65.

90. Foster, S.; Chilton, P., Groundwater: the processes and global significance of aquifer degradation. *Philosophical Transactions of the Royal Society of London B: Biological Sciences* **2003,** *358* (1440), 1957-1972.

91. Wallis, M.; Horne, D., Soil water repellency. In *Advances in soil science*, Springer: 1992; pp 91-146.

92. Schnitzer, M.; Khan, S. U., *Soil organic matter*. Elsevier: 1975.

93. Lehmann, J.; Kleber, M., The contentious nature of soil organic matter. *Nature (London)* **2015,** *528* (7580), 60-68.

94. Osman, K. T., *Soils: principles, properties and management*. 1. Aufl.;2013; ed.; Springer: New York;Dordrecht;, 2013; Vol. 9789400756632.

95. McIntosh, J.; Horne, D. In *Causes of repellency. I. The nature of the hydrophobic compounds found in a New Zealand development sequence of yellow-brown sands*, Proceedings of the 2nd National Water Repellency Workshop, Perth Western Australia: 1994; pp 1-5.

96. Franco, C.; Clarke, P.; Tate, M.; Oades, J., Hydrophobic properties and chemical characterisation of natural water repellent materials in Australian sands. *Journal of Hydrology* **2000,** *231*, 47-58.

97. Roper, M., Sorting our sandy soils. *Microbiol. Australia* **1998,** *19*, 6-7.

98. Moore, G.; Blackwell, P., Water repellence. *Soil guide: a handbook for understanding and managing agricultural soils. Agriculture Western Australia Bulletin* **1998,** *4343*, 53-63.

99. Fér, M.; Leue, M.; Kodešová, R.; Gerke, H. H.; Ellerbrock, R. H., Droplet infiltration dynamics and soil wettability related to soil organic matter of soil aggregate coatings and interiors. *Journal of Hydrology and Hydromechanics* **2016,** *64* (2), 111-120.

100. Hallett, P.; Gordon, D.; Bengough, A., Plant influence on rhizosphere hydraulic properties: direct measurements using a miniaturized infiltrometer. *New Phytologist* **2003,** *157* (3), 597-603.

101. Czarnes, S.; Hallett, P.; Bengough, A.; Young, I., Root-and microbial-derived mucilages affect soil structure and water transport. *European Journal of Soil Science* **2000,** *51* (3), 435-443.

102. Reeder, C. J.; Jurgensen, M., Fire-induced water repellency in forest soils of upper Michigan. *Canadian Journal of Forest Research* **1979,** *9* (3), 369-373.

103. Doerr, S.; Llewellyn, C.; Douglas, P.; Morley, C.; Mainwaring, K.; Haskins, C.; Johnsey, L.; Ritsema, C.; Stagnitti, F.; Allinson, G., Extraction of compounds associated with water repellency in sandy soils of different origin. *Soil Research* **2005,** *43* (3), 225-237.

104. Feeney, D. S.; Paul D. Hallett, T. D.; Karl Ritz, J. I.; Young, I. M., Does the presence of glomalin relate to reduced water infiltration through hydrophobicity? *Canadian Journal of Soil Science* **2004,** *84* (4), 365-372.

105. Mainwaring, K. A.; Morley, C. P.; Doerr, S. H.; Douglas, P.; Llewellyn, C. T.; Llewellyn, G.; Matthews, I.; Stein, B. K., Role of heavy polar organic compounds for water repellency of sandy soils. *Environmental Chemistry Letters* **2004,** *2* (1), 35-39.

106. Zisman, W. A., Relation of the Equilibrium Contact Angle to Liquid and Solid Constitution. In *Contact Angle, Wettability, and Adhesion*, AMERICAN CHEMICAL SOCIETY: 1964; Vol. 43, pp 1-51.

107. Kanta, A.; Sedev, R.; Ralston, J., Thermally- and Photoinduced Changes in the Water Wettability of Low-Surface-Area Silica and Titania. *Langmuir* **2005,** *21* (6), 2400-2407.

108. Liu, P.; Cao, L.; Zhao, W.; Xia, Y.; Huang, W.; Li, Z., Insights into the superhydrophobicity of metallic surfaces prepared by electrodeposition involving spontaneous adsorption of airborne hydrocarbons. *Applied Surface Science* **2015,** *324*, 576-583.

109. Woollam, J. A.; Johs, B. D.; Herzinger, C. M.; Hilfiker, J. N.; Synowicki, R. A.; Bungay, C. L. In *Overview of variable-angle spectroscopic ellipsometry (VASE): I. Basic theory and typical applications*, Optical Metrology: A Critical Review, International Society for Optics and Photonics: 1999; p 1029402.

110. Vig, J. R., UV/ozone cleaning of surfaces. *Journal of Vacuum Science & Technology A: Vacuum, Surfaces, and Films* **1985,** *3* (3), 1027-1034.

111. Vuye, G.; Fisson, S.; Van, V. N.; Wang, Y.; Rivory, J.; Abeles, F., Temperature dependence of the dielectric function of silicon using in situ spectroscopic ellipsometry. *Thin Solid Films* **1993,** *233* (1-2), 166-170.

112. Clarke, R.; Tapping, R.; Hopper, M.; Young, L., An ESCA Study of the Oxide at the Si-SiO2 Interface. *Journal of The Electrochemical Society* **1975,** *122* (10), 1347.

113. Strohmeier, B. R., An ESCA method for determining the oxide thickness on aluminum alloys. *Surface and Interface Analysis* **1990,** *15* (1), 51-56.

114. Siegbahn, K., Electron spectroscopy-an outlook. *Journal of Electron Spectroscopy and Related Phenomena* **1974,** *5* (1), 3-97.

115. Jensen, D. S.; Kanyal, S. S.; Madaan, N.; Vail, M. A.; Dadson, A. E.; Engelhard, M. H.; Linford, M. R., Silicon (100)/SiO2 by XPS. *Surface Science Spectra* **2013,** *20* (1), 36-42.

116. Li, Z.; Kozbial, A.; Nioradze, N.; Parobek, D.; Shenoy, G. J.; Salim, M.; Amemiya, S.; Li, L.; Liu, H., Water Protects Graphitic Surface from Airborne Hydrocarbon Contamination. *ACS Nano* **2016,** *10* (1), 349-359.

117. Ritsema, C. J.; Dekker, L. W., *Soil water repellency: Occurrence, consequences, and amelioration*. Elsevier: 2012.

118. Trasatti, S.; Petrii, O., Real surface area measurements in electrochemistry. *Pure and applied chemistry* **1991,** *63* (5), 711-734.

119. Johs, B.; Hale, J. S., Dielectric function representation by B-splines. *physica status solidi (a)* **2008,** *205* (4), 715-719.

120. Prunici, P.; Hess, P., Ellipsometric in situ measurement of oxidation kinetics and thickness of (C2–C20) alkylsilyl (sub)monolayers. *Journal of Applied Physics* **2008,** *103* (2), 024312.

121. Miramond, C.; Vuillaume, D., 1-octadecene monolayers on Si(111) hydrogen-terminated surfaces: Effect of substrate doping. *Journal of Applied Physics* **2004,** *96* (3), 1529-1536.

122. Homola, T.; Matoušek, J.; Medvecká, V.; Zahoranová, A.; Kormunda, M.; Kováčik, D.; Černák, M., Atmospheric pressure diffuse plasma in ambient air for ITO surface cleaning. *Applied Surface Science* **2012,** *258* (18), 7135-7139.

123. Sugiyama, K.; Ishii, H.; Ouchi, Y.; Seki, K., Dependence of indium–tin–oxide work function on surface cleaning method as studied by ultraviolet and x-ray photoemission spectroscopies. *Journal of Applied Physics* **2000,** *87* (1), 295-298.

124. Manica, D. P.; Mitsumori, Y.; Ewing, A. G., Characterization of Electrode Fouling and Surface Regeneration for a Platinum Electrode on an Electrophoresis Microchip. *Analytical Chemistry* **2003,** *75* (17), 4572-4577.

125. Sun, T.; Blanchard, P.-Y.; Mirkin, M. V., Cleaning Nanoelectrodes with Air Plasma. *Analytical Chemistry* **2015,** *87* (8), 4092-4095.

126. Ermakov, S. S.; Borzhitskaya, A. V.; Moskvin, L. N., Electrochemical Polishing of the Surface of a Gold Electrode and Its Effect on the Sensitivity of the Stripping Voltammetric Determination of Mercury(II). *Journal of Analytical Chemistry* **2001,** *56* (6), 542-545.

127. Duran, B.; Brocenschi, R. F.; France, M.; Galligan, J. J.; Swain, G. M., Electrochemical activation of diamond microelectrodes: implications for the in vitro measurement of serotonin in the bowel. *Analyst* **2014,** *139* (12), 3160-3166.

128. Yeh, C.-F.; Hsiao, C.-W.; Lin, S.-J.; Hsieh, C.-M.; Kusumi, T.; Aomi, H.; Kaneko, H.; Dai, B.-T.; Tsai, M.-S., The removal of airborne molecular contamination in cleanroom using

PTFE and chemical filters. *IEEE Transactions on semiconductor Manufacturing* **2004,** *17* (2), 214-220.

129. Den, W.; Bai, H.; Kang, Y., Organic airborne molecular contamination in semiconductor fabrication clean rooms a review. *Journal of The Electrochemical Society* **2006,** *153* (2), G149-G159.

130. Fujimoto, T.; Takeda, K.; Nonaka, T., Airborne molecular contamination: contamination on substrates and the environment in semiconductors and other industries. In *Developments in Surface Contamination and Cleaning*, Elsevier: 2008; pp 329-474.

131. Den, W.; Wang, C.-C., Enhancement of adsorptive chemical filters via titania photocatalysts to remove vapor-phase toluene and isopropanol. *Separation and Purification Technology* **2012,** *85*, 101-111.

132. Fenner, D.; Biegelsen, D.; Bringans, R., Silicon surface passivation by hydrogen termination: A comparative study of preparation methods. *Journal of Applied Physics* **1989,** *66* (1), 419-424.

133. Moon, D.; Kurokawa, A.; Ichimura, S.; Lee, H.; Jeon, I., Ultraviolet-ozone jet cleaning process of organic surface contamination layers. *Journal of Vacuum Science & Technology A: Vacuum, Surfaces, and Films* **1999,** *17* (1), 150-154.

134. Siperko, L., Scanning tunneling microscopy of various graphitic surfaces. *Journal of Vacuum Science & Technology B: Microelectronics and Nanometer Structures Processing, Measurement, and Phenomena* **1991,** *9* (2), 1061-1063.

135. Hu, F.; Karweik, D. H.; Kuwana, T., Activation and deactivation of glassy carbon electrodes. *Journal of electroanalytical chemistry and interfacial electrochemistry* **1985,** *188* (1-2), 59-72.

136. Zhou, J.; Wipf, D. O., UV/ozone pretreatment of glassy carbon electrodes. *Journal of Electroanalytical Chemistry* **2001,** *499* (1), 121-128.

137. Li, Z.; Wang, Y.; Kozbial, A.; Shenoy, G.; Zhou, F.; McGinley, R.; Ireland, P.; Morganstein, B.; Kunkel, A.; Surwade, S. P.; Li, L.; Liu, H., Effect of airborne contaminants on the wettability of supported graphene and graphite. *Nature Materials* **2013,** *12*, 925.

138. Amadei, C. A.; Lai, C.-Y.; Heskes, D.; Chiesa, M., Time dependent wettability of graphite upon ambient exposure: The role of water adsorption. *The Journal of Chemical Physics* **2014,** *141* (8), 084709.

139. Lai, C.-Y.; Tang, T.-C.; Amadei, C. A.; Marsden, A. J.; Verdaguer, A.; Wilson, N.; Chiesa, M., A nanoscopic approach to studying evolution in graphene wettability. *Carbon* **2014,** *80*, 784-792.

140. Mücksch, C.; Rösch, C.; Müller−Renno, C.; Ziegler, C.; Urbassek, H. M., Consequences of Hydrocarbon Contamination for Wettability and Protein Adsorption on Graphite Surfaces. *The Journal of Physical Chemistry C* **2015,** *119* (22), 12496-12501.

141. Nioradze, N.; Chen, R.; Kurapati, N.; Khvataeva-Domanov, A.; Mabic, S.; Amemiya, S., Organic Contamination of Highly Oriented Pyrolytic Graphite As Studied by Scanning Electrochemical Microscopy. *Analytical Chemistry* **2015,** *87* (9), 4836-4843.

142. Aria, A. I.; Kidambi, P. R.; Weatherup, R. S.; Xiao, L.; Williams, J. A.; Hofmann, S., Time Evolution of the Wettability of Supported Graphene under Ambient Air Exposure. *The Journal of Physical Chemistry C* **2016,** *120* (4), 2215-2224.

143. Wolkoff, P., Impact of air velocity, temperature, humidity, and air on long-term VOC emissions from building products. *Atmospheric environment* **1998,** *32* (14-15), 2659-2668.

144. Yu, C.; Crump, D., A review of the emission of VOCs from polymeric materials used in buildings. *Building and Environment* **1998,** *33* (6), 357-374.

145. Salthammer, T.; Mentese, S.; Marutzky, R., Formaldehyde in the indoor environment. *Chemical reviews* **2010,** *110* (4), 2536-2572.

146. Chuah, Y.; Tsai, C.-H.; Hu, S., Simultaneous control of particle contamination and VOC pollution under different operating conditions of a mini-environment that contains a coating process. *Building and environment* **2000,** *35* (2), 91-99.

147. Sherwood, P. M., Photoelectron spectroscopic studies of electrode and related surfaces. *Chemical Society Reviews* **1985,** *14* (1), 1-44.

148. Hubbard, A. T., Electrochemistry at well-characterized surfaces. *Chemical Reviews* **1988,** *88* (4), 633-656.

149. Liang, Y.; Paul, D. K.; Xie, Y.; Sherwood, P. M., Core and valence band photoelectron spectroscopic studies of nickel oxidation in an anaerobic liquid cell. *Analytical chemistry* **1993,** *65* (17), 2276-2281.

150. Kozbial, A.; Li, Z.; Conaway, C.; McGinley, R.; Dhingra, S.; Vahdat, V.; Zhou, F.; D'Urso, B.; Liu, H.; Li, L., Study on the Surface Energy of Graphene by Contact Angle Measurements. *Langmuir* **2014,** *30* (28), 8598-8606.

151. Rafiee, J.; Mi, X.; Gullapalli, H.; Thomas, A. V.; Yavari, F.; Shi, Y.; Ajayan, P. M.; Koratkar, N. A., Wetting transparency of graphene. *Nature Materials* **2012,** *11*, 217.

152. Shih, C.-J.; Wang, Q. H.; Lin, S.; Park, K.-C.; Jin, Z.; Strano, M. S.; Blankschtein, D., Breakdown in the Wetting Transparency of Graphene. *Physical Review Letters* **2012,** *109* (17), 176101.

153. Raj, R.; Maroo, S. C.; Wang, E. N., Wettability of Graphene. *Nano Lett.* **2013,** *13* (4), 1509-1515.

154. Shih, C.-J.; Strano, M. S.; Blankschtein, D., Wetting translucency of graphene. *Nature Materials* **2013,** *12*, 866.

155. Peng, S.; Lohse, D.; Zhang, X., Microwetting of Supported Graphene on Hydrophobic Surfaces Revealed by Polymerized Interfacial Femtodroplets. *Langmuir* **2014,** *30* (33), 10043-10049.

156. Ondarçuhu, T.; Thomas, V.; Nuñez, M.; Dujardin, E.; Rahman, A.; Black, C. T.; Checco, A., Wettability of partially suspended graphene. *Scientific Reports* **2016,** *6*, 24237.

157. Belyaeva, L. A.; van Deursen, P. M. G.; Barbetsea, K. I.; Schneider, G. F., Hydrophilicity of Graphene in Water through Transparency to Polar and Dispersive Interactions. **2018,** *30* (6), 1703274.

158. Prydatko, A. V.; Belyaeva, L. A.; Jiang, L.; Lima, L. M. C.; Schneider, G. F., Contact angle measurement of free-standing square-millimeter single-layer graphene. *Nature Communications* **2018,** *9* (1), 4185.

159. Kozbial, A.; Trouba, C.; Liu, H.; Li, L., Characterization of the Intrinsic Water Wettability of Graphite Using Contact Angle Measurements: Effect of Defects on Static and Dynamic Contact Angles. *Langmuir* **2017,** *33* (4), 959-967.

160. Tadros, M. E.; Hu, P.; Adamson, A. W., Adsorption and contact angle studies: I. Water on smooth carbon, linear polyethylene, and stearic acid-coated copper. *Journal of Colloid and Interface Science* **1974,** *49* (2), 184-195.

161. Ashraf, A.; Wu, Y.; Wang, M. C.; Aluru, N. R.; Dastgheib, S. A.; Nam, S., Spectroscopic Investigation of the Wettability of Multilayer Graphene Using Highly Ordered Pyrolytic Graphite as a Model Material. *Langmuir* **2014,** *30* (43), 12827-12836.

162. Marbou, K.; Al Ghaferi, A.; Jouiad, M., In-situ characterization of Wettability alteration in HOPG. *SOP Trans. Nanotechnol* **2015**, 1-10.

163. Wei, Y.; Jia, C. Q., Intrinsic wettability of graphitic carbon. *Carbon* **2015,** *87*, 10-17.

164. Fowkes, F. M.; Harkins, W. D., The State of Monolayers Adsorbed at the Interface Solid—Aqueous Solution. *J. Am. Chem. Soc.* **1940,** *62* (12), 3377-3386.

165. Morcos, I., Surface Tension of Stress-Annealed Pyrolytic Graphite. *The Journal of Chemical Physics* **1972,** *57* (4), 1801-1802.

166. Schrader, M. E., Ultrahigh vacuum techniques in the measurement of contact angles. IV. Water on graphite (0001). *The Journal of Physical Chemistry* **1975,** *79* (23), 2508-2515.

167. Westreich, P.; Fortier, H.; Flynn, S.; Foster, S.; Dahn, J. R., Exclusion of Salt Solutions from Activated Carbon Pores and the Relationship to Contact Angle on Graphite. *The Journal of Physical Chemistry C* **2007,** *111* (9), 3680-3684.

168. Wang, S.; Zhang, Y.; Abidi, N.; Cabrales, L., Wettability and surface free energy of graphene films. *Langmuir* **2009,** *25* (18), 11078-11081.

169. Ou, J.; Wang, J.; Liu, S.; Mu, B.; Ren, J.; Wang, H.; Yang, S., Tribology study of reduced graphene oxide sheets on silicon substrate synthesized via covalent assembly. *Langmuir* **2010,** *26* (20), 15830-15836.

170. Shin, Y. J.; Wang, Y.; Huang, H.; Kalon, G.; Wee, A. T. S.; Shen, Z.; Bhatia, C. S.; Yang, H., Surface-energy engineering of graphene. *Langmuir* **2010,** *26* (6), 3798-3802.

171. Taherian, F.; Marcon, V.; van der Vegt, N. F. A.; Leroy, F., What Is the Contact Angle of Water on Graphene? *Langmuir* **2013,** *29* (5), 1457-1465.

172. Chow, P. K.; Singh, E.; Viana, B. C.; Gao, J.; Luo, J.; Li, J.; Lin, Z.; Elías, A. L.; Shi, Y.; Wang, Z.; Terrones, M.; Koratkar, N., Wetting of Mono and Few-Layered WS2 and MoS2 Films Supported on Si/SiO2 Substrates. *ACS Nano* **2015,** *9* (3), 3023-3031.

173. Gao, J.; Li, B.; Tan, J.; Chow, P.; Lu, T.-M.; Koratkar, N., Aging of Transition Metal Dichalcogenide Monolayers. *ACS Nano* **2016,** *10* (2), 2628-2635.

174. Li, X.; Qiu, H.; Liu, X.; Yin, J.; Guo, W., Wettability of Supported Monolayer Hexagonal Boron Nitride in Air. *Advanced Functional Materials* **2017,** *27* (19), 1603181.

175. Khalkhali, M.; Zhang, H.; Liu, Q., Effects of Thickness and Adsorption of Airborne Hydrocarbons on Wetting Properties of MoS2: An Atomistic Simulation Study. *The Journal of Physical Chemistry C* **2018,** *122* (12), 6737-6747.

176. Zhou, Y.; Reed, E. J., Microscopic Origins of the Variability of Water Contact Angle with Adsorbed Contaminants on Layered Materials. *The Journal of Physical Chemistry C* **2018,** *122* (32), 18520-18527.

177. Velický, M.; Bissett, M. A.; Toth, P. S.; Patten, H. V.; Worrall, S. D.; Rodgers, A. N.; Hill, E. W.; Kinloch, I. A.; Novoselov, K. S.; Georgiou, T., Electron transfer kinetics on natural crystals of MoS 2 and graphite. *Physical Chemistry Chemical Physics* **2015,** *17* (27), 17844-17853.

178. Duignan, T. T.; Zhao, X. S., Impurities Limit the Capacitance of Carbon-Based Supercapacitors. *The Journal of Physical Chemistry C* **2019,** *123* (7), 4085-4093.

179. Iamprasertkun, P.; Hirunpinyopas, W.; Keerthi, A.; Wang, B.; Radha, B.; Bissett, M. A.; Dryfe, R. A. W., Capacitance of Basal Plane and Edge-Oriented Highly Ordered Pyrolytic Graphite: Specific Ion Effects. *The Journal of Physical Chemistry Letters* **2019,** *10* (3), 617-623.

180. Bowling, R. J.; Packard, R. T.; McCreery, R. L., Activation of highly ordered pyrolytic graphite for heterogeneous electron transfer: relationship between electrochemical performance and carbon microstructure. *Journal of the American Chemical Society* **1989,** *111* (4), 1217-1223.

181. Rice, R. J.; McCreery, R. L., Quantitative relationship between electron transfer rate and surface microstructure of laser-modified graphite electrodes. *Analytical Chemistry* **1989,** *61* (15), 1637-1641.

182. McDermott, M. T.; Kneten, K.; McCreery, R. L., Anthraquinonedisulfonate adsorption, electron-transfer kinetics, and capacitance on ordered graphite electrodes: the important role of surface defects. *The Journal of Physical Chemistry* **1992,** *96* (7), 3124-3130.

183. Cline, K. K.; McDermott, M. T.; McCreery, R. L., Anomalously Slow Electron Transfer at Ordered Graphite Electrodes: Influence of Electronic Factors and Reactive Sites. *The Journal of Physical Chemistry* **1994,** *98* (20), 5314-5319.

184. Davies, T. J.; Moore, R. R.; Banks, C. E.; Compton, R. G., The cyclic voltammetric response of electrochemically heterogeneous surfaces. *Journal of Electroanalytical Chemistry* **2004,** *574* (1), 123-152.

185. Lee, C.-Y.; Bond, A. M., Evaluation of Levels of Defect Sites Present in Highly Ordered Pyrolytic Graphite Electrodes Using Capacitive and Faradaic Current Components Derived Simultaneously from Large-Amplitude Fourier Transformed ac Voltammetric Experiments. *Analytical Chemistry* **2009,** *81* (2), 584-594.

186. Amemiya, S.; Bard, A. J.; Fan, F.-R. F.; Mirkin, M. V.; Unwin, P. R., Scanning Electrochemical Microscopy. *Annual Review of Analytical Chemistry* **2008,** *1* (1), 95-131.

187. Eifert, A.; Kranz, C., Hyphenating Atomic Force Microscopy. *Analytical Chemistry* **2014,** *86* (11), 5190-5200.

188. Frederix, P. L.; Bosshart, P. D.; Akiyama, T.; Chami, M.; Gullo, M. R.; Blackstock, J. J.; Dooleweerdt, K.; de Rooij, N. F.; Staufer, U.; Engel, A., Conductive supports for combined AFM–SECM on biological membranes. *Nanotechnology* **2008,** *19* (38), 384004.

189. Anne, A.; Cambril, E.; Chovin, A.; Demaille, C.; Goyer, C., Electrochemical Atomic Force Microscopy Using a Tip-Attached Redox Mediator for Topographic and Functional Imaging of Nanosystems. *ACS Nano* **2009,** *3* (10), 2927-2940.

190. Williams, C. G.; Edwards, M. A.; Colley, A. L.; Macpherson, J. V.; Unwin, P. R., Scanning Micropipet Contact Method for High-Resolution Imaging of Electrode Surface Redox Activity. *Analytical Chemistry* **2009,** *81* (7), 2486-2495.

191. Lai, S. C. S.; Patel, A. N.; McKelvey, K.; Unwin, P. R., Definitive Evidence for Fast Electron Transfer at Pristine Basal Plane Graphite from High-Resolution Electrochemical Imaging. *Angew. Chem. Int. Ed.* **2012,** *51* (22), 5405-5408.

192. Patel, A. N.; Collignon, M. G.; O'Connell, M. A.; Hung, W. O. Y.; McKelvey, K.; Macpherson, J. V.; Unwin, P. R., A New View of Electrochemistry at Highly Oriented Pyrolytic Graphite. *Journal of the American Chemical Society* **2012,** *134* (49), 20117-20130.

193. Güell, A. G.; Cuharuc, A. S.; Kim, Y.-R.; Zhang, G.; Tan, S.-y.; Ebejer, N.; Unwin, P. R., Redox-Dependent Spatially Resolved Electrochemistry at Graphene and Graphite Step Edges. *ACS Nano* **2015,** *9* (4), 3558-3571.

194. Chen, R.; Balla, R. J.; Li, Z.; Liu, H.; Amemiya, S., Origin of Asymmetry of Paired Nanogap Voltammograms Based on Scanning Electrochemical Microscopy: Contamination Not Adsorption. *Analytical Chemistry* **2016,** *88* (16), 8323-8331.

195. Tan, S.-y.; Zhang, J.; Bond, A. M.; Macpherson, J. V.; Unwin, P. R., Impact of Adsorption on Scanning Electrochemical Microscopy Voltammetry and Implications for Nanogap Measurements. *Analytical Chemistry* **2016,** *88* (6), 3272-3280.

196. Amemiya, S., Comment on "Impact of Adsorption on Scanning Electrochemical Microscopy Voltammetry and Implications for Nanogap Measurements": Assessment of Heterogeneous Self-Exchange Reaction at Conductor and Insulator. *Analytical Chemistry* **2017,** *89* (13), 7269-7272.

197. Kneten, K. R.; McCreery, R. L., Effects of redox system structure on electron-transfer kinetics at ordered graphite and glassy carbon electrodes. *Analytical Chemistry* **1992,** *64* (21), 2518-2524.

198. Salmeron, M.; Schlögl, R., Ambient pressure photoelectron spectroscopy: A new tool for surface science and nanotechnology. *Surface Science Reports* **2008,** *63* (4), 169-199.

199. Greenler, R. G.; Snider, D. R.; Witt, D.; Sorbello, R. S., The metal-surface selection rule for infrared spectra of molecules adsorbed on small metal particles. *Surface Science* **1982,** *118* (3), 415-428.

200. Salim, M.; Hurst, J.; Montgomery, M.; Tolman, N.; Liu, H., Airborne contamination of graphite as analyzed by ultra-violet photoelectron spectroscopy. *J. Electron. Spectrosc. Relat. Phenom.* **2019,** *235*, 8-15.

201. Bewig, K. W.; Zisman, W. A., The Wetting of Gold and Platinum by Water. *The Journal of Physical Chemistry* **1965,** *69* (12), 4238-4242.

202. Deitz, V. R.; Carpenter, F. G., The Rate of Physical Adsorption at Low Surface Coverage. In <*bold*>*SOLID SURFACES*</*bold*>, American Chemical Society: 1961; Vol. 33, pp 146-159.

203. Lerner, E.; Daunt, J. G., Adsorption of4He, Ar, and N2 on exfoliated graphite and of4He on Ar-coated exfoliated graphite at low temperatures. *Journal of Low Temperature Physics* **1973,** *10* (3), 299-307.

204. Bienfait, M.; Venables, J. A., Kinetics of adsorption and desorption using Auger electron spectroscopy: Application to xenon covered (0001) graphite. *Surface Science* **1977,** *64* (2), 425-436.

205. Diehl, R. D.; Jr., S. C. F., Adsorption of nitrogen molecules on graphite for 31<T<52 K: The fluid-to-commensurate-solid transition, multilayer condensation, and the pressure–temperature phase diagram. *The Journal of Chemical Physics* **1982,** *77* (10), 5065-5072.

206. Amelio, G. F.; Scheibner, E. J., Auger spectroscopy of graphite single crystals with low energy electrons. *Surface Science* **1968,** *11* (2), 242-254.

207. Price, G. L.; Venables, J. A., Layer growth of xenon on graphite. *Surface Science* **1975,** *49* (1), 264-274.

208. Metois, J.; Heyraud, J.; Takeda, Y., Experimental conditions to obtain clean graphite surfaces. *Thin Solid Films* **1978,** *51* (1), 105-117.

209. Métois, J. J.; Nitsche, S.; Heyraud, J. C., An ultra-high-vacuum transmission and scanning electron microscope for crystal growth experiments. *Ultramicroscopy* **1989,** *27* (4), 349-357.

210. Reichelt, K., Vacuum Cleavage Device for Mica. *Review of Scientific Instruments* **1973,** *44* (2), 243-244.

211. Lemke, B. P.; Haneman, D., Low-Temperature EPR Measurements on in situ Vacuum-Cleaved Silicon. *Physical Review Letters* **1975,** *35* (20), 1379-1382.

212. Angot, T.; Suzanne, J.; Hoarau, J. Y., An original in situ cleaver for low temperature surface experiments. *Review of Scientific Instruments* **1991,** *62* (7), 1865-1866.

213. Chen, R.; Nioradze, N.; Santhosh, P.; Li, Z.; Surwade, S. P.; Shenoy, G. J.; Parobek, D. G.; Kim, M. A.; Liu, H.; Amemiya, S., Ultrafast electron transfer kinetics of graphene grown by chemical vapor deposition. *Angew. Chem. Int. Ed.* **2015,** *54* (50), 15134-15137.

214. Fechine, G. J.; Martin-Fernandez, I.; Yiapanis, G.; Bentini, R.; Kulkarni, E. S.; de Oliveira, R. V. B.; Hu, X.; Yarovsky, I.; Neto, A. H. C.; Oezyilmaz, B., Direct dry transfer of chemical vapor deposition graphene to polymeric substrates. *Carbon* **2015,** *83*, 224-231.

215. Lock, E. H.; Baraket, M.; Laskoski, M.; Mulvaney, S. P.; Lee, W. K.; Sheehan, P. E.; Hines, D. R.; Robinson, J. T.; Tosado, J.; Fuhrer, M. S., High-quality uniform dry transfer of graphene to polymers. *Nano letters* **2011,** *12* (1), 102-107.